FLOW IN A POROUS MEDIUM DRIVEN BY DIFFERENTIAL HEATING

by

Mahosut Punpocha

Thesis submitted for the degree of

Doctor of Philosophy

Department of Mathematics

City University

London

September 2000

Contents

1

Acknowledgements

Declaration

I grant powers of discretion to the University Librarian to allow this thesis to be copied in whole or in part without further reference to me. This permission covers only single copies made for study purposes, subject to normal conditions of acknowledgement.

Abstract

This thesis is concerned with steady two-dimensional flow in a rectangular cavity filled with a saturated porous medium governed by Darcy's law. The flow is driven by differential heating of the upper surface of the cavity, whereas the sides and the bottom of the cavity are thermally insulated. Numerical calculations of the flow and temperature fields are carried out for cases where the temperature profile at the upper surface is a monotonic function of position (either a cosine function or a quadratic function) and results are obtained for a wide range of Darcy-Rayleigh numbers R and aspect ratios L which describe the resulting single-cell circulation. Analytical results are obtained in the limit of small Darcy-Rayleigh number using a perturbation method and are compared with the numerical results. At large Darcy-Rayleigh numbers the flow adopts a boundary-layer structure in which the main variations in temperature and velocity occur near the upper surface. In the case of the quadratic temperature profile at the upper surface, an exact solution of the horizontal boundary layer equations is found which provides useful insight, including a prediction of the almost constant temperature of the fluid in the core region below the horizontal boundary layer. This solution can only be regarded as approximate, however, because it fails to take account of the need for the solution to match with that in a vertical boundary layer at one end of the layer. By considering the properties of this vertical boundary layer it is argued that in the limit of large Darcy-Rayleigh number the entire leading order flow circulation is contained within the combined horizontal and vertical boundary layers near the upper surface. The solution of the combined horizontal and vertical boundary layer system is considered and an asymptotic solution is found at the lower edge of the layers which matches consistently across the layers and with a solution in the core region below. This is used to obtain an improved overall solution of the system in good agreement with the numerical calculations at large Darcy-Rayleigh numbers.

Chapter 1

Introduction

1.1 Background

Porous media play an important role in many areas of application including geothermal energy systems, oil and gas recovery, the spread of pollution in ground water and cavity wall insulation. A porous medium is a material consisting of a solid matrix with an interconnected void(pores). The porosity of the medium is defined as the fraction of the total volume of the medium that is occupied by void space; for natural media, the porosity does not normally exceed 0.6. The interconnected pores allow the flow of fluid through the material. In single phase flow the pores are saturated by a single fluid. In multiphase flow two or more fluids occupy the pore space. The distribution of pores with respect to shape and size is irregular in nature so on the pore scale(microscopic scale) the flow quantities will be irregular. However the quantities of interest are measured over an area that crosses many pores. Such space-averaged(macroscopic) quantities generally change in a regular manner with respect to space and time. This approach of averaging is called the spatial approach and a macroscopic variable is defined as an appropriate mean over a sufficiently large representative elementary volume. This operation yields the value of that variable at the centroid of the elementary volume. There is also a statistical approach in which the average is taken over an ensemble of possible pore structures. If we are concerned with deriving relationships between spatial quantities and not about their fluctuation in time, the results obtained by using the two approaches are the same. This leads to a continuum model for flow in a porous medium which is described in Section 1.2 below.

Previous studies of thermal convection in porous media can be divided into two main groups, those where the heating is from below and flow is generated typically by an instability mechanism, and those where the heating is from the side and horizontal thermal gradients generate motion (see equation (1.2.16) below). In the former case, the basic theory was developed by Lapwood (1948) who showed that instability due to buoyancy forces overcoming friction would result when the vertical thermal gradient was sufficiently large or, in non-dimensional terms, when the Darcy-Rayleigh number R (see(1.2.18) below) reaches a certain critical value. The basic theory for an infinite horizontal layer has since been extended in numerous ways to include, for example, the variation of viscosity and thermal expansion with temperature(Kassoy and Zebib 1975, Morland, Zebib and Kassoy 1977), nonlinear effects (Palm, Weber and Kvernvold 1972, Straus 1974), time-dependent motion(Schubert and Straus 1982) and the effect of lateral boundaries (Straus and Schubert 1979). Recent developments are discussed by Nield and Bejan (1999, chapter 6).

In the case of heating from the side, most previous studies have been concerned with the case of a two-dimensional cavity where the vertical walls of the cavity are maintained at different constant temperatures. If the upper and lower boundaries are either perfectly insulated or perfectly conducting, the solution of the problem possesses a centro-symmetry property as noted by Gill (1966) for the corresponding Newtonian problem. Weber (1975) considered the boundary layer structure on the vertical walls in the large Darcy-Rayleigh number limit ($R \rightarrow \infty$) for the case where the horizontal walls are insulated. The results of his analysis are in satisfactory agreement with experiment for the interior temperature distribution and the Nusselt number, defined as the ratio of the total heat transport to the heat transferred by pure conduction. He also included the effect of a variable viscosity by allowing the viscosity to be a linear function of temperature, which introduces asymmetry into the solution. Walker and Homsy (1978) considered the flow properties for large aspect ratio L(defined as the width of the cavity divided by the depth), and in the large and small R limits for fixed L. For large aspect ratio L and for large R, solutions were found by matched asymptotic expansions and for fixed L and small R solutions were found by a regular expansion in R using semi-numerical techniques. Blythe, Daniels and Simpkins (1982) considered the structure of the vertical boundary layers near the corners in the high Rayleigh number limit and subsequently they also considered the horizontal

7

boundary layer structure for the case of perfectly insulated boundaries (Daniels, Blythe and Simpkins 1982). This showed that in the high Rayleigh number limit the horizontal boundary layers have a double structure in which there is an outer layer of thickness $O(R^{-\frac{1}{4}})$ and an inner layer of thickness $O(R^{-\frac{5}{16}})$. This work provided a leading order description of the overall flow field in the entire cavity for the boundary layer regime ($R \to \infty$, L fixed). A summary of the various flow regimes is given by Blythe, Simpkins and Daniels (1983), and the properties of two distinct regimes where L is large were later examined in detail. In the intermediate regime (Daniels, Blythe and Simpkins 1986), where the Rayleigh number R is comparable with the cavity aspect ratio $L(\gg 1)$, they found that as the Rayleigh number increases the flow departs from a single cell Hadley structure and separate circulations develop at each end of the cavity. Later,(Daniels, Simpkins and Blythe 1989) they considered the merged layer regime which arises for large aspect ratio L when $R = O(L^2)$. They showed that in this limit, as L increases, the boundary layers on the horizontal walls merge to completely fill the cavity and there is non parallel core flow throughout the cavity.

Other work on the porous cavity problem with heated sidewalls includes numerical calculations by Chan, Ivey and Barry (1970), Hickox and Gartling (1981) and Prasad and Kulacki (1984) and a discussion of limiting structures in tall cavities ($L \ll 1$) by Ansari and Daniels (1993,1994). Also experimental results for this problem have been obtained by Klarsfeld (1970), Bankvall (1974), Combarnous and Bories (1975) and Seki, Fukusako and Inaba (1978). Other related work involving horzontal thermal gradients includes the horizontal boundary-layer analysis of Cheng and Chan (1976) and Chang and Cheng (1983) who considered similarity solutions of the porous medium boundary-layer equations on a heated horizontal wall. This and related work is described in a review article by Tien and Vafai (1990). More recently, the stability of porous media flows on horizontal surfaces has been considered by Rees and Bassom (1993, 1994). Porous medium boundary layer flows on heated vertical surfaces have been studied by Cheng and Minkowycz (1977), Merkin (1980), Ingham, Merkin and Pop (1982), Joshi and Gebhart (1984) and Ingham and Brown (1986), and flows driven by thermal gradients in corner regions by Daniels and Simpkins (1984), Ingham and Pop (1987) and Rees and Bassom (1991). For confined porous medium flows, there are also a number of studies which involve the generation of flow in a cavity

by internal heat sources, where typically a double-cell circulation may be produced(Haajizadeh, Ozguc and Tien 1984, Blythe, Daniels and Simpkins 1985, Prasad 1987, Mohamed 1995). Further examples and references pertaining to convection in porous media are discussed by Nield and Bejan (1999).

In the present thesis it is proposed to investigate thermally-driven flow in a two-dimensional cavity where the flow is driven by a temperature differential along the upper surface and the other walls are thermally insulated. Such flows may be relevant in groundwater systems where there is uneven heating of the Earth's surface and in flows driven by localised heat sources such as the magma chamber of a caldera (Chery, Bonneville, Vilotte and Yuen 1991). Unlike the case of fixed temperatures at the vertical walls, in the problem where the flow is driven by a temperature differential along the upper boundary the solution does not possess centro-symmetry. The purpose of the investigation is to gain insight into the structure of the steady state flow and temperature fields for different values of the Darcy-Rayleigh number R and the cavity aspect ratio L, and in particular to study in detail the limiting structure of the solution as $R \to \infty$.

1.2   Mathematical model

The system considered here is a rectangular two-dimensional cavity of length l and height d, filled with a saturated porous medium. The upper boundary is held at a temperature which depends on the distance from the corners while the bottom of the cavity and both vertical walls are thermally insulated.

Cartesian coordinates (x^*, z^*) are introduced with origin at the left hand lower corner of the cavity. Subject to Darcy's law, and the Oberbeck-Boussinesq approximation, steady single-phase flows in fluid-saturated porous media are governed by the equations

$$\nabla^* . \mathbf{u}^* = 0, \qquad (1.2.1)$$

$$\mathbf{u}^* = -\frac{K}{\mu}(\nabla^* p^* - \rho \mathbf{F}), \qquad (1.2.2)$$

$$\mathbf{u}^* . \nabla^* T^* = \kappa \nabla^{*2} T^*, \qquad (1.2.3)$$

where K is the permeability, μ is the coefficient of viscosity, ρ is the fluid density, κ is the thermal diffusivity, $\mathbf{u}^*$ is the velocity, p^* is the pressure, T^* is the temperature and $\mathbf{F}$ is any external force per unit mass. Equation (1.2.1) is the

continuity equation in which changes in the fluid density are neglected, in accordance with the Oberbeck- Boussinesq approximation(Oberbeck 1879, Boussinesq 1903). Equation (1.2.2) is Darcy's law under the approximation that the permeability and viscosity are constant and equation (1.2.3) is the thermal energy equation. Further details of the physical assumptions leading to these equations are given by Bear (1988), Nield and Bejan (1999) and de Boer (2000).

In two-dimensions with gravity acting in the negative z^* direction we have

$$\mathbf{u}^* = (u^*, w^*), \tag{1.2.4}$$

$$\mathbf{F} = (0, -g), \tag{1.2.5}$$

where g is the acceleration due to gravity. The equation of state is assumed to be

$$\rho = \rho_0(1 - \beta(T^* - T_0^*)), \tag{1.2.6}$$

where β is the coefficient of thermal expansion and T_0^* is the temperature at density ρ_0, and the governing equations (1.2.1)–(1.2.3) then become

$$\frac{\partial u^*}{\partial x^*} + \frac{\partial w^*}{\partial z^*} = 0, \tag{1.2.7}$$

$$u^* = -\frac{K}{\mu}\frac{\partial p^*}{\partial x^*}, \tag{1.2.8}$$

$$w^* = -\frac{K}{\mu}\frac{\partial p^*}{\partial z^*} - \frac{K\rho_0 g}{\mu}(1 - \beta(T^* - T_0^*)), \tag{1.2.9}$$

$$u^*\frac{\partial T^*}{\partial x^*} + w^*\frac{\partial T^*}{\partial z^*} = \kappa\nabla^{*2}T^*, \tag{1.2.10}$$

where $\nabla^{*2} = \frac{\partial^2}{\partial x^{*2}} + \frac{\partial^2}{\partial z^{*2}}$ is the two-dimensional Laplacian. Elimination of the pressure p^* yields

$$\nabla^{*2}\psi^* = -\frac{Kg\beta}{\nu}\frac{\partial T^*}{\partial x^*}, \tag{1.2.11}$$

$$\kappa\nabla^{*2}T^* = \frac{\partial(T^*, \psi^*)}{\partial(x^*, z^*)}, \tag{1.2.12}$$

where $\nu = \frac{\mu}{\rho_0}$ is the kinematic viscosity and ψ^* is the stream function defined by

$$u^* = \frac{\partial\psi^*}{\partial z^*}, \quad w^* = -\frac{\partial\psi^*}{\partial x^*}. \tag{1.2.13}$$

Non-dimensional variables x, z, ψ and T are introduced by defining

$$(x^*, z^*) = d(x, z), \tag{1.2.14}$$

$$\psi^* = \kappa\psi, \quad T^* = T_0^* + (\Delta T)T, \tag{1.2.15}$$

where ΔT is the maximum temperature difference along the upper boundary and T_0^* will be taken as the temperature at the left-hand corner $x = 0, z = 1$. Then equations (1.2.11), (1.2.12) become

$$\nabla^2\psi = -R\frac{\partial T}{\partial x}, \tag{1.2.16}$$

$$\nabla^2 T = \frac{\partial(T, \psi)}{\partial(x, z)}, \tag{1.2.17}$$

where

$$R = \frac{Kg\beta\Delta Td}{\kappa\nu}, \tag{1.2.18}$$

is the Darcy-Rayleigh number.

The boundary conditions for the stream function at the impermeable walls are

$$\psi = 0 \quad \text{on} \quad x = 0, L, \tag{1.2.19}$$

$$\psi = 0 \quad \text{on} \quad z = 0, 1, \tag{1.2.20}$$

where

$$L = \frac{l}{d} \tag{1.2.21}$$

is the aspect ratio of the cavity. The bottom and side walls are assumed to be thermally insulated, so that

$$\frac{\partial T}{\partial x} = 0 \quad \text{on} \quad x = 0, L, \tag{1.2.22}$$

$$\frac{\partial T}{\partial z} = 0 \quad \text{on} \quad z = 0, \tag{1.2.23}$$

while the imposed temperature at the upper boundary is taken to be

$$T = S(x), \quad (0 \le x \le L). \tag{1.2.24}$$

The mathematical problem is now defined by the equations(1.2.16), (1.2.17) and the boundary conditions (1.2.19), (1.2.20), (1.2.22), (1.2.23) and (1.2.24), and

11

contains two non-dimensional parameters, the Darcy-Rayleigh number R and the aspect ratio L.

1.3 Present study

The plan of the thesis is as follows. In Chapter 2, the flow is assumed to be driven by a temperature distribution along the upper wall given by a cosine function which is anti-symmetric about the vertical centre line of the cavity. The behaviour of the flow for small Darcy-Rayleigh numbers is investigated by means of a perturbation analysis. A numerical method of solution based on an explicit finite difference scheme is then used for calculating the flow and temperature fields at general Darcy-Rayleigh numbers, with particular emphasis on the case of a square cavity, $L = 1$. The results are compared with the perturbation analysis for small values of R and show how the flow develops with increasing values of the Darcy-Rayleigh number, and in particular the kind of boundary-layer structure that emerges as $R \to \infty$.

In Chapter 3, a quadratic temperature profile is applied at the upper boundary, and a detailed study is made of the effect of changing the aspect ratio of the cavity. Numerical results are obtained for aspect ratios in the range $0.25 \leq L \leq 4$ and for Darcy-Rayleigh numbers up to 5000.

Chapters 4 to 6 are concerned with the singular structure of the solution that develops as $R \to \infty$. The numerical results indicate that in this limit the main features of the flow and temperature fields occur in a horizontal boundary layer near the upper surface and a vertical boundary layer near the top of the sidewall on the colder side. In Chapter 4, an approximate analytical solution for the horizontal boundary layer is obtained by neglecting the interaction with the vertical boundary layer. By considering the heat flux through the upper surface of the cavity, a prediction is obtained for the temperature in the core region of the cavity, below the horizontal boundary layer.

In Chapter 5 we consider the properties of the vertical boundary layer and how it interacts with the horizontal layer. Asymptotic solutions are considered near the top of the vertical layer and near the bottom of the layer, where it merges with the core region. Further properties are investigated using an integral method. One of the main conclusions of this analysis is that the main flow circulation is actually completed within the horizontal and vertical layers near

the upper surface and that the core region therefore plays a relatively minor role in completing the mass-flux balance.

These ideas lead, in Chapter 6, to the development of a consistent overall solution structure in the cavity, in the large Darcy-Rayleigh number limit. An asymptotic solution is found at the lower edge of the horizontal boundary layer which matches consistently with a solution in the vertical boundary layer and is used to obtained an improved approximation to the combined horizontal/vertical boundary layer problem. A possible method for the complete numerical solution of this problem is outlined and some initial results are obtained. Properties of the solution in the core region are also discussed.

The results are summarized in Chapter 7 and possible future avenues of research are outlined.

Chapter 2

Flow in a Cavity Driven by Differential Heating of the Upper Surface

2.1 Introduction

We consider a two-dimensional cavity $0 \leq x \leq L, 0 \leq z \leq 1$ of aspect ratio L containing a fluid-saturated porous medium and thermally insulated along the two vertical sides ($x = 0, L$) and the horizontal base ($z = 0$). In this chapter we study the steady flow and temperature fields generated when the upper surface of the cavity is subject to an anti-symmetric temperature distribution

$$T = S(x) = \frac{1}{2}(1 - \cos\frac{\pi x}{L}), \quad (0 \leq x \leq L, z = 1). \tag{2.1.1}$$

Thus in non-dimensional terms the temperature at the upper boundary varies monotonically from zero at the left-hand (cold) corner to one at the right-hand (hot) corner, and is anti-symmetric about the value $T = \frac{1}{2}$ at the central point $x = \frac{L}{2}$. The configuration is shown in figure 2.1. As shown in Section 1.2, subject to Darcy's law and the Oberbeck-Boussinesq approximation, the non-dimensional stream function $\psi(x, z)$ and temperature $T(x, z)$ are governed by the equations

$$\nabla^2 \psi = -R\frac{\partial T}{\partial x}, \tag{2.1.2}$$

$$\nabla^2 T = \frac{\partial(T, \psi)}{\partial(x, z)}, \tag{2.1.3}$$

14

where R is the Darcy-Rayleigh number. The boundary conditions are given by (2.1.1) together with

$$\psi = \frac{\partial T}{\partial x} = 0 \quad \text{on} \quad x = 0, L \tag{2.1.4}$$

$$\psi = 0 \quad \text{on} \quad z = 0, 1, \tag{2.1.5}$$

$$\frac{\partial T}{\partial z} = 0 \quad \text{on} \quad z = 0. \tag{2.1.6}$$

In the next section the solution of the system (2.1.1)-(2.1.6) is found analytically for small values of the Darcy-Rayleigh number R using a perturbation method. A numerical scheme of solution for general values of R is described in Section 2.3 and results for the case of a square cavity ($L = 1$) are reported in Section 2.4. A brief summary is given in Section 2.5.

2.2 Solution for small Darcy-Rayleigh numbers

The solution for small Darcy-Rayleigh numbers can be obtained by assuming a perturbation expansion in powers of R:

$$T(x, z) = T_0(x, z) + RT_1(x, z) + \dots, \tag{2.2.1}$$

$$\psi(x, z) = R\psi_1(x, z) + R^2\psi_2(x, z) + \dots. \tag{2.2.2}$$

Substitution of (2.2.1) and (2.2.2) into (2.1.3) gives

$$\frac{\partial^2 T_0}{\partial x^2} + \frac{\partial^2 T_0}{\partial z^2} + R(\frac{\partial^2 T_1}{\partial x^2} + \frac{\partial^2 T_1}{\partial z^2}) + \dots =$$
$$(\frac{\partial T_0}{\partial x} + R\frac{\partial T_1}{\partial x} + \dots)(R\frac{\partial \psi_1}{\partial z} + R^2\frac{\partial \psi_2}{\partial z} + \dots)$$
$$- (\frac{\partial T_0}{\partial z} + R\frac{\partial T_1}{\partial z} + \dots)(R\frac{\partial \psi_1}{\partial x} + R^2\frac{\partial \psi_2}{\partial x} + \dots). \tag{2.2.3}$$

Equating coefficients of R^0 shows that the leading order temperature field $T_0(x, z)$ satisfies Laplace's equation

$$\frac{\partial^2 T_0}{\partial x^2} + \frac{\partial^2 T_0}{\partial z^2} = 0, \tag{2.2.4}$$

which must be solved subject to the boundary conditions

$$\frac{\partial T_0}{\partial x} = 0 \quad \text{on} \quad x = 0, L, \tag{2.2.5}$$

15

$$\frac{\partial T_0}{\partial z} = 0 \quad \text{on} \quad z = 0, \tag{2.2.6}$$

$$T_0 = S(x) = \frac{1}{2}(1 - \cos\frac{\pi x}{L}) \quad \text{on} \quad z = 1. \tag{2.2.7}$$

The solution is readily found to be

$$T_0 = \frac{1}{2} - \frac{1}{2}\operatorname{sech}\frac{\pi}{L}\cos\frac{\pi x}{L}\cosh\frac{\pi z}{L}. \tag{2.2.8}$$

Substitution of (2.2.1) and (2.2.2) into (2.1.2) gives

$$R(\frac{\partial^2 \psi_1}{\partial x^2} + \frac{\partial^2 \psi_1}{\partial z^2}) + R^2(\frac{\partial^2 \psi_2}{\partial x^2} + \frac{\partial^2 \psi_2}{\partial z^2}) = -R(\frac{\partial T_0}{\partial x} + R\frac{\partial T_1}{\partial x} + \ldots). \tag{2.2.9}$$

Equating coefficients of R shows that ψ_1 satisfies Poisson's equation

$$\frac{\partial^2 \psi_1}{\partial x^2} + \frac{\partial^2 \psi_1}{\partial z^2} = -\frac{\partial T_0}{\partial x}, \tag{2.2.10}$$

where T_0 is given by (2.2.8). This must be solved subject to the boundary conditions

$$\psi_1 = 0 \quad \text{on} \quad x = 0, L, \qquad \psi_1 = 0 \quad \text{on} \quad z = 0, 1. \tag{2.2.11}$$

The solution is found to be

$$\psi_1 = \frac{1}{4}(1 - z)\operatorname{sech}\frac{\pi}{L}\sinh\frac{\pi z}{L}\sin\frac{\pi x}{L}. \tag{2.2.12}$$

The leading order terms $T_0 - \frac{1}{2}$ and ψ_1 are seen to be odd and even functions of $x - \frac{1}{2}L$ respectively and their contours are shown in figure 2.2 for the case $L = 1$. The maximum value of the first order stream function, which defines the centre of circulation is found to be $\psi_1 = 0.0288277$ and occurs at $x = \frac{L}{2}, z = 0.689924$.

From equation (2.2.3) equating coefficients of R shows that the first-order temperature field T_1 satisfies Poisson's equation

$$\frac{\partial^2 T_1}{\partial x^2} + \frac{\partial^2 T_1}{\partial z^2} = \frac{\partial T_0}{\partial x}\frac{\partial \psi_1}{\partial z} - \frac{\partial T_0}{\partial z}\frac{\partial \psi_1}{\partial x}, \tag{2.2.13}$$

where, on the right-hand side, T_0 and ψ_1 are given by (2.2.8) and (2.2.12). This must be solved subject to the boundary conditions

$$\frac{\partial T_1}{\partial x} = 0 \quad \text{on} \quad x = 0, L, \tag{2.2.14}$$

16

$$\frac{\partial T_1}{\partial z} = 0 \quad \text{on} \quad z = 0, \tag{2.2.15}$$

$$T_1 = 0 \quad \text{on} \quad z = 1. \tag{2.2.16}$$

The solution can be determined in a straightforward manner and is found to be

$$T_1 = a_0 e^{\frac{2\pi z}{L}} + a_1 e^{\frac{-2\pi z}{L}} + a_2 z \cosh \frac{2\pi z}{L} + a_3 +$$
$$+ \cos \frac{2\pi x}{L}\left(a_4 e^{\frac{2\pi z}{L}} + a_5 e^{\frac{-2\pi z}{L}} - \frac{a_2}{2}\left(z \cosh \frac{2\pi z}{L} - 2(z-1)\right)\right), \tag{2.2.17}$$

where

$$a_0 = 2q\left(1 + \frac{L}{2\pi}\right), \tag{2.2.18}$$

$$a_1 = 2q\left(1 - \frac{L}{2\pi}\right), \tag{2.2.19}$$

$$a_2 = -4q, \tag{2.2.20}$$

$$a_3 = -\frac{2Lq}{\pi} \sinh \frac{2\pi}{L}, \tag{2.2.21}$$

$$a_4 = q\left(\frac{Le^{\frac{-2\pi}{L}}}{2\pi} \operatorname{sech} \frac{2\pi}{L} - 1\right), \tag{2.2.22}$$

$$a_5 = a_4 - \frac{Lq}{\pi}, \tag{2.2.23}$$

and

$$q = \frac{1}{256} \operatorname{sech}^2 \frac{\pi}{L}. \tag{2.2.24}$$

From equation (2.2.9), equating coefficients of R^2 shows that the second order stream function ψ_2 satisfies Poisson's equation

$$\frac{\partial^2 \psi_2}{\partial x^2} + \frac{\partial^2 \psi_2}{\partial z^2} = -\frac{\partial T_1}{\partial x}, \tag{2.2.25}$$

where T_1 is given by equation (2.2.17). This must be solved subject to the boundary conditions

$$\psi_2 = 0 \quad \text{on} \quad x = 0, L, \quad \psi_2 = 0 \quad \text{on} \quad z = 0, 1. \tag{2.2.26}$$

The solution is found to be

$$\psi_2 = \sin \frac{2\pi x}{L}\left(2b_1 z^2 \sinh \frac{2\pi z}{L} + z\left(b_2 e^{\frac{2\pi z}{L}} + b_3 e^{\frac{-2\pi z}{L}}\right) + \right.$$

17

$$+ b_4(z - 1 + e^{\frac{2\pi z}{L}} + b_5 \sinh \frac{2\pi z}{L})), \qquad (2.2.27)$$

where

$$b_1 = \frac{q}{4}, \qquad (2.2.28)$$

$$b_2 = \frac{a_4}{2} - \frac{Lq}{8\pi}, \qquad (2.2.29)$$

$$b_3 = \frac{-L}{4\pi}(\frac{q}{2} + \frac{2\pi a_5}{L}), \qquad (2.2.30)$$

$$b_4 = \frac{2Lq}{\pi}, \qquad (2.2.31)$$

$$b_5 = -b_0 - b_4^{-1}((b_1 + b_2)e^{\frac{2\pi}{L}} + (b_3 - b_1)e^{\frac{-2\pi}{L}})\operatorname{cosech}\frac{2\pi}{L} \qquad (2.2.32)$$

and

$$b_0 = 2(1 - e^{\frac{-4\pi}{L}})^{-1}. \qquad (2.2.33)$$

Contours of the functions T_1 and ψ_2, which are even and odd functions of $x - \frac{1}{2}L$ respectively, are shown in figure 2.3.

In summary, the solution at small Darcy-Rayleigh numbers is found to have the form

$$T = \left(\frac{1}{2} - \frac{1}{2}\operatorname{sech}\frac{\pi}{L}\cos\frac{\pi x}{L}\cosh\frac{\pi z}{L}\right) + R\left(a_0 e^{\frac{2\pi z}{L}} + a_1 e^{\frac{-2\pi z}{L}} + \right.$$
$$+ a_2 z \cosh\frac{2\pi z}{L} + a_3 +$$
$$\left. + \cos\frac{2\pi x}{L}(a_4 e^{\frac{2\pi z}{L}} + a_5 e^{\frac{-2\pi z}{L}} - \frac{a_2}{2}(z\cosh\frac{2\pi z}{L} - 2(z - 1)))\right)$$
$$+ O(R^2), \qquad (2.2.34)$$

$$\psi = R\left(\frac{1}{4}(1 - z)\operatorname{sech}\frac{\pi}{L}\sinh\frac{\pi z}{L}\sin\frac{\pi x}{L}\right) + R^2\left(\sin\frac{2\pi x}{L}(2b_1 z^2 \sinh\frac{2\pi z}{L} + \right.$$
$$\left. + z(b_2 e^{\frac{2\pi z}{L}} + b_3 e^{\frac{-2\pi z}{L}}) + b_4(z - 1 + e^{\frac{2\pi z}{L}} + b_5 \sinh\frac{2\pi z}{L}))\right)$$
$$+ O(R^3), \qquad (2.2.35)$$

where the various constants are given by (2.2.18)–(2.2.24) and (2.2.28)–(2.2.33). The temperature distribution along the upper boundary drives a circulation in the cavity with upwelling on the hot side and downwelling on the cold side. At leading order the velocity and temperature fields have symmetry about the centre line of the cavity ($x = \frac{L}{2}$) but the correction terms destroy this symmetry, as can be seen from contour plots of the overall temperature and stream function (2.2.34)

18

and (2.2.35) for $R = 5$, 10, 20 and 30 in figures 2.4-2.7. As the Darcy-Rayleigh number increases, the centre of circulation shifts towards the upper cold corner, while the isotherms swing around towards the hotter side.

2.3   Numerical method of solution

The steady-state equations (2.1.2) and (2.1.3) are of elliptic type but in order to obtain numerical solutions, time is introduced as an additional independent variable. Artificial time derivatives $\frac{\partial \psi}{\partial t}$ and $\frac{\partial T}{\partial t}$ are introduced and the system

$$
\frac{\partial \psi}{\partial t} \;=\; \nabla^2 \psi + R \frac{\partial T}{\partial x}, \tag{2.3.1}
$$

$$
\frac{\partial T}{\partial t} \;=\; \nabla^2 T - \frac{\partial(T, \psi)}{\partial(x, z)}, \tag{2.3.2}
$$

is considered, which is parabolic with respect to time. This allows a numerical solution to be obtained by a straightforward marching procedure in time, with the required steady-state results obtained in the limit of large time. An explicit finite difference method is used to solve the equations (2.3.1), (2.3.2) subject to the boundary conditions (2.1.4)–(2.1.6) and (2.1.1).

The rectangular domain $0 \le x \le L, \quad 0 \le z \le 1$ is covered with a uniform rectangular grid with spacings h in the x direction and k in the z direction. The discretized version of (2.3.1), (2.3.2) based on central differences in x and z and a forward difference in time is then

$$
\begin{aligned}
\psi_{i,j}^{n+1} = \psi_{i,j}^n &+ \frac{\Delta t}{h^2}(\psi_{i+1,j}^n - 2\psi_{i,j}^n + \psi_{i-1,j}^n) \\
&+ \frac{\Delta t}{k^2}(\psi_{i,j+1}^n - 2\psi_{i,j}^n + \psi_{i,j-1}^n) \\
&+ \frac{\Delta t R}{2h}(T_{i+1,j}^n - T_{i-1,j}^n),
\end{aligned} \tag{2.3.3}
$$

$$
\begin{aligned}
T_{i,j}^{n+1} = T_{i,j}^n &+ \frac{\Delta t}{h^2}(T_{i+1,j}^n - 2T_{i,j}^n + T_{i-1,j}^n) \\
&+ \frac{\Delta t}{k^2}(T_{i,j+1}^n - 2T_{i,j}^n + T_{i,j-1}^n), \\
&- (\frac{T_{i+1,j}^n - T_{i-1,j}^n}{2h})(\frac{\psi_{i,j+1}^n - \psi_{i,j-1}^n}{2k}) \\
&+ (\frac{T_{i,j+1}^n - T_{i,j-1}^n}{2k})(\frac{\psi_{i+1,j}^n - \psi_{i-1,j}^n}{2h}),
\end{aligned} \tag{2.3.4}
$$

where

$$\psi_{i,j}^n \;=\; \psi(x_i, z_j, t_n), \tag{2.3.5}$$

$$T_{i,j}^n \;=\; T(x_i, z_j, t_n), \tag{2.3.6}$$

$$\psi_{i,j}^{n+1} \;=\; \psi(x_i, z_j, t_n + \Delta t), \tag{2.3.7}$$

$$T_{i,j}^{n+1} \;=\; T(x_i, z_j, t_n + \Delta t), \tag{2.3.8}$$

and $x_i = ih, \quad z_j = jk, \quad t_n = n\Delta t$. Formulae (2.3.3) and (2.3.4) are used to advance the solution at all internal grid points. Because the explicit scheme (2.3.3) and (2.3.4) uses central differences in x and z, the discretization of the spatial derivatives is second order accurate. In discretizing the boundary conditions for $\frac{\partial T}{\partial x}$ and $\frac{\partial T}{\partial z}$ second order accuracy is maintained by using a quadratic approximation to T. For example, at the boundary $x = 0, \quad T$ is expressed in the form

$$T = a + bx + cx^2. \tag{2.3.9}$$

This is equated to the value of T at the new time step at the internal grid points $x = h$ and $x = 2h$. The boundary condition (2.1.6) requires $b = 0$ and so this determines the values of a and c. In particular, the value of T at the boundary $x = 0$ at the new time step is obtained as $T = a$. In this way the values of T at the new time step are obtained along the two sidewalls and the bottom wall. The boundary condition (2.1.1) determines T directly along the top boundary.

Computations were started at $t = 0$ from the initial state

$$T = 0, \quad \psi = 0, \tag{2.3.10}$$

and allowed to proceed until a steady state was achieved. The time step Δt was chosen to ensure that the condition for numerical stability and convergence of the equivalent pair of heat conduction equations (where the second terms on the right-hand sides of (2.3.1), (2.3.2) are neglected)

$$\Delta t \;\leq\; \frac{1}{2}\left(\frac{h^2 k^2}{h^2 + k^2}\right), \tag{2.3.11}$$

is satisfied. This proved to be effective in practice.

20

2.4 Numerical results

Various checks were carried out to test the accuracy and convergence of the numerical scheme. A comparison of the computed total heat flux at the upper boundary, the temperature at the centre of the cavity and the value of the stream function at the centre of the cavity for different step sizes h and k with $L = 1$ are shown in table 2.1 for a Darcy-Rayleigh number $R = 20$ and in table 2.2 for $R = 500$.

h, k	Total heat flux at upper boundary	Temperature at centre of cavity	Stream function at centre of cavity
0.05, 0.05	0.033754	0.428582	0.470505
0.02, 0.02	0.007494	0.428276	0.472080
0.01, 0.01	0.002750	0.428252	0.472274

Table 2.1: Comparison of the results for different grid sizes for $L = 1$ and $R = 20$

h, k	Total heat flux at upper boundary	Temperature at centre of cavity	Stream function at centre of cavity
0.05, 0.05	0.632147	0.165044	2.759958
0.02, 0.02	0.145898	0.161698	2.781390
0.01, 0.01	0.040989	0.161463	2.784363

Table 2.2: Comparison of the results for different grid sizes for $L = 1$ and $R = 500$

The time step Δt in each case is chosen to be

$$\Delta t = 0.2(\frac{h^2 k^2}{h^2 + k^2}).$$ (2.4.1)

The number of time steps,N, used in calculating each set of results was such that $N\Delta t = t = 2$, at which point the solution had reached its steady state form. The convergence of the solution to its steady-state form is illustrated in figures 2.8-2.13.

Figure 2.8 shows the heat flux at the upper boundary as t varies from zero to 2 for $L = 1$ and $R = 20$. For the steady state solution the total heat flux Q at the upper boundary must be zero: this can be shown analytically from equation (2.1.3) and the boundary conditions (2.1.4)-(2.1.6). It follows from integration of the heat equation over the cavity that

$$Q \equiv \int_0^L \frac{\partial T}{\partial z}\bigg|_{z=1} dx = \int_0^L (\psi \frac{\partial T}{\partial x})\bigg|_{z=0}^1 dx - \int_0^1 (\psi \frac{\partial T}{\partial z})\bigg|_{x=0}^L dz$$ (2.4.2)

but since $\psi = 0$ on the impermeable walls of the cavity it follows that

$$Q = \int_0^L \frac{\partial T}{\partial z}\bigg|_{z=1} dx = 0$$ (2.4.3)

so that the total heat flux across the upper boundary is zero. From the graph in figure 2.8 it is seen that the total heat flux decreases gradually to small values but never quite reaches zero due to the error in the numerical discretization and the use of the trapezoidal rule in calculating the integral (2.4.3). Figure 2.9 shows the corresponding behaviour for $R = 500$. Figures 2.10, 2.11 show the computed value of the temperature at the centre of the cavity for R=20, 500 as t varies from zero to 2. The temperature approaches a limiting value which varies slightly for different grid sizes at a given value of R. Figures 2.12 and 2.13 show the corresponding behaviour of the computed value of the stream function at the centre of the cavity for $R = 20$ and $R = 500$. As in the case of the temperature, the stream function approaches values which vary slightly for different grid sizes at a given value of R. The results for h, k = 0.02, 0.02 and h, k = 0.01, 0.01 are extremely close. The step sizes h and k were chosen to be 0.01 and 0.01 for all subsequent calculations.

22

The results of the numerical calculations for the stream function and temperature fields with $L = 1$ show that the flow moves in a counter clockwise direction. For small Darcy-Rayleigh numbers the centre of circulation is near the vertical centre-line of the cavity, as shown in figures 2.14-2.17. Analytical solutions for small R based on the results of Section 2.2 (figures 2.4-2.7) compare well with the numerical solutions and show that both results are in good agreement for values of R up to about 30.

As R increases, the numerical solutions show that the centre of circulation moves towards the cold end of the upper boundary, as can be seen in figures 2.18, 2.19.

For high values of the Darcy-Rayleigh number the temperature field starts to exhibit a boundary-layer structure at the upper boundary and near the vertical boundary at the upper cold corner. This can be seen clearly in figures 2.20, 2.21.

Figures 2.22-2.24 show the slip velocities on the sidewalls of the cavity for different values of the Darcy-Rayleigh number. The corresponding slip velocities on the upper and lower walls are shown in figures 2.25-2.27. The local heat flux at the upper boundary is shown for different Darcy-Rayleigh numbers in figures 2.28, 2.29 and the profiles calculated from the small Darcy-Rayleigh number analysis of Section 2.2 are shown for comparison in figure 2.30. A measure of the error in the numerical solution for different values of R is shown by the total heat flux at the upper boundary in figure 2.31.

The variation of the solution properties with R is shown in figures 2.32-2.37. The variation of the maximum stream function value ψ_{max} shown in a logarithmic plot in figure 2.32 confirms that ψ_{max} is of order R as $R \to 0$ and predicts a value of order $R^{1/3}$ as $R \to \infty$; this is confirmed by a boundary-layer analysis of the solution structure for large values of R in Chapter 4. The behaviour of the temperature at the centre of the cavity shown in figure 2.33 indicates that it approaches a finite, non-zero value of approximately 0.1, that is, about 10 per cent of the maximum temperature imposed at the upper surface. From the isotherms shown in figure 2.21 it is clear that at large R most of the cavity is at a temperature of about this value, the exception being the immediate vicinity of the upper surface. In contrast, the behaviour of the stream function at the centre of the cavity is less obvious, and although no clear asymptotic form has emerged at $R = 5000$ it appears that it may also be approaching a finite value independent of R. Figures 2.35-2.39 show the movement of the maximum stream

function location (x_{max}, z_{max}) as a function of R. The values of x_{max} and z_{max} plotted in these figures are only accurate to within the tolerance of the grid spacing (0.01). The centre of circulation moves into the upper cold corner of the cavity as $R \to \infty$.

2.5   Summary

In this chapter we have used numerical and asymptotic methods to investigate the flow and temperature fields in a fluid-saturated porous medium contained in a cavity whose upper surface is subject to differential heating. Analytical results have been obtained for small Darcy-Rayleigh numbers R and numerical results for general values of R, with particular emphasis on the case of a square cavity, $L = 1$. With increasing R, the differential heating drives a circulation whose centre moves towards the upper cold corner of the cavity. Most of the variation in temperature then occurs near the upper surface and below this the temperature tends to an almost constant value slightly greater than the coldest value at the upper surface. The structure of the cavity flow at large values of R is considered in detail in Chapters 4-6.

In the next chapter, results are obtained for an alternative temperature profile on the upper surface and a detailed investigation is made of how the aspect ratio influences the solution.
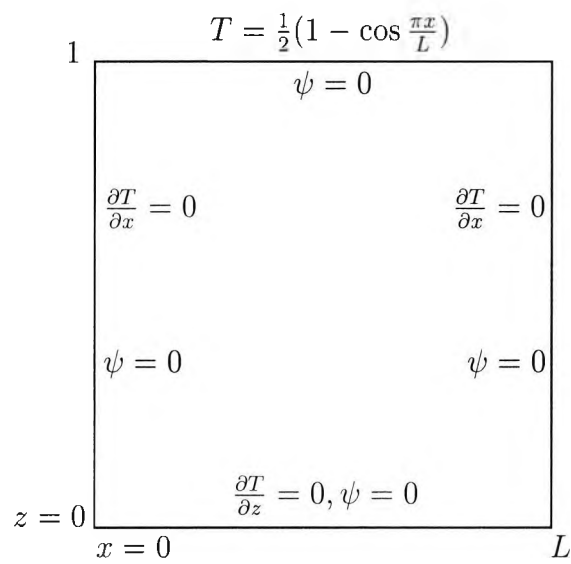
Figure 2.1: Configuration of the problem
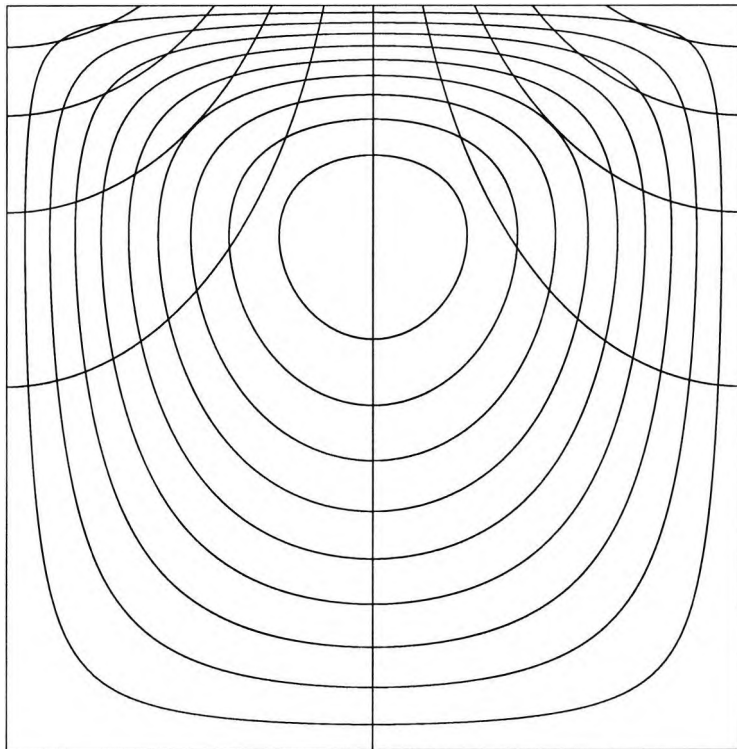
Figure 2.2: Contours of the leading order temperature and stream function for $L = 1$.
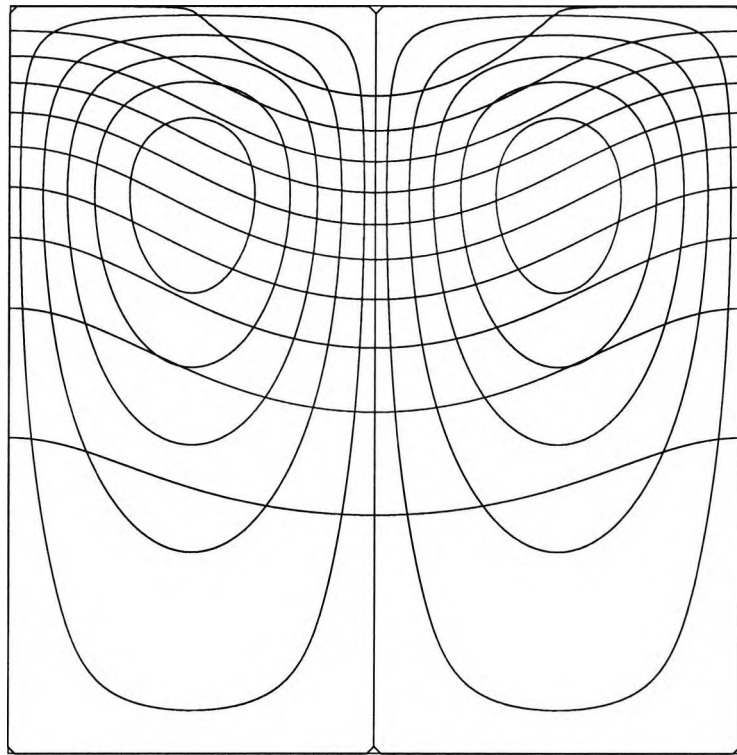
Figure 2.3: Contours of the first order temperature and stream function for $L = 1$.
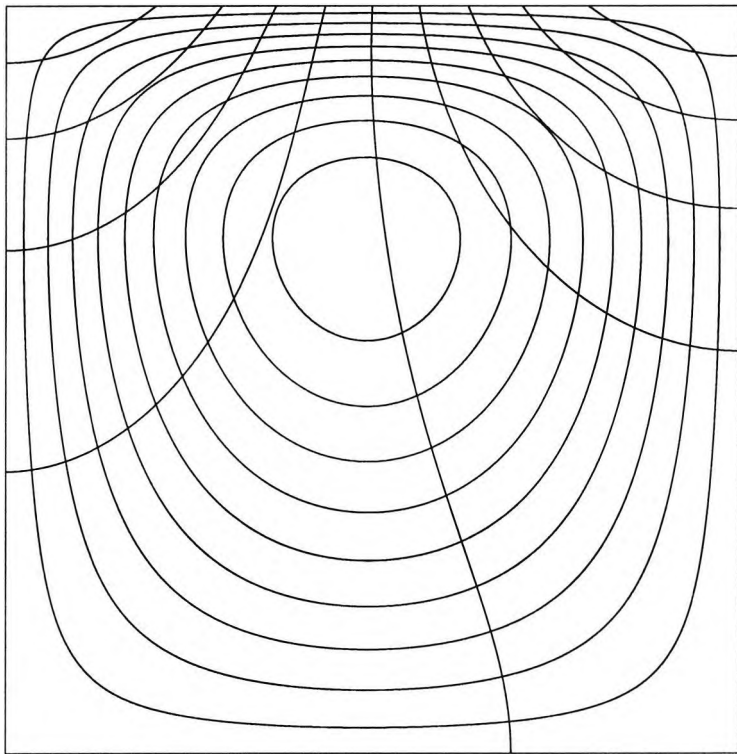
Figure 2.4: Analytical prediction of isotherms and streamlines for $L = 1$ and $R = 5$
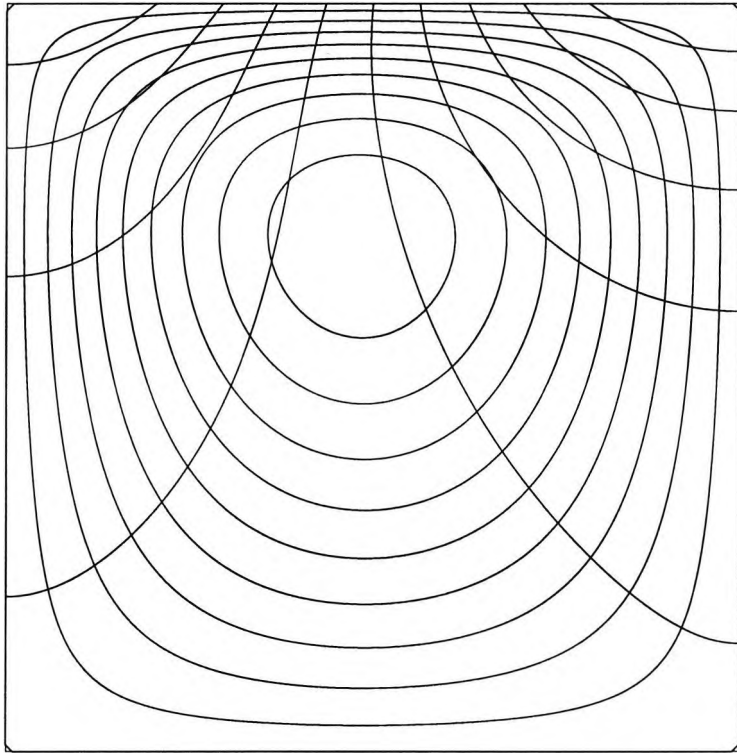
Figure 2.5: Analytical prediction of isotherms and streamlines for $L = 1$ and $R = 10$
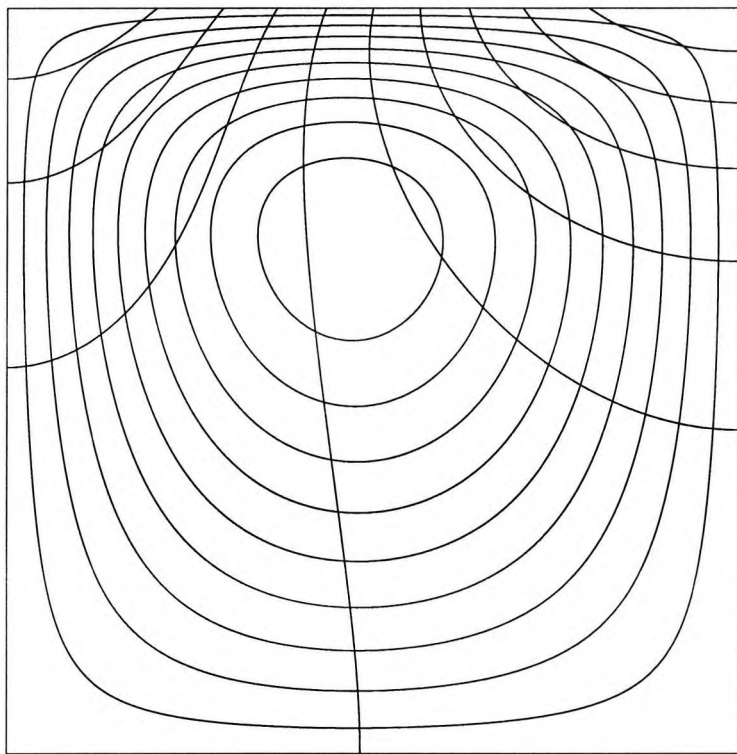
Figure 2.6: Analytical prediction of isotherms and streamlines for $L = 1$ and $R = 20$
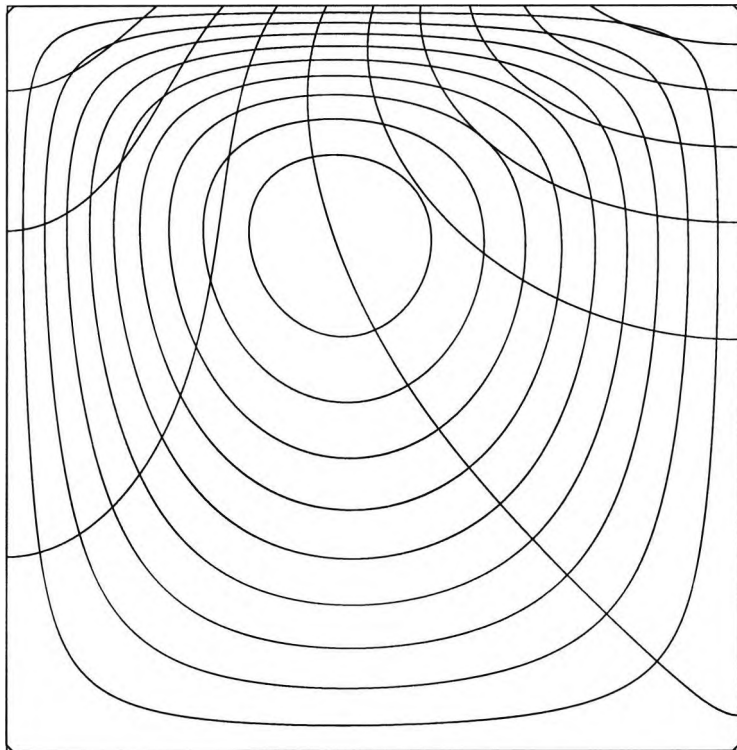
Figure 2.7: Analytical prediction of isotherms and streamlines for $L = 1$ and $R = 30$
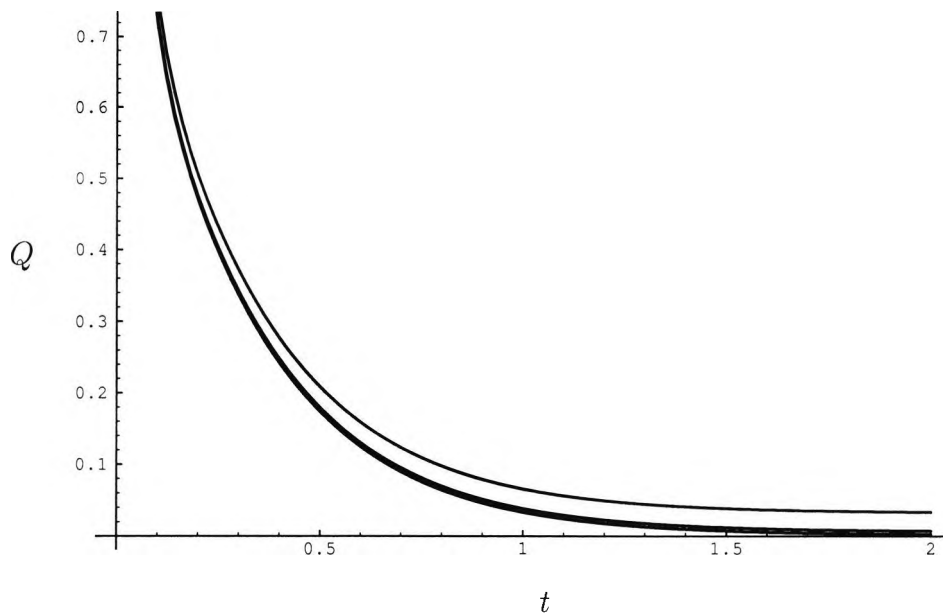
Figure 2.8: Total heat flux Q across the upper boundary for $L = 1$ and $R{=}20$ versus t for different grid sizes where the upper curve is for $h = 0.05, k = 0.05$, the middle curve for $h = 0.02, k = 0.02$ and the lower curve for $h = 0.01, k = 0.01$.
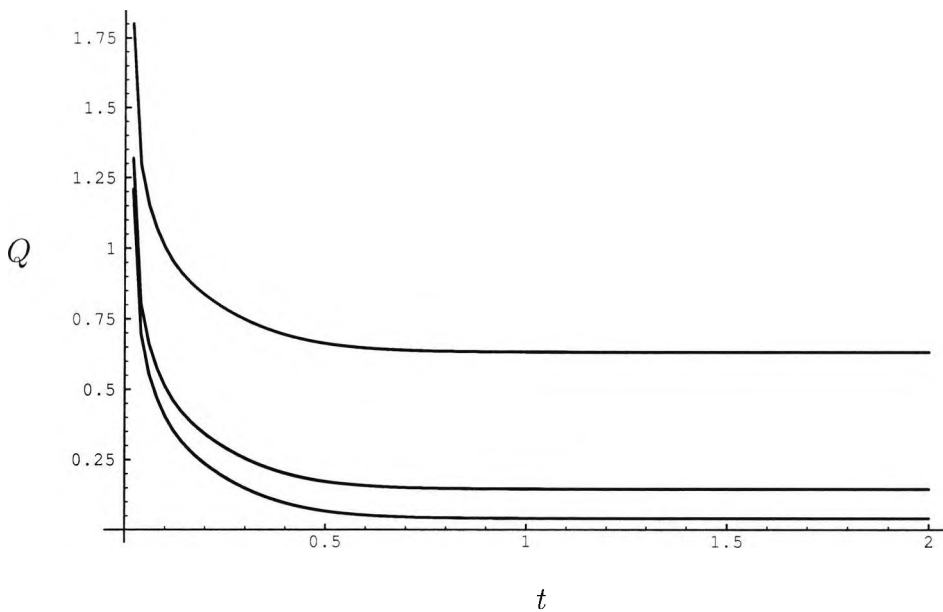
Figure 2.9: Total heat flux Q across the upper boundary for $L = 1$ and $R{=}500$ versus t for different grid sizes where the upper curve is for $h = 0.05, k = 0.05$, the middle curve for $h = 0.02, k = 0.02$ and the lower curve for $h = 0.01, k = 0.01$.
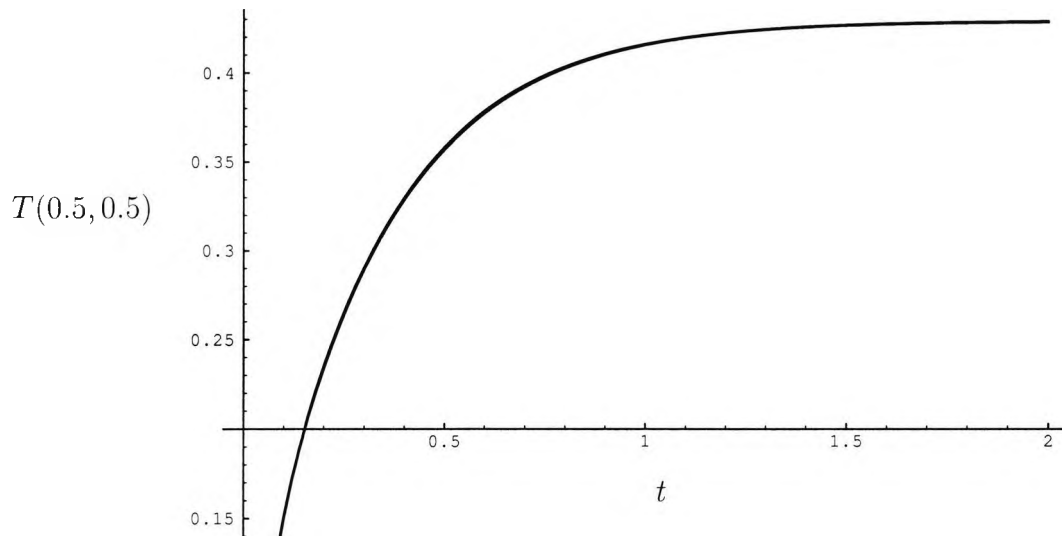
Figure 2.10: Value of the temperature at the centre of the cavity for $L = 1$ and $R = 20$ versus t for different grid sizes $h = 0.05, k = 0.05$; $h = 0.02, k = 0.02$ and $h = 0.01, k = 0.01$: all three curves are nearly the same
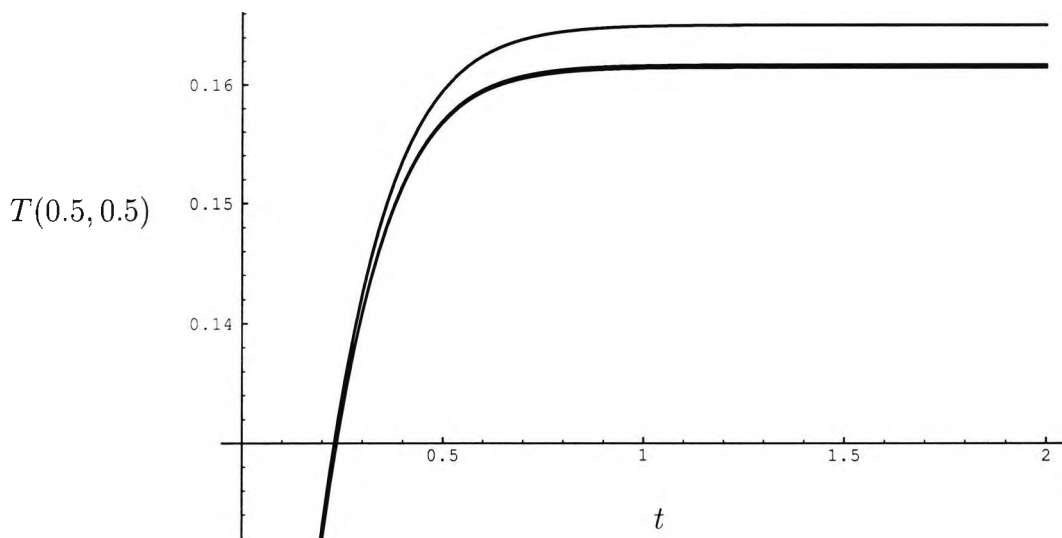
Figure 2.11: Value of the temperature at the centre of the cavity for $L = 1$ and $R = 500$ versus t for different grid sizes, where the upper curve is for $h = 0.05, k = 0.05$, the middle curve for $h = 0.02, k = 0.02$ and the lower curve for $h = 0.01, k = 0.01$.
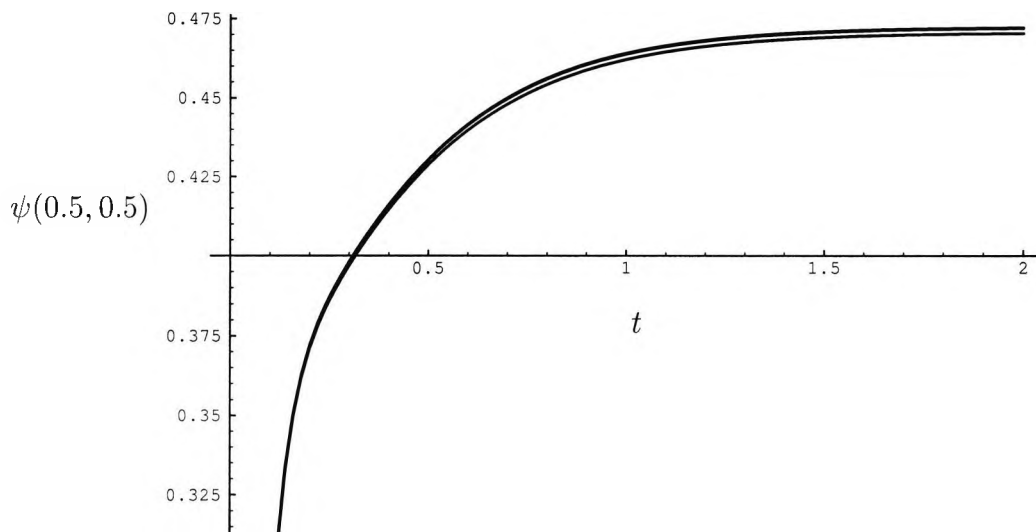
Figure 2.12: Value of the stream function at the centre of the cavity for $L = 1$ and $R = 20$ versus t for different grid sizes, where the upper curves are for $h = 0.01, k = 0.01$ and $h = 0.02, k = 0.02$, and the lower curve for $h = 0.05, k = 0.05$.
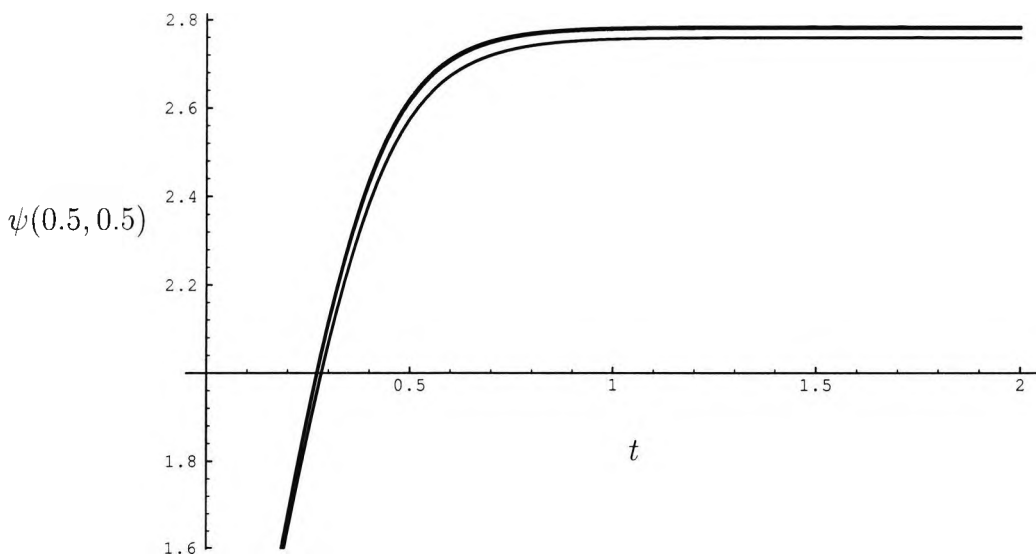
Figure 2.13: Value of the stream function at the centre of the cavity for $L = 1$ and $R = 500$ versus t for different grid sizes, where the upper curves are for $h = 0.01, k = 0.01$ and $h = 0.02, k = 0.02$, and the lower curve for $h = 0.05, k = 0.05$.
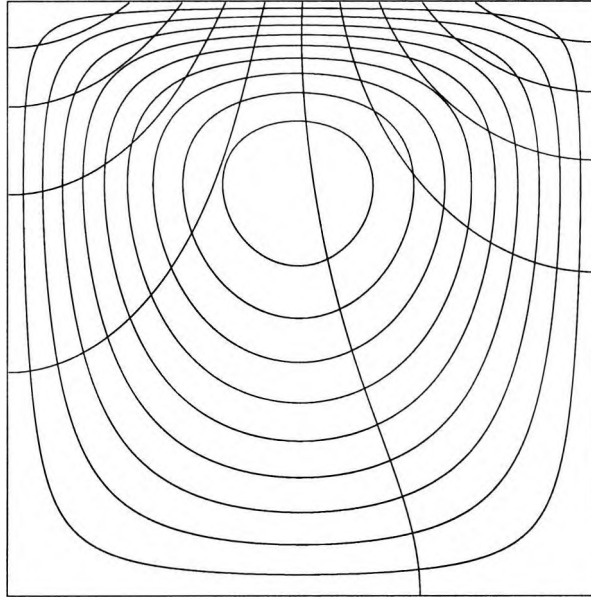
Figure 2.14: Contour plot of the temperature and stream function from the numerical solution for $L = 1$ and $R = 5$
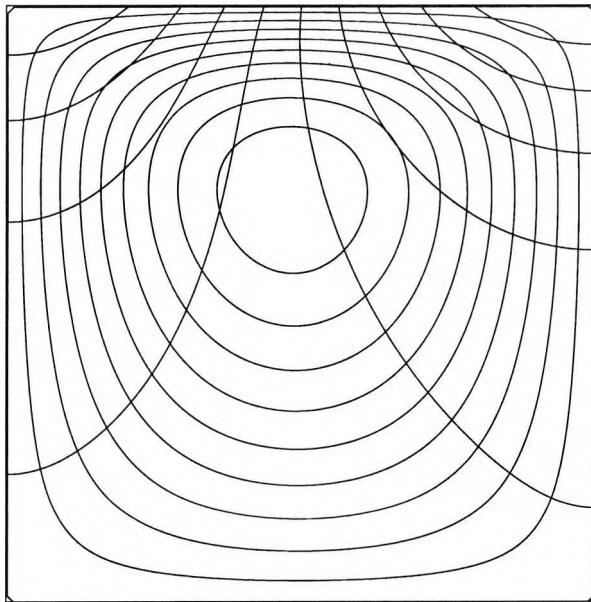
Figure 2.15: Contour plot of the temperature and stream function from the numerical solution for $L = 1$ and $R = 10$
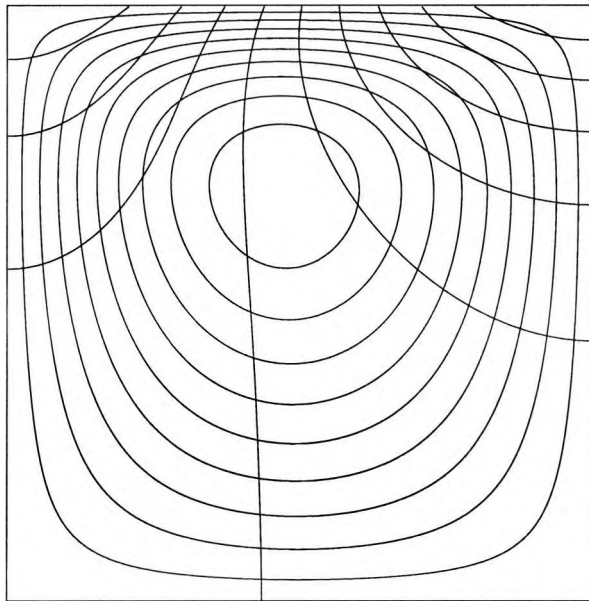
Figure 2.16: Contour plot of the temperature and stream function from the numerical solution for $L = 1$ and $R = 20$
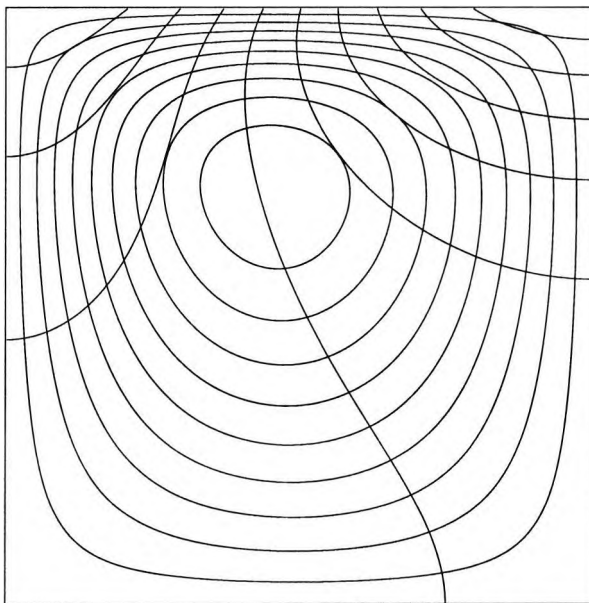
Figure 2.17: Contour plot of the temperature and stream function from the numerical solution for $L = 1$ and $R = 30$
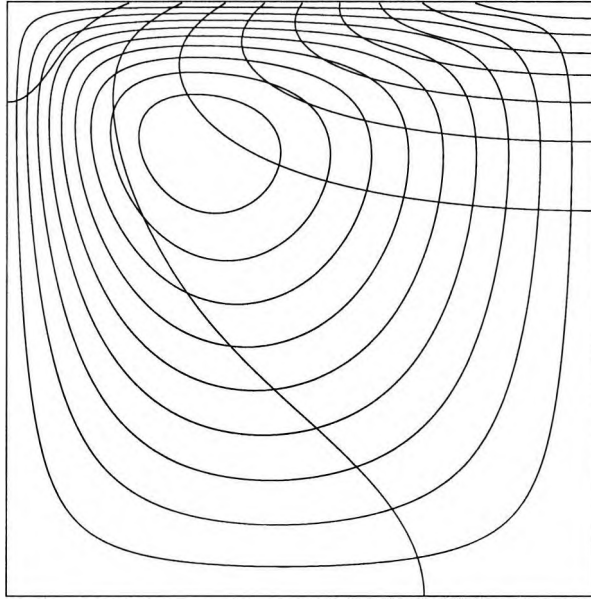
Figure 2.18: Contour plot of the temperature and stream function from the numerical solution for $L = 1$ and $R = 200$
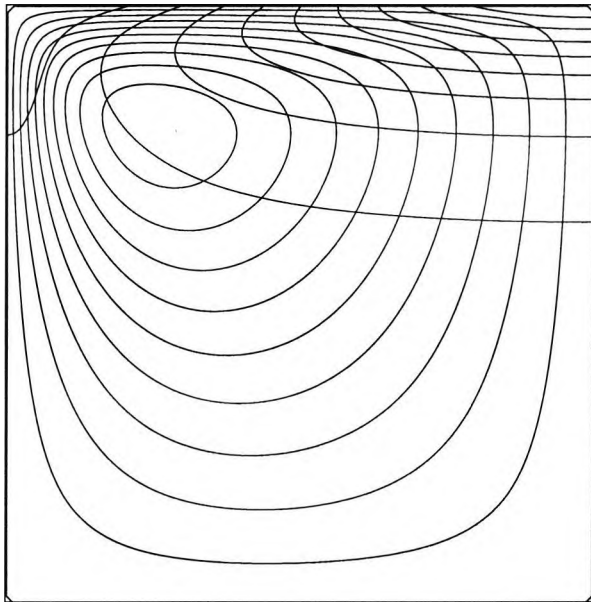
Figure 2.19: Contour plot of the temperature and stream function from the numerical solution for $L = 1$ and $R = 500$
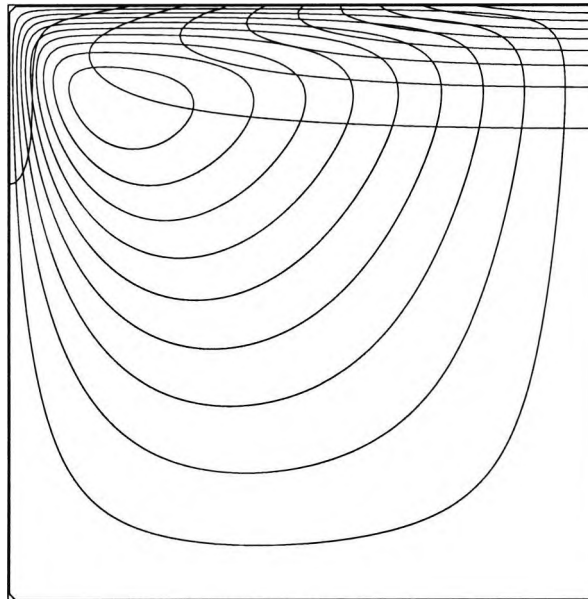
Figure 2.20: Contour plot of the temperature and stream function from the numerical solution for $L = 1$ and $R = 1500$
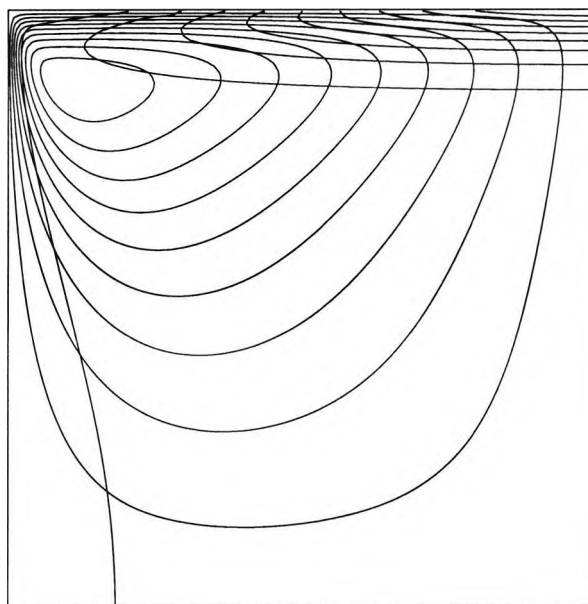
Figure 2.21: Contour plot of the temperature and stream function from the numerical solution for $L = 1$ and $R = 5000$
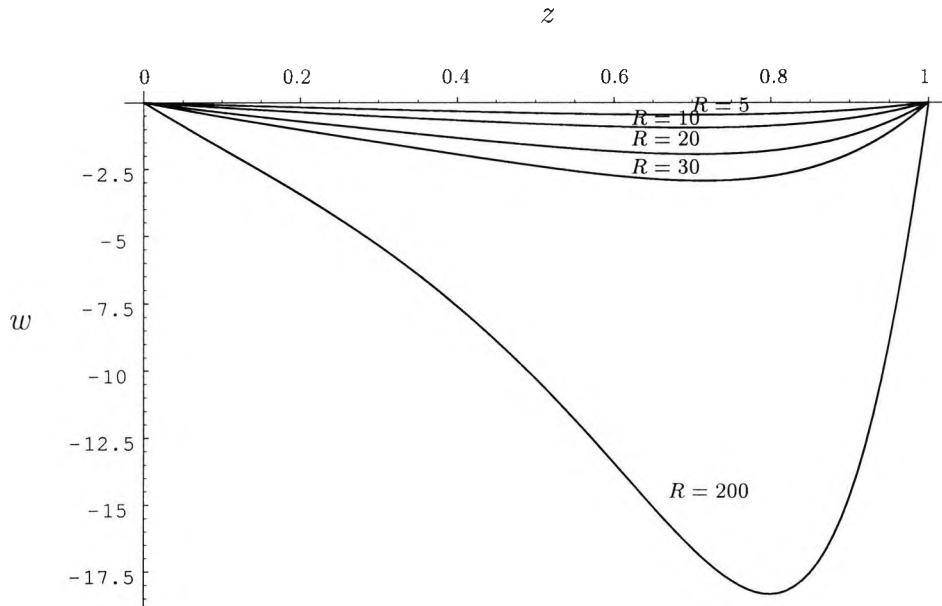
Figure 2.22: Slip velocity w for $L = 1$ and different values of R at the boundary $x = 0$ from the numerical calculation
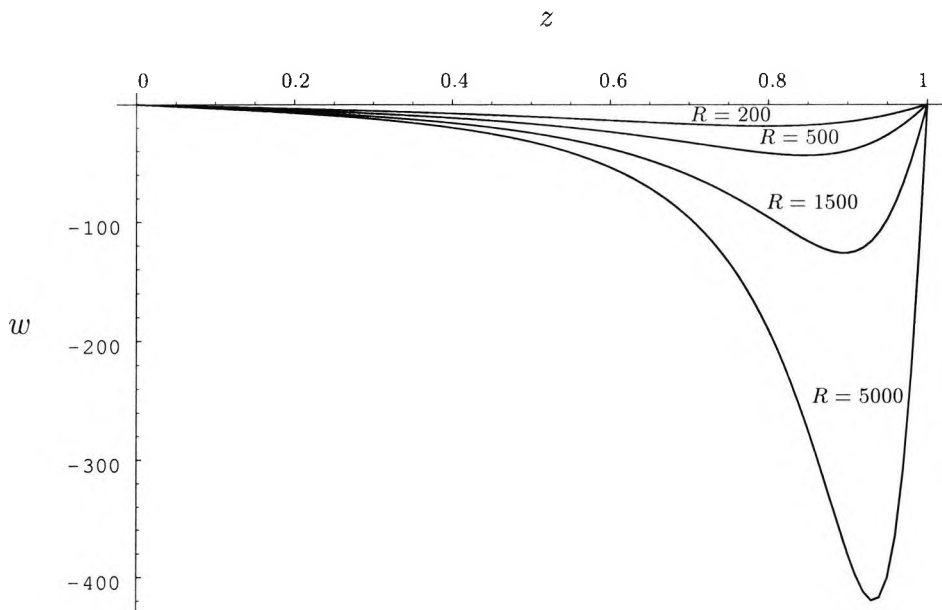
Figure 2.23: Slip velocity w for $L = 1$ and different values of R at the boundary $x = 0$ from the numerical calculation
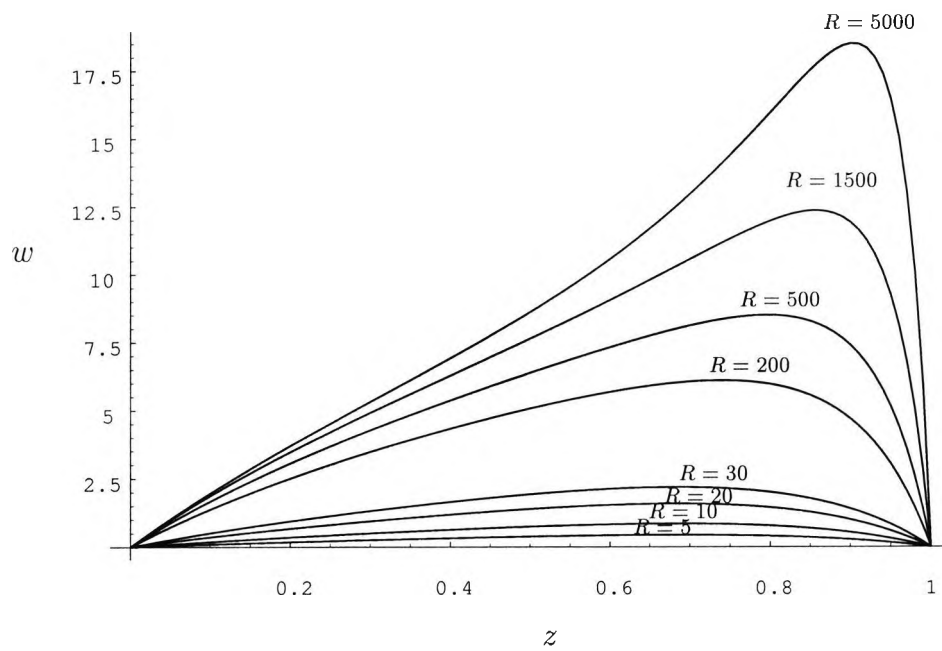
Figure 2.24: Slip velocity w for $L = 1$ and different values of R at the boundary $x = 1$ from the numerical calculation
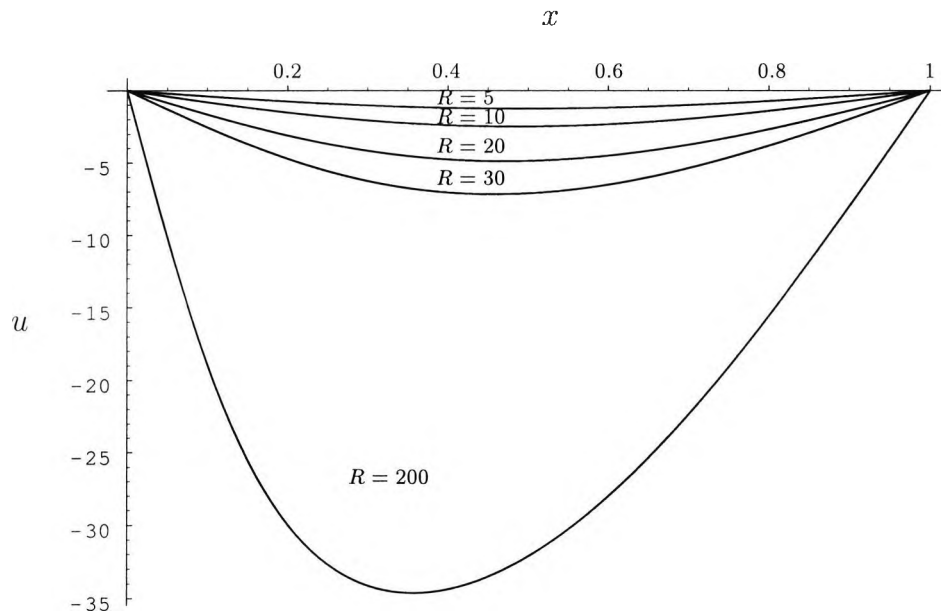
Figure 2.25: Slip velocity u for $L = 1$ and different values of R at the upper boundary $z = 1$ from the numerical calculation
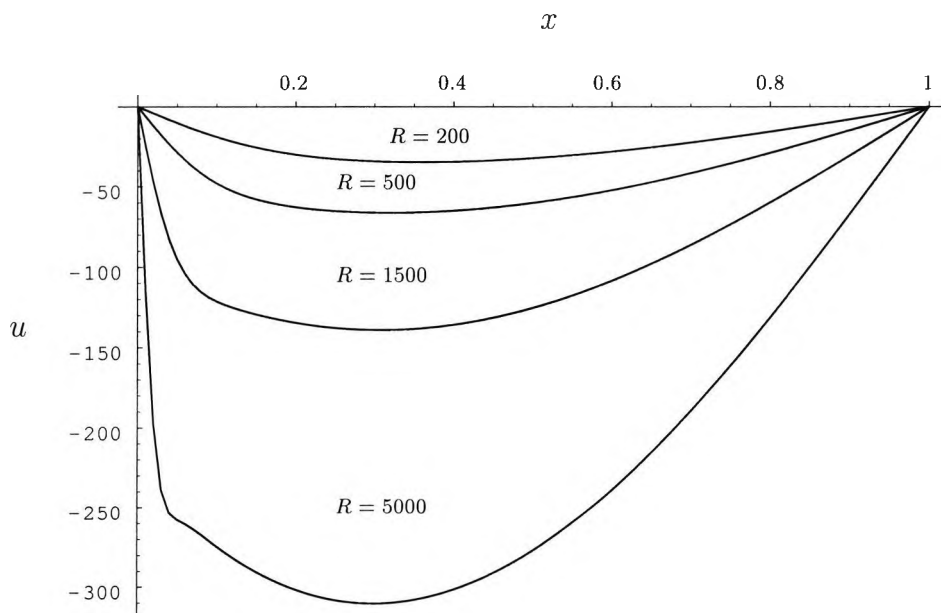
Figure 2.26: Slip velocity u for $L = 1$ and different values of R at the upper boundary $z = 1$ from the numerical calculation
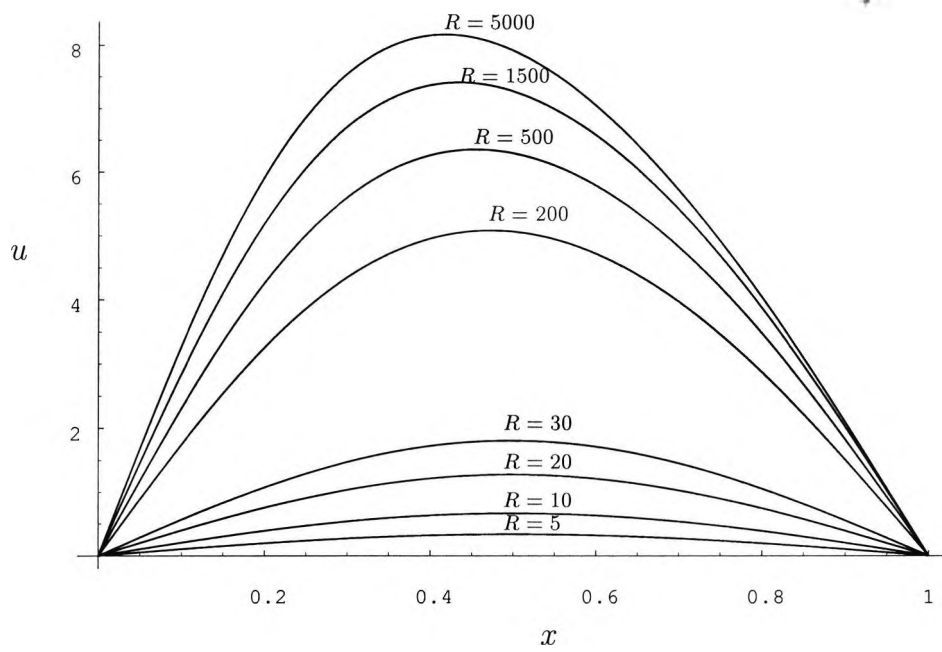
Figure 2.27: Slip velocity u for $L = 1$ and different values of R at the lower boundary $z = 0$ from the numerical calculation
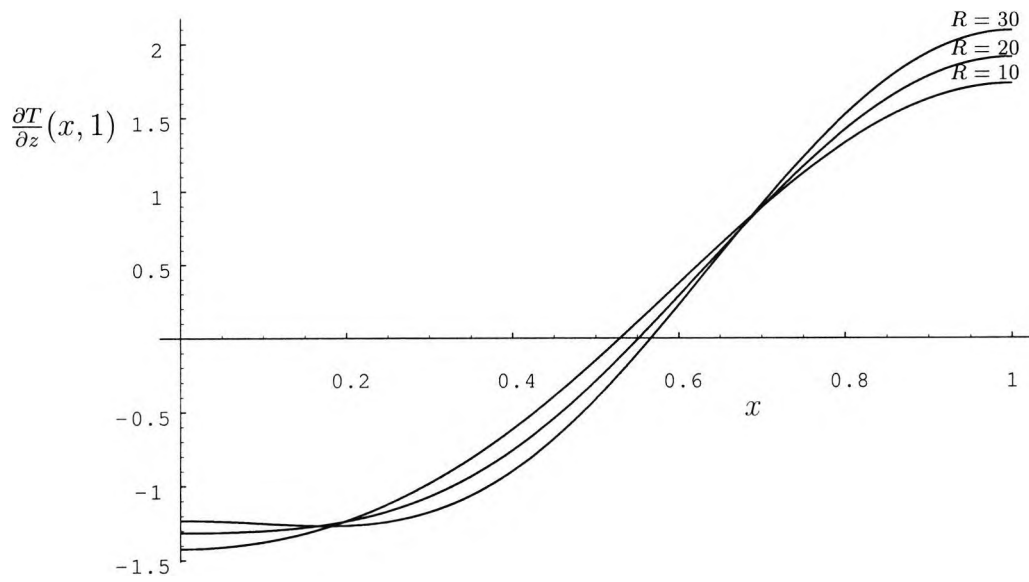
Figure 2.28: Local heat flux at the upper boundary $z = 1$ from the numerical calculation for $L = 1$ and different values of R.
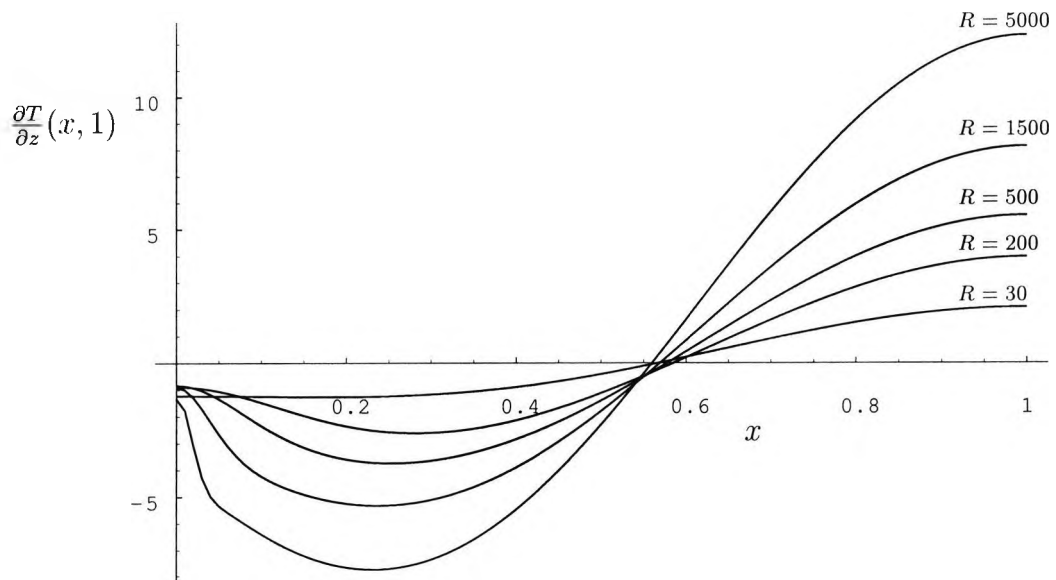
Figure 2.29: Local heat flux at the upper boundary $z = 1$ from the numerical calculation for $L = 1$ and different values of R
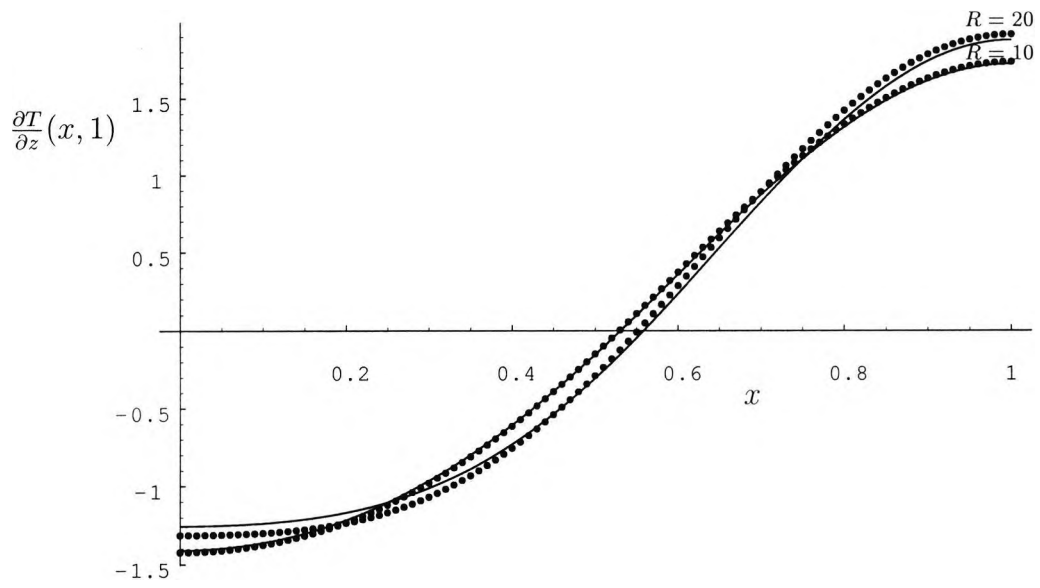
Figure 2.30: Comparison between the value of the local heat flux at the upper boundary $z = 1$ from the numerical calculation for $L = 1$ and the analytical calculation for small R, where the dotted curves represent the results from the numerical calculation
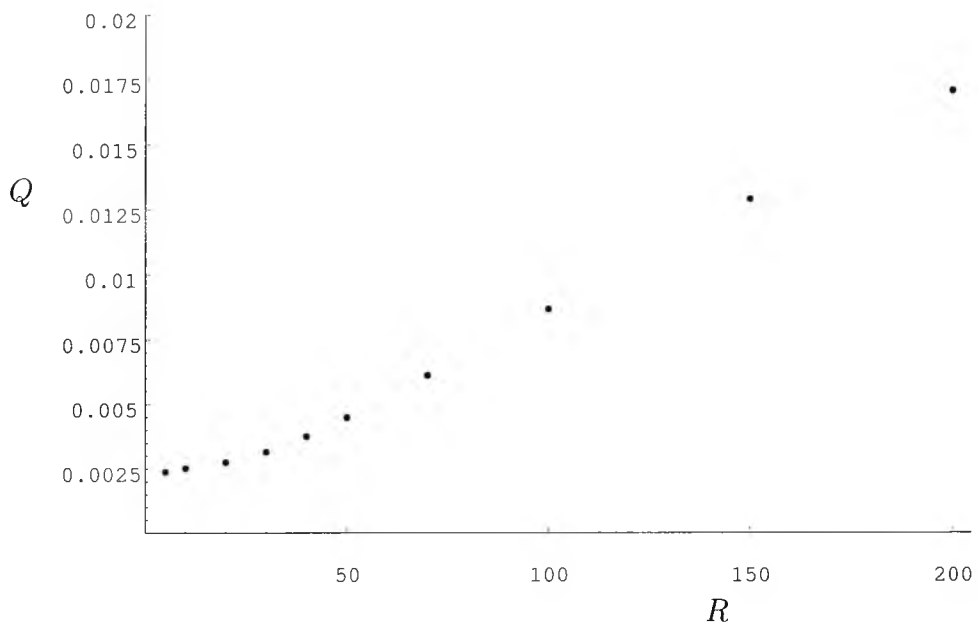
Figure 2.31: Total heat flux Q across the upper boundary $z = 1$ from the numerical calculation for $L = 1$ and various values of R
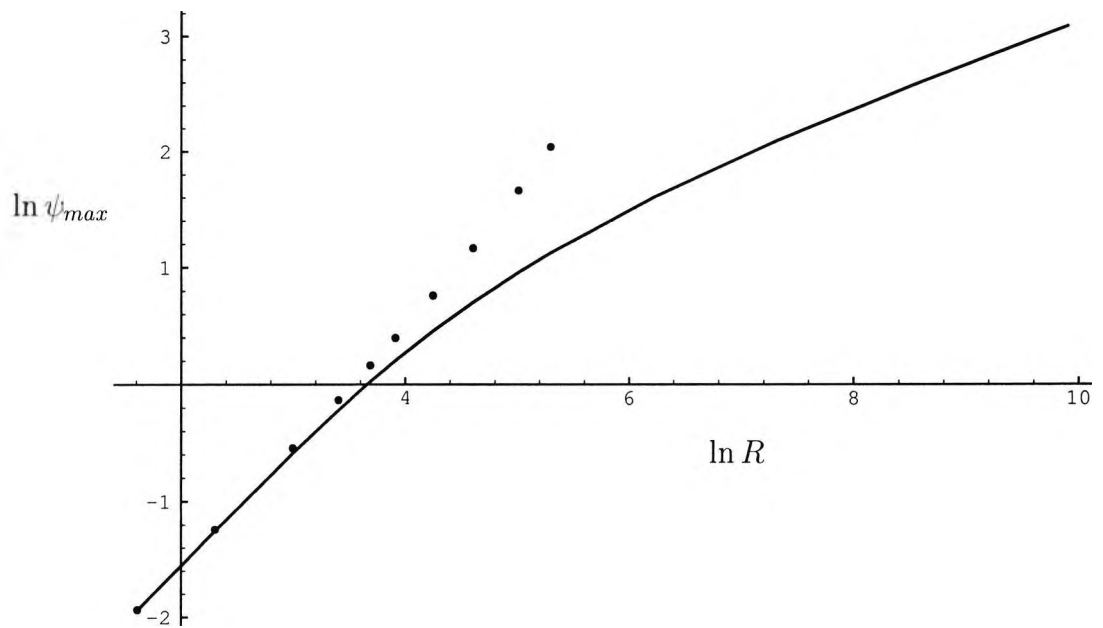
Figure 2.32: Graph of $\ln \psi_{max}$ versus $\ln R$ for $L = 1$ where the dotted curve is from the analytical calculation for small R and the full curve is from the numerical calculation
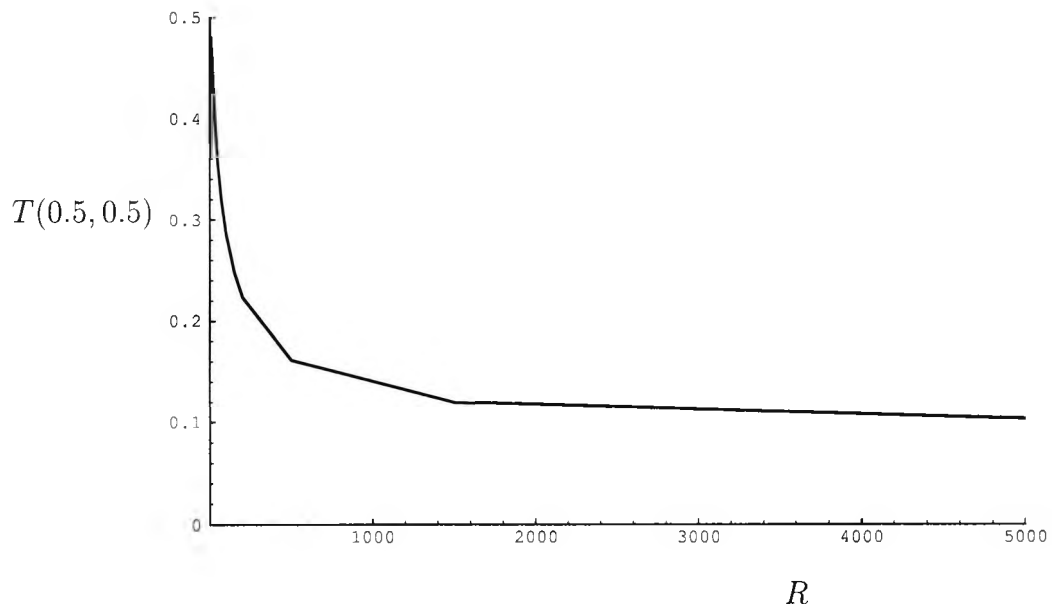
Figure 2.33: Temperature at the centre of the cavity versus R from the numerical calculation for $L = 1$
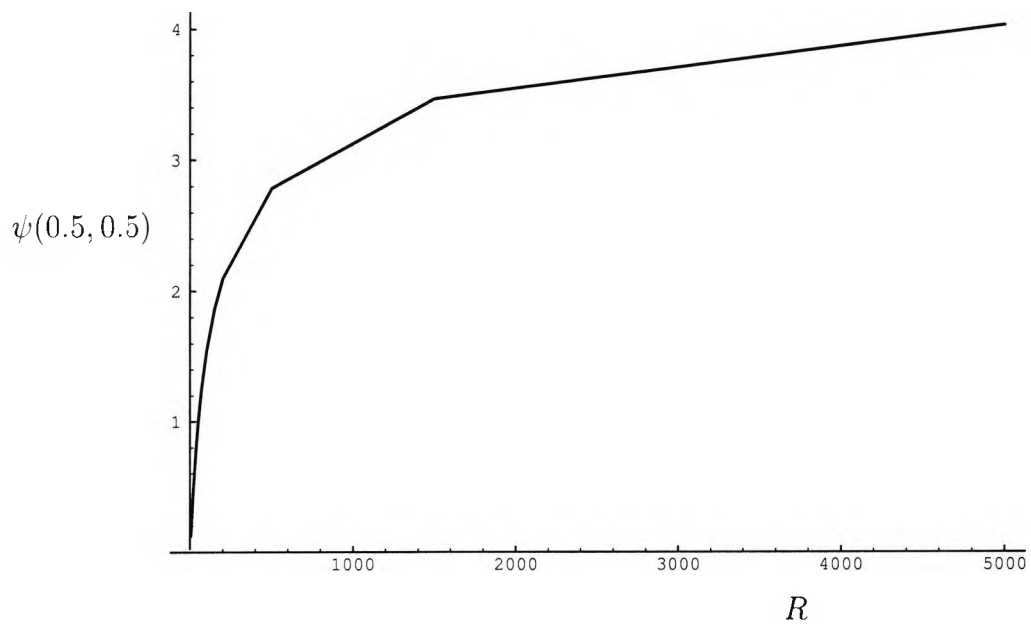
Figure 2.34: Stream function at the centre of the cavity versus R from the numerical calculation for $L = 1$

46
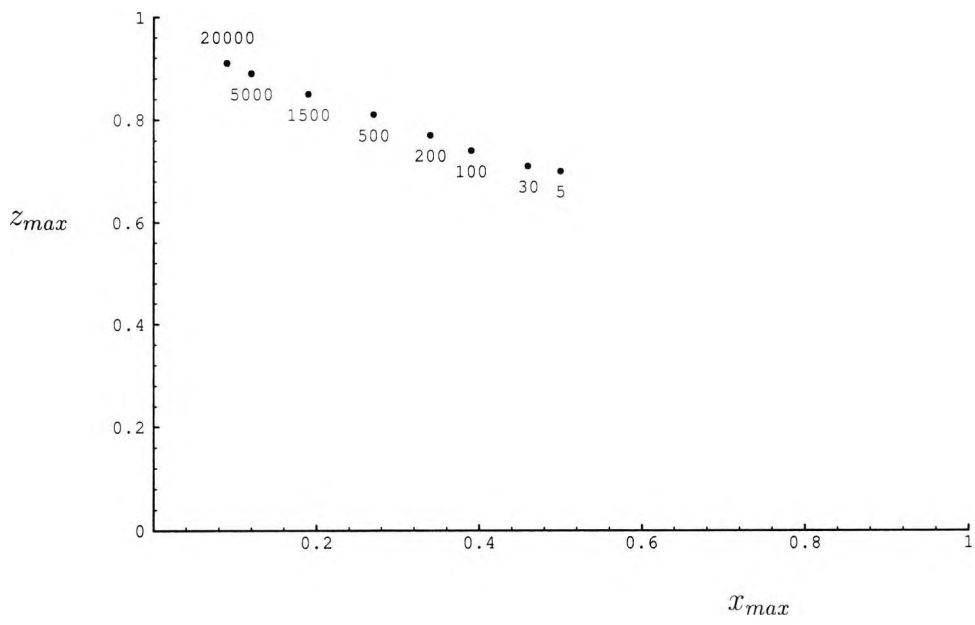
Figure 2.35: Position (x_{max}, z_{max}) of the maximum value of the stream function ψ_{max} for different values of R from the numerical calculation for $L = 1$
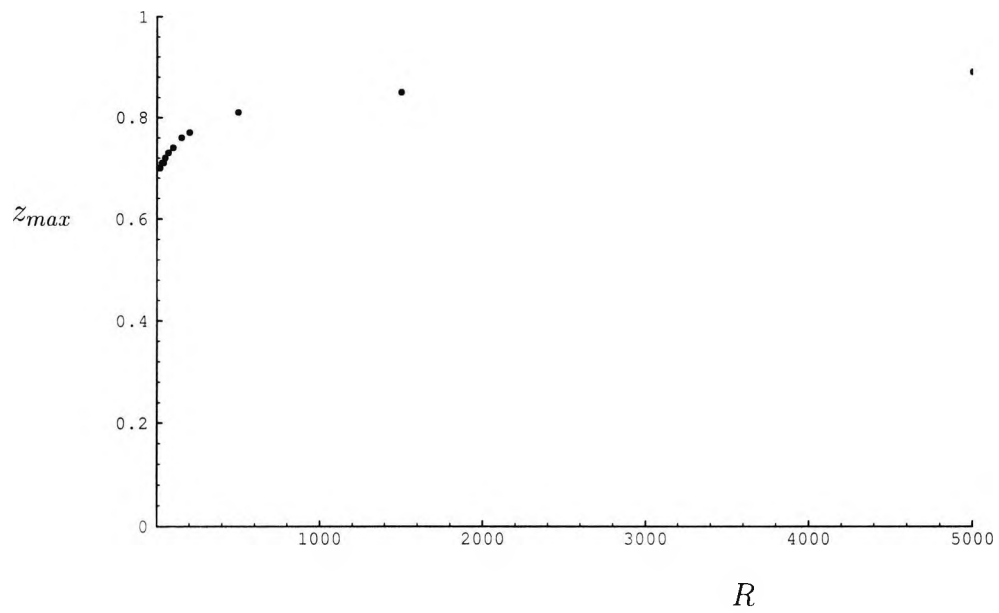
Figure 2.36: Position z_{max} of the maximum value of the stream function ψ_{max} versus R from the numerical calculation for $L = 1$
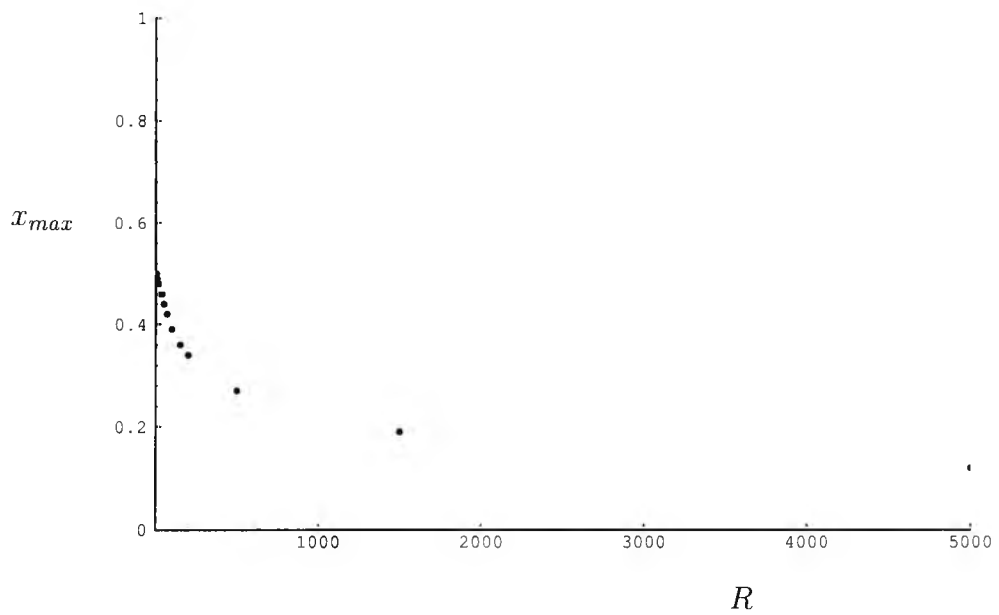
Figure 2.37: Position x_{max} of the maximum value of the stream function ψ_{max} versus R from the numerical calculation for $L = 1$
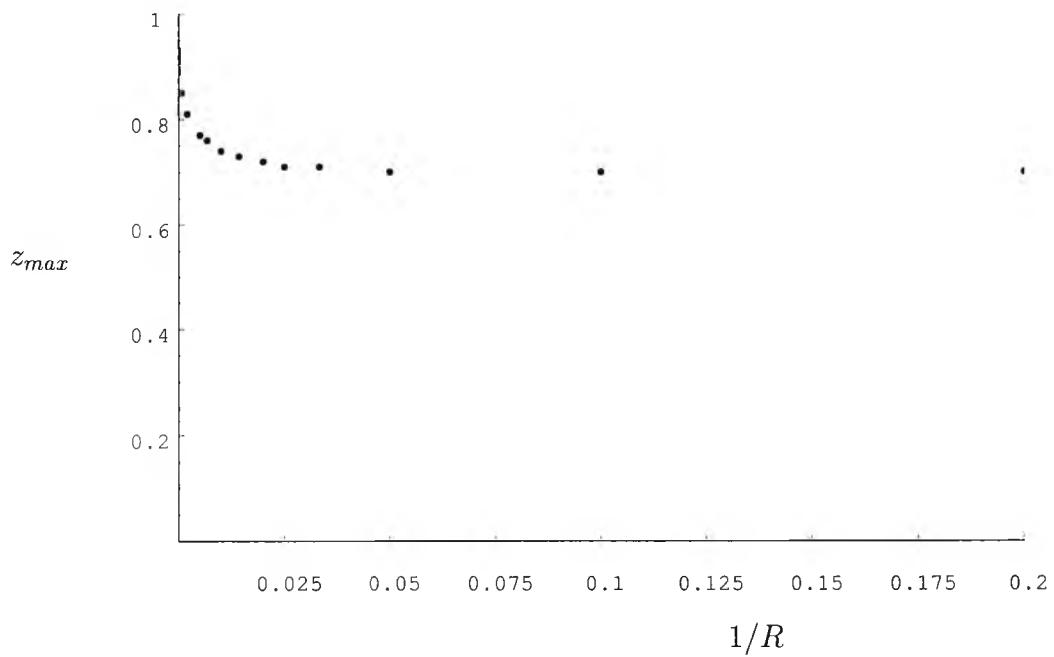
Figure 2.38: Position z_{max} of the maximum value of the stream function ψ_{max} versus $1/R$ from the numerical calculation for $L = 1$
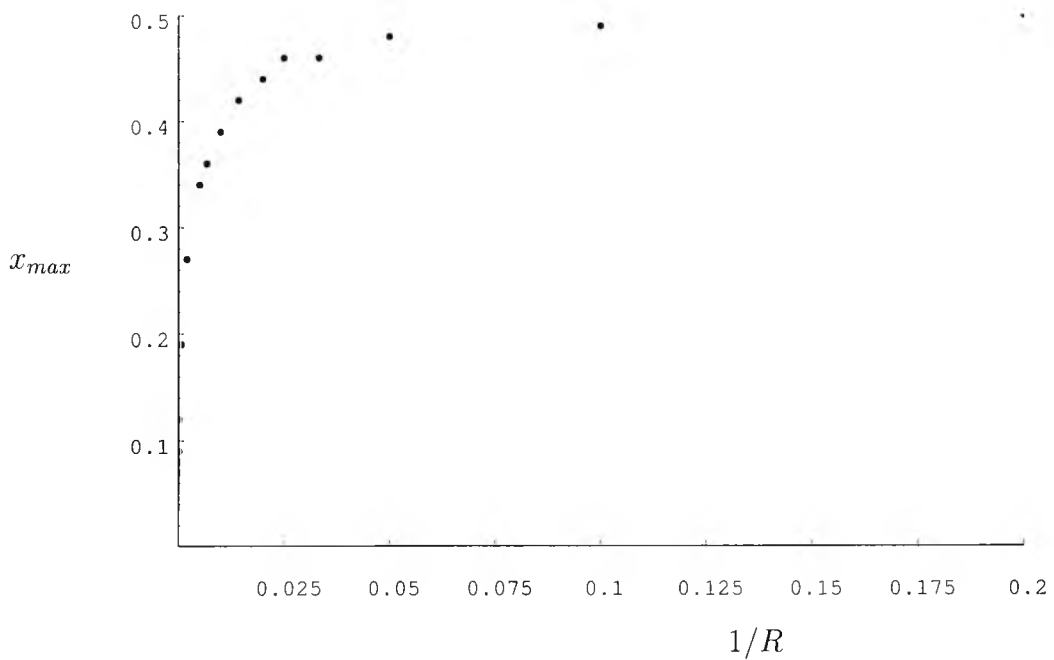
Figure 2.39: Position x_{max} of the maximum value of the stream function ψ_{max} versus $1/R$ from the numerical calculation for $L = 1$

Chapter 3

Further Solutions and Dependence on Aspect Ratio

3.1   Introduction

In this chapter the results are extended to a different temperature profile along the upper surface of the cavity and to a range of aspect ratios. At the upper boundary $z = 1$ the temperature is assumed to have the quadratic form

$$T = 1 - \frac{(x - L)^2}{L^2}, \quad 0 \leq x \leq L \tag{3.1.1}$$

so that, as with the cosine profile(2.1.1) it is monotonic and varies from zero at the cold end($x = 0$) to one at the hot end ($x = 1$). One reason for studying this quadratic profile is that it allows an exact solution of the horizontal boundary layer equations in the high Darcy-Rayleigh number limit, to be discussed in Chapter 4. This profile is also of interest in that unlike the cosine profile it is linear as it approaches the cold end ($x = 0$), implying a more sudden drop in temperature there and thus a more vigorous motion. Mathematically, it also implies a weak singularity in the thermal field in the corner ($x = 0, z = 1$) because the value of $\frac{\partial T}{\partial x}$ must adjust from the value $2/L$ given by(3.1.1) on $z = 1$ as $x \to 0+$ to the value $\frac{\partial T}{\partial x} = 0$ associated with the thermally insulated boundary, $x = 0$. From(2.1.2)-(2.1.6) the full system considered here consists of the equations

$$\nabla^2 \psi = -R\frac{\partial T}{\partial x}, \tag{3.1.2}$$

$$\nabla^2 T = \frac{\partial(T, \psi)}{\partial(x, z)} \tag{3.1.3}$$

together with (3.1.1) and the remaining boundary conditions

$$\psi = \frac{\partial T}{\partial x} = 0 \quad \text{on} \quad x = 0, L \tag{3.1.4}$$

$$\psi = 0 \quad \text{on} \quad z = 0, 1, \tag{3.1.5}$$

$$\frac{\partial T}{\partial z} = 0 \quad \text{on} \quad z = 0. \tag{3.1.6}$$

The solution for small Darcy-Rayleigh numbers is considered in Section 3.2 and numerical solutions for general Darcy-Rayleigh numbers are discussed in Section 3.3. Both tabular and graphical results are obtained for aspect ratios in the range $L = \frac{1}{4}$ to $L = 4$. The results are summarized in Section 3.4 .

3.2   Solution for small Darcy-Rayleigh numbers

The solution for the flow in the cavity for small Darcy-Rayleigh numbers R where the upper boundary temperature has the quadratic form (3.1.1) can be obtained by assuming

$$T(x, z) = T_0(x, z) + \cdots \tag{3.2.1}$$

$$\psi(x, z) = R\psi_1(x, z) + \cdots \tag{3.2.2}$$

As in Section 2.2, the leading order temperature field $T_0(x, z)$ satisfies Laplace's equation

$$\frac{\partial^2 T_0}{\partial x^2} + \frac{\partial^2 T_0}{\partial z^2} = 0, \tag{3.2.3}$$

which must now be solved subject to the boundary conditions

$$\frac{\partial T_0}{\partial x} = 0 \quad \text{on} \quad x = 0, L, \tag{3.2.4}$$

$$\frac{\partial T_0}{\partial z} = 0 \quad \text{on} \quad z = 0, \tag{3.2.5}$$

$$T_0 = 1 - \frac{(x - L)^2}{L^2} \quad \text{on} \quad z = 1. \tag{3.2.6}$$

The solution is found using a cosine series in x in order to satisfy the boundary conditions (3.2.4), and has the form

$$T_0 = \frac{2}{3} + \sum_{n=1}^{\infty} C_n \cos \frac{n\pi x}{L} \cosh \frac{n\pi z}{L} \tag{3.2.7}$$

where

$$C_n = -\frac{4}{(n\pi)^2} \operatorname{sech} \frac{n\pi}{L}. \tag{3.2.8}$$

The leading order stream function ψ_1 satisfies Poisson's equation

$$\frac{\partial^2 \psi_1}{\partial x^2} + \frac{\partial^2 \psi_1}{\partial z^2} = -\frac{\partial T_0}{\partial x}, \tag{3.2.9}$$

where T_0 is given by (3.2.7). This must be solved subject to the boundary conditions

$$\psi_1 = 0 \quad \text{on} \quad x = 0, L, \qquad \psi_1 = 0 \quad \text{on} \quad z = 0, 1. \tag{3.2.10}$$

Here the solution can be constructed as a sine series in x and is composed of a particular integral which balances the right-hand side of (3.2.9) together with a complementary function which ensures that the boundary conditions at $z = 0$ and $z = 1$ are satisfied. The solution is found to be

$$\psi_1 = \sum_{n=1}^{\infty} \frac{C_n}{2} (z - 1) \sinh \frac{n\pi z}{L} \sin \frac{n\pi x}{L} \tag{3.2.11}$$

where C_n is given by (3.2.8).

The solutions for T_0 and ψ_1 are both infinite series in this case, in contrast to the previous case (Section 2.2) where the temperature at the upper boundary is a cosine function and only one mode of the cosine and sine series for T_0 and ψ_0 (respectively) are generated, as shown in (2.2.8) and (2.2.12). We see that there is now no symmetry about $x = \frac{L}{2}$ in either the temperature field T_0 or the stream function ψ_1, unlike the previous case. The centre of the eddy, where ψ_1 attains its maximum value of 0.02342 is at $x = 0.44$, $z = 0.69$ when $L = 1$, and is thus closer to the cold end of the cavity than in the previous case.

Plots of the isotherms and the streamlines predicted by this analysis are shown

for $R = 5$ and $L = 1$ in figure 3.1. Both the isotherms and the centre of circulation are seen to be closer to the cold side than in the corresponding result for the cosine function shown in figure 2.4. However, the overall pattern of isotherms and streamlines is similar in each case. Results predicted by the analysis of this section for other aspect ratios in the range $\frac{1}{4} \leq L \leq 4$ and $R = 5$ are shown in figures 3.2 and 3.3.

3.3 Numerical results for general Darcy-Rayleigh numbers

The same numerical method as described in Section 2.4 was used to calculate solutions of the system of equations (3.1.2), (3.1.3) with boundary conditions (3.1.1) and (3.1.4)-(3.1.6) for general Darcy-Rayleigh numbers. Most computations were carried out with step sizes of 0.01 in both the x and z directions and a time step of 10^{-5}. In all cases it was found that 2×10^5 time steps were sufficient to reach a steady-state, equivalent to $t = 2$. The initial state at $t = 0$ was taken to be $T = 0$, $\psi = 0$ at all internal points in the cavity.

3.3.1 Results for a square cavity, $L = 1$.

Numerical values of the steady state solution at various reference points in the cavity are displayed in table 3.1 for values of R equal to 5, 30, 200, 500, 1500 and 5000. Also shown are the position and value of the maximum value of the stream function and the corresponding value of the temperature at that point.

Isotherms and streamlines are shown in figures 3.4 - 3.15. The results for $R = 5$ shown in figures 3.4 and 3.5 are in excellent agreement with the small R analysis. We see that as the value of R increases (figures 3.6 - 3.15) the isotherms migrate towards the hot end and the centre of circulation moves towards the cold end, leaving the temperature in the lower part of cavity at a value of around 0.23-0.24 in the limit of large R. This can be seen in figure 3.14 and in more detail in figure 3.16. The overall structure of the solution is similar to that of the previous results of Chapter 2, where the temperature at the upper boundary is a cosine function, although the temperature in the lower region in the limit of large R is slightly lower (< 0.2) in the previous case.
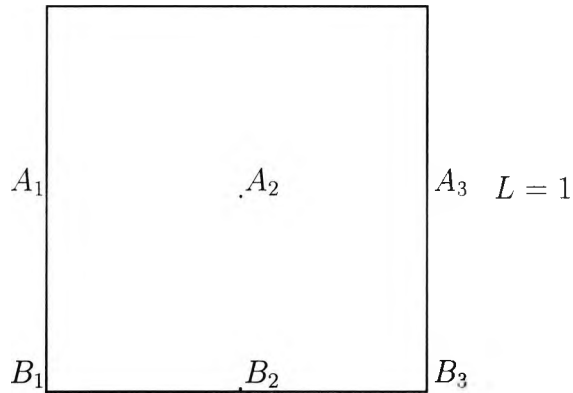
R	5	30	200	500	1500	5000
ψ_{A2}	0.100642	0.584468	2.034072	2.764080	3.494969	4.084355
T_{A2}	0.656712	0.591581	0.394221	0.310195	0.251687	0.236864
T_{A1}	0.556830	0.484798	0.328248	0.274621	0.238047	0.232662
T_{A3}	0.735051	0.659985	0.416885	0.318704	0.253339	0.236738
T_{B1}	0.612686	0.533341	0.346509	0.283131	0.241108	0.233620
T_{B2}	0.648512	0.566640	0.359310	0.288660	0.242871	0.234105
T_{B3}	0.683464	0.602136	0.376120	0.296274	0.245264	0.234708
ψ_{max}	0.117937	0.699686	3.029098	5.032325	8.440277	13.860153
T at ψ_{max}	0.638297	0.586046	0.433103	0.375387	0.329827	0.312290
x_{max}, z_{max}	(0.43,0.69)	(0.40,0.70)	(0.27,0.76)	(0.20,.81)	(0.13,.86)	(0.08,.90)

Table 3.1: Numerical results for $L = 1$

3.3.2 Results for tall cavities, $L < 1$.

Numerical calculations for taller cavities were carried out for two aspect ratios $L = 0.25$ and $L = 0.5$. Numerical values of the steady-state solution at various reference points in the cavity for $L = 0.25$ are shown in table 3.2 and isotherms and streamlines are displayed for $R = 5, 30, 200, 500, 1500$ and 5000 in figures 3.17 - 3.22. The results for $R = 5$ are in good agreement with the small R analysis (figure 3.3). We see that most of the variation occurs in the upper part

54

$$L = 0.25$$

Table 3.2: Numerical results for $L = 0.25$
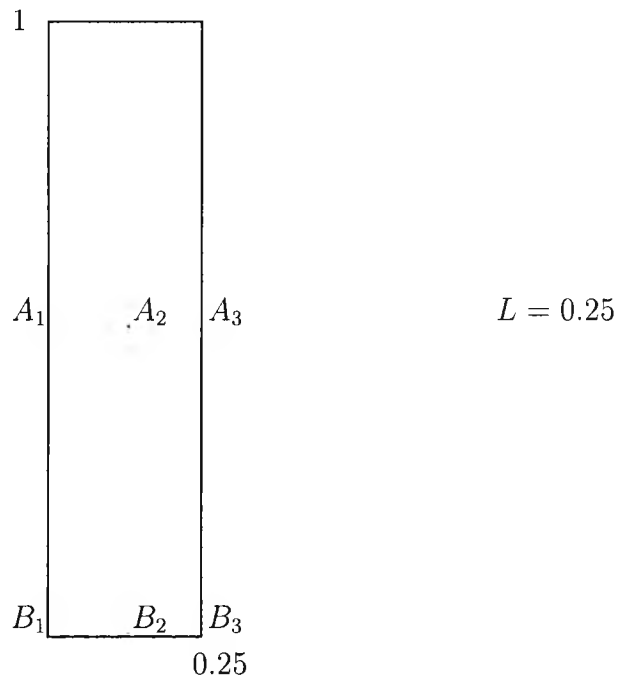
R	5	30	200	500	1500	5000
ψ_{A2}	0.000944	0.005722	0.033301	0.055332	0.072721	0.078472
T_{A2}	0.662393	0.641186	0.516368	0.413588	0.322736	0.278668
T_{A1}	0.661680	0.640465	0.515743	0.413188	0.322576	0.278620
T_{A3}	0.663200	0.642000	0.517063	0.414029	0.322911	0.278713
T_{B1}	0.661892	0.640715	0.516186	0.413522	0.322699	0.278628
T_{B2}	0.661895	0.640718	0.516188	0.413523	0.322700	0.278628
T_{B3}	0.661898	0.640721	0.516191	0.413525	0.322701	0.278628
ψ_{max}	0.029523	0.178483	1.110682	2.231225	4.271912	7.653702
T at ψ_{max}	0.651209	0.641041	0.549390	0.476495	0.415317	0.356216
x_{max}, z_{max}	(0.11,0.92)	(0.11,0.92)	(0.09,0.93)	(0.08,0.93)	(0.06,0.95)	(0.04,0.96)

Table 3.2: Numerical results for $L = 0.25$

of the cavity as R increases and a horizontal boundary layer structure develops as $R \to \infty$. The temperature in the lower part of the cavity in the limit of large R is between 0.27 and 0.28, and the isotherms there for $R = 5000$ can be seen in more detail in figure 3.23. The corresponding results for the case $L = 0.5$ are shown in table 3.3 and figures 3.24 - 3.30.

1

A_1 A_2 A_3 $L = 0.5$

B_1 B_2 B_3

0.5
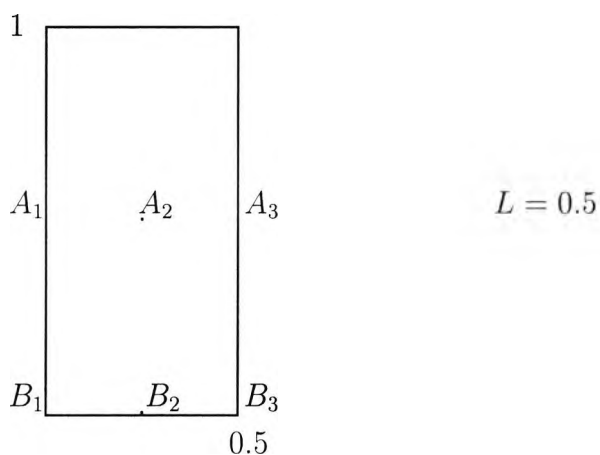
R	5	30	200	500	1500	5000
ψ_{A2}	0.021927	0.132274	0.604564	0.862543	1.070963	1.193139
T_{A2}	0.657565	0.615215	0.435155	0.342707	0.274151	0.250765
T_{A1}	0.639429	0.596431	0.421738	0.335426	0.271487	0.250007
T_{A3}	0.674743	0.632053	0.444619	0.347122	0.275512	0.251079
T_{B1}	0.655163	0.612105	0.431217	0.340099	0.273074	0.250438
T_{B2}	0.656689	0.613638	0.432179	0.340582	0.273239	0.250482
T_{B3}	0.658212	0.615175	0.433163	0.341080	0.273408	0.250527
ψ_{max}	0.059558	0.360278	1.930214	3.459962	6.129371	10.419395
T at ψ_{max}	0.648037	0.617785	0.486767	0.417138	0.356994	0.328509
x_{max}, z_{max}	(0.22,0.84)	(0.21,0.84)	(0.16,0.86)	(0.13,0.88)	(0.09,0.91)	(0.05,0.94)

Table 3.3: Numerical results for $L = 0.5$

3.3.3 Results for shallow cavities, $L > 1$

Numerical calculations for shallow cavities were also investigated for two aspect ratios, $L = 2$ and $L = 4$. Numerical values of the temperature and stream function at various reference points are shown in table 3.4 for $L = 2$ and the isotherms and streamlines for various values of R are displayed in figures 3.31 - 3.36. Results for $R = 5$ in figure 3.31 agree well with the small R analysis(figure 3.2). More detailed isotherms in the lower part of the cavity for $R = 5000$ are shown in figure 3.37. Corresponding results for an aspect ratio $L = 4$ are shown in table 3.5 and figures 3.38 - 3.44. Notice here that the shallow geometry makes the development of a horizontal boundary layer structure as $R \to \infty$ less evident than in the previous case, although its emergence is clearly indicated in the results for $R = 5000$ shown in figures 3.43 and 3.44.

For moderate and small values of R and very shallow cavities ($L \gg 1$) the isotherms align almost vertically in the middle section of the cavity, as shown for $L = 4$ and $R = 5$ in figure 3.38, and the streamlines are approximately symmetrical about the horizontal line $z = \frac{1}{2}$. This reflects the fact that the z derivatives on the left-hand sides of (3.1.2) and (3.1.3) dominate the x derivatives in this limit, and the relevant solution thoughout most of the cavity ($0 < \frac{x}{L} \leq 1, 0 \leq z \leq 1$) is

$$T \sim 1 - (\frac{x}{L} - 1)^2, \qquad \psi \sim \frac{Rz}{L}(1 - z)(1 - \frac{x}{L}). \tag{3.3.1}$$

An inner solution near $x/L = 0$ is necessary to allow ψ to adjust to zero at the cold end wall, but the details are not considered here.

```
1       ┌─────────────────────────────────────┐
        │                                     │
A₁      │              A₂                     │  A₃  L = 2
        │                                     │
B₁      └─────────────────────────────────────┘  B₃
                        B₂
                                          2
```
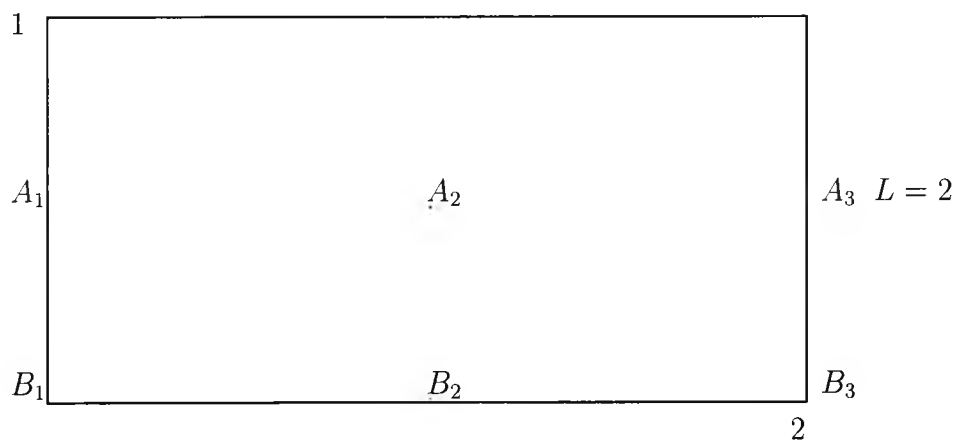
R	5	30	200	500	1500	5000
ψ_{A2}	0.171382	0.954399	3.098205	4.388374	5.992555	7.573549
T_{A2}	0.672782	0.605718	0.416770	0.326718	0.257741	0.234563
T_{A1}	0.403675	0.333748	0.245124	0.223516	0.212824	0.219693
T_{A3}	0.847273	0.763870	0.479277	0.355945	0.266952	0.235889
T_{B1}	0.470041	0.383329	0.265650	0.234878	0.217864	0.221616
T_{B2}	0.647676	0.529180	0.316333	0.257728	0.225613	0.223919
T_{B3}	0.800721	0.697852	0.402883	0.300467	0.240080	0.227571
ψ_{max}	0.180961	1.033586	4.112726	6.752359	11.172470	18.078587
T at ψ_{max}	0.604932	0.533863	0.383803	0.338168	0.306067	0.295019
x_{max}, z_{max}	(0.79,0.56)	(0.72,0.57)	(0.43,0.65)	(0.30,0.71)	(0.20,0.77)	(0.12,0.83)

Table 3.4: Numerical results for $L = 2$

1

A_1 $.A_2$ A_3 $L = 4$

B_1 $.B_2$ B_3

4
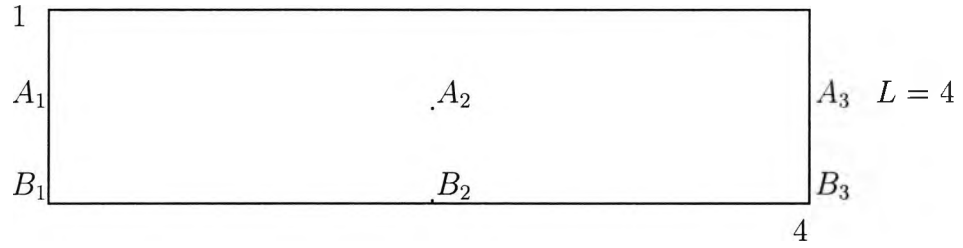
R	5	30	200	500	1500	5000
ψ_{A2}	0.142369	0.846964	3.522609	5.511643	8.332968	11.762621
T_{A2}	0.704617	0.652744	0.494190	0.400635	0.308188	0.253876
T_{A1}	0.244860	0.204832	0.160752	0.164277	0.181400	0.203643
T_{A3}	0.949152	0.919195	0.660494	0.490519	0.344591	0.264704
T_{B1}	0.291744	0.240495	0.179283	0.176843	0.188552	0.207033
T_{B2}	0.683537	0.580946	0.336233	0.257919	0.218717	0.216280
T_{B3}	0.932064	0.891926	0.585507	0.410249	0.283840	0.235788
ψ_{max}	0.164882	0.937143	4.251990	7.617726	13.529162	22.714008
T at ψ_{max}	0.512657	0.475739	0.330235	0.292985	0.281880	0.284960
x_{max}, z_{max}	(1.26,0.52)	(1.27,0.52)	(0.76,0.58)	(0.47,0.63)	(0.29,0.68)	(0.17,0.75)

Table 3.5: Numerical results for $L = 4$

3.4 Summary

From the numerical results for a range of aspect ratios L and various values of R, we see that the solutions possess the same general features as those found in Chapter 2 for square cavities. In particular, the results indicate the formation of a horizontal boundary layer in the upper part of the cavity as R increases, leaving the bottom part of the cavity with an almost constant temperature in the region of 0.2 - 0.3 in the limit of large R. This limiting value appears to be largely independent of aspect ratio. The main feature of the flow pattern is the migration of the centre of circulation towards the upper end of the cold wall as R increases.
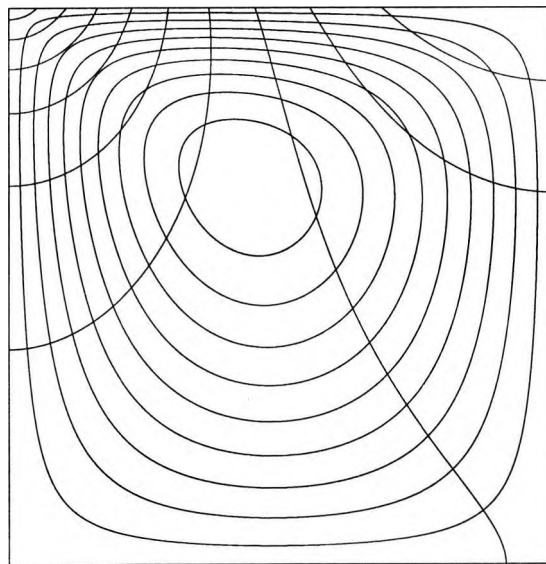
Figure 3.1: Isotherms and streamlines from the small R analysis for $R = 5$ and $L = 1$
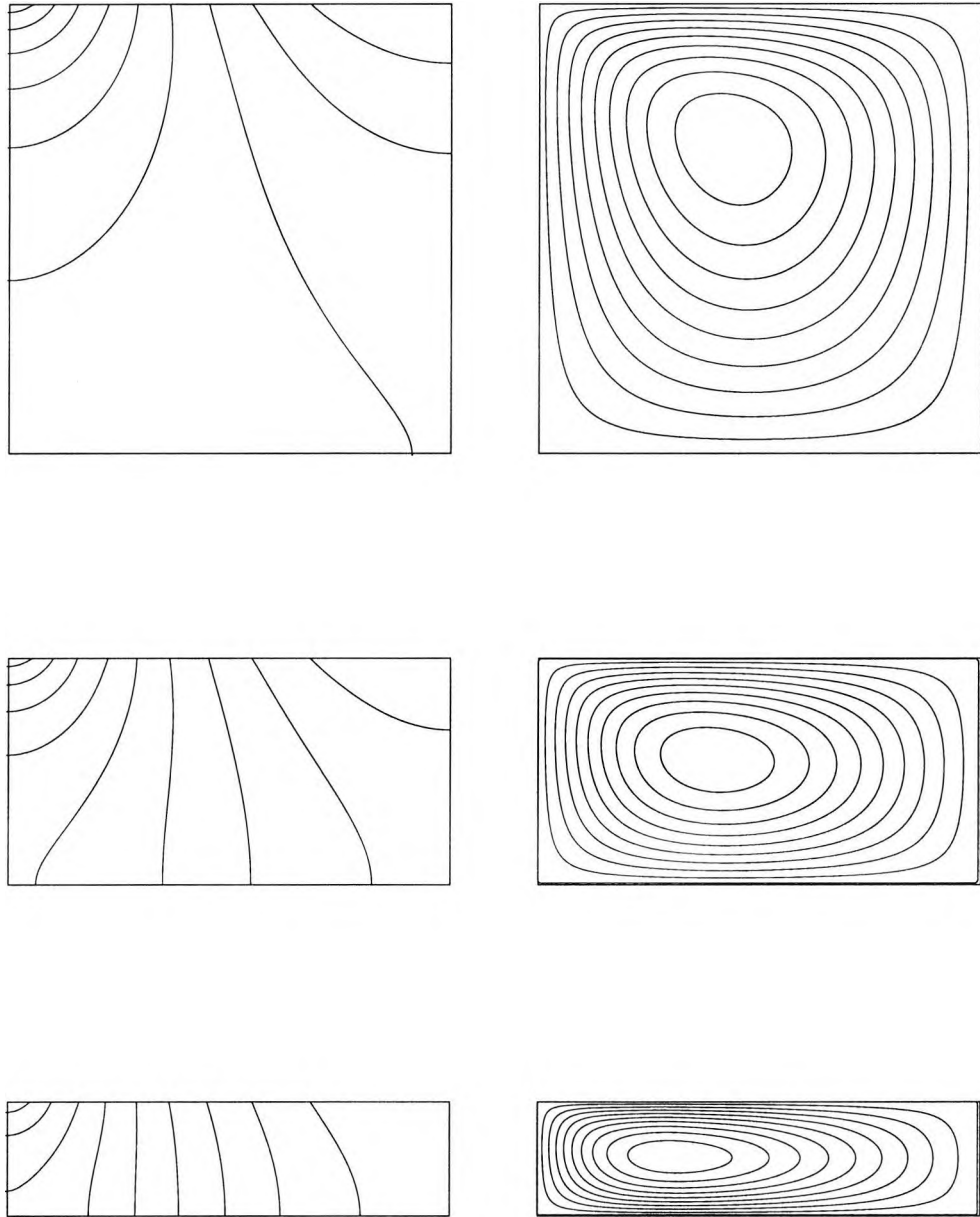
Figure 3.2: Isotherms and streamlines from the small R analysis for $R = 5$ and aspect ratios $L = 1, 2, 4$
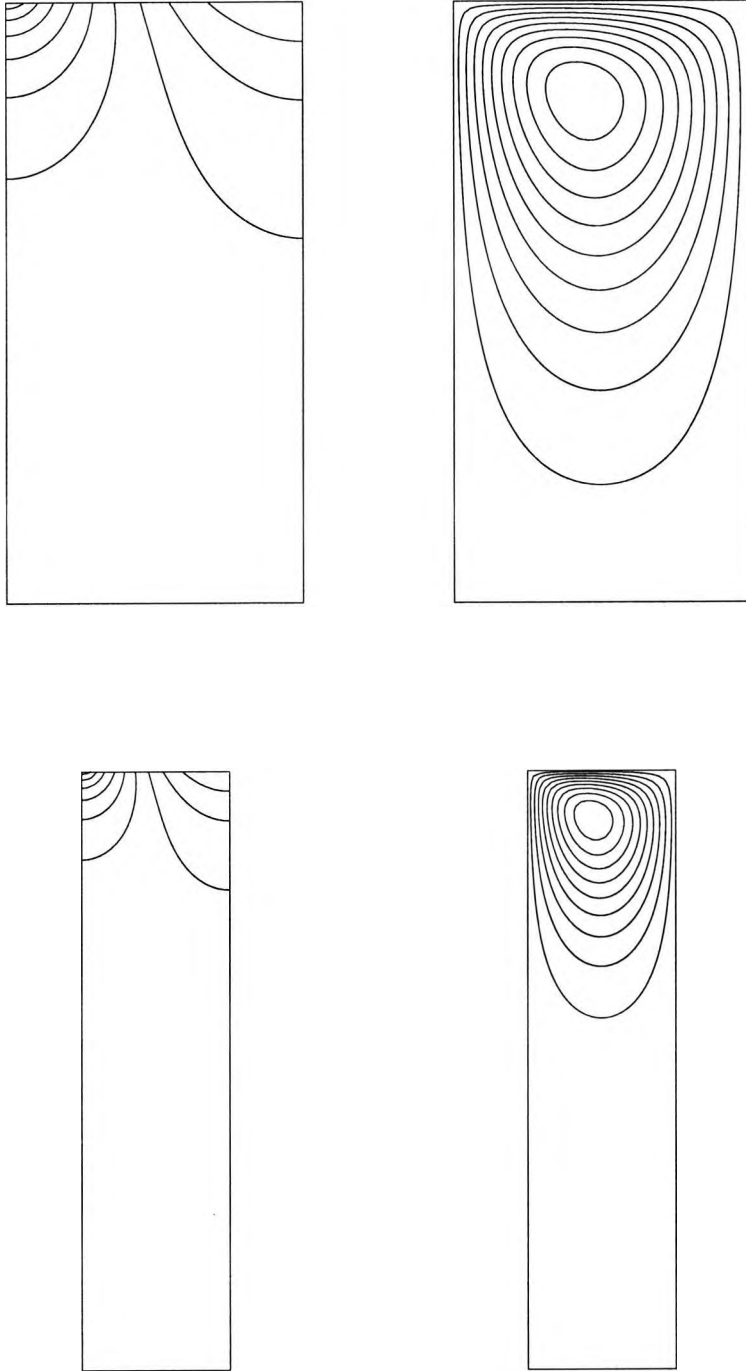
Figure 3.3: Isotherms and streamlines from the small R analysis for $R = 5$ and aspect ratios $L = 0.5, 0.25$
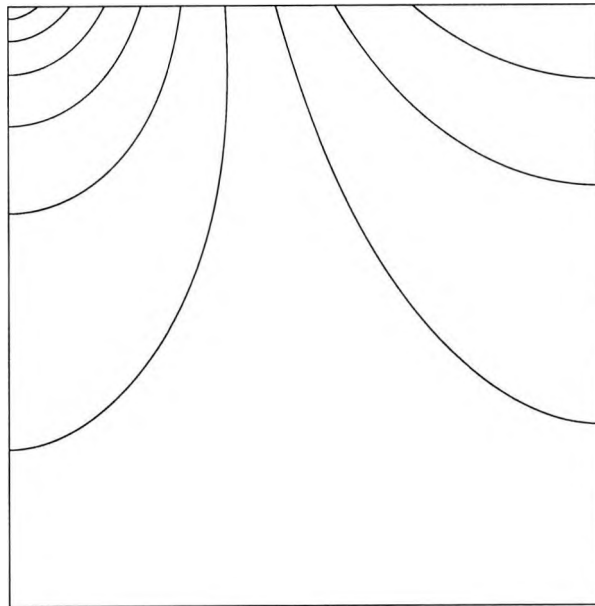
Figure 3.4: Isotherms from the numerical calculation for $R = 5$ and $L = 1$
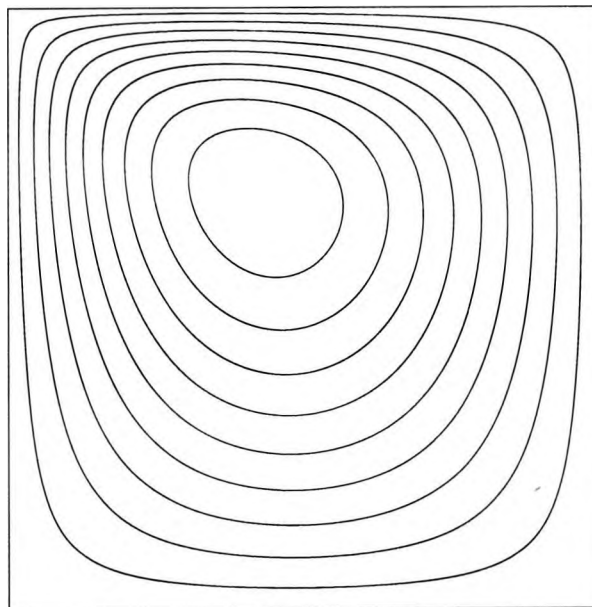
Figure 3.5: Streamlines from the numerical calculation for $R = 5$ and $L = 1$
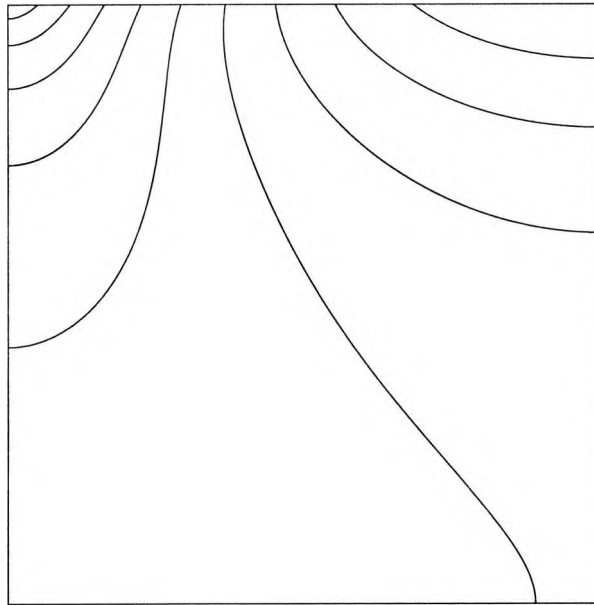
Figure 3.6: Isotherms from the numerical calculation for $R = 30$ and $L = 1$
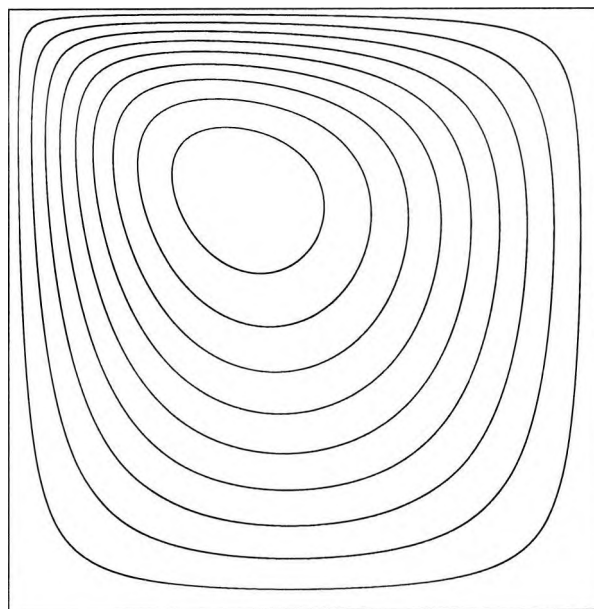
Figure 3.7: Streamlines from the numerical calculation for $R = 30$ and $L = 1$
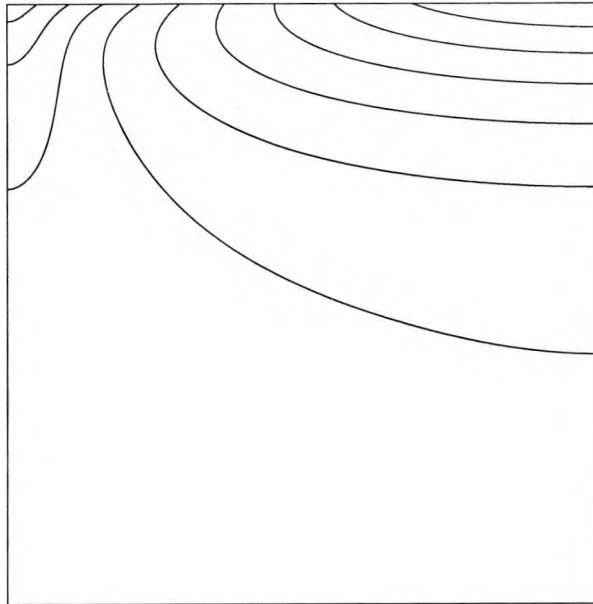
Figure 3.8: Isotherms from the numerical calculation for $R = 200$ and $L = 1$
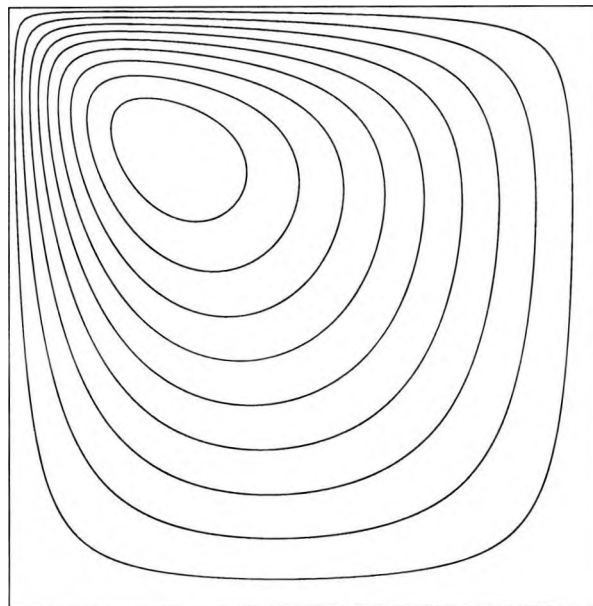
Figure 3.9: Streamlines from the numerical calculation for $R = 200$ and $L = 1$
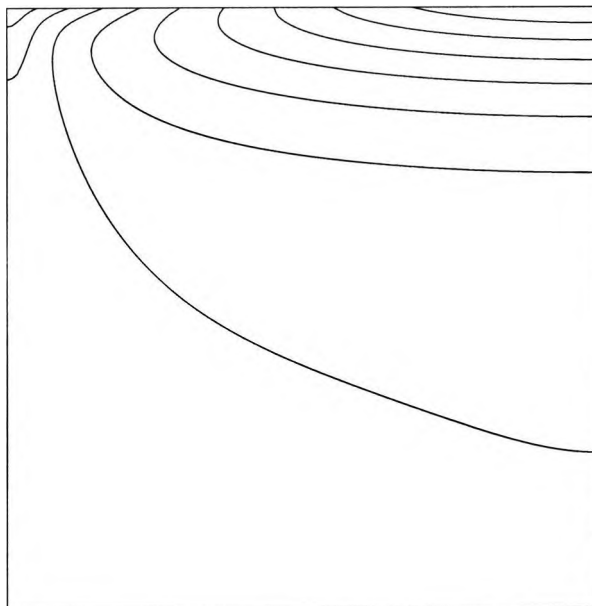
Figure 3.10: Isotherms from the numerical calculation for $R = 500$ and $L = 1$
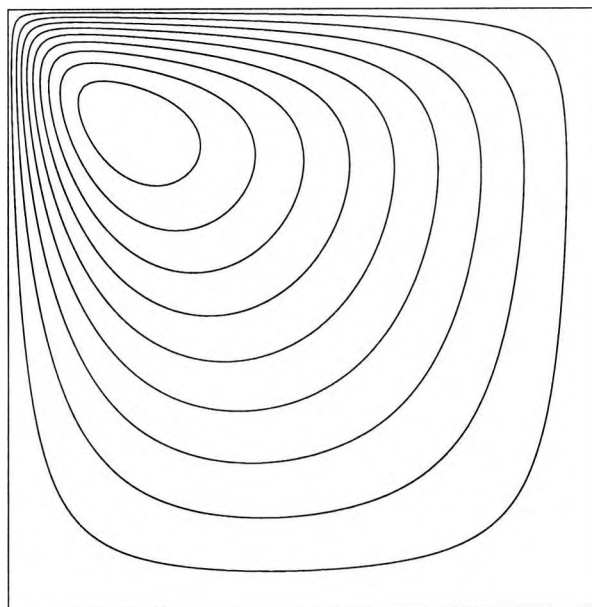
Figure 3.11: Streamlines from the numerical calculation for $R = 500$ and $L = 1$
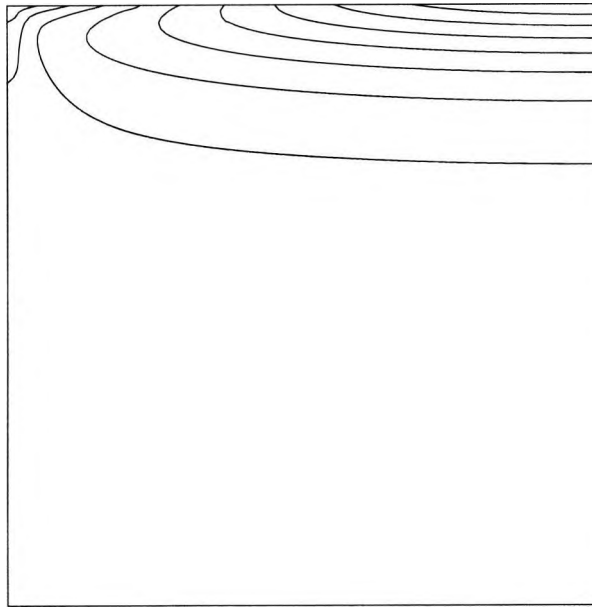
Figure 3.12: Isotherms from the numerical calculation for $R = 1500$ and $L = 1$
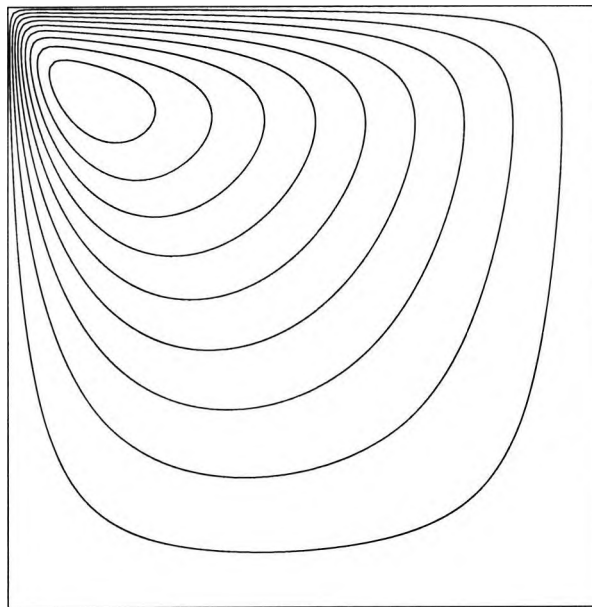
Figure 3.13: Streamlines from the numerical calculation for $R = 1500$ and $L = 1$
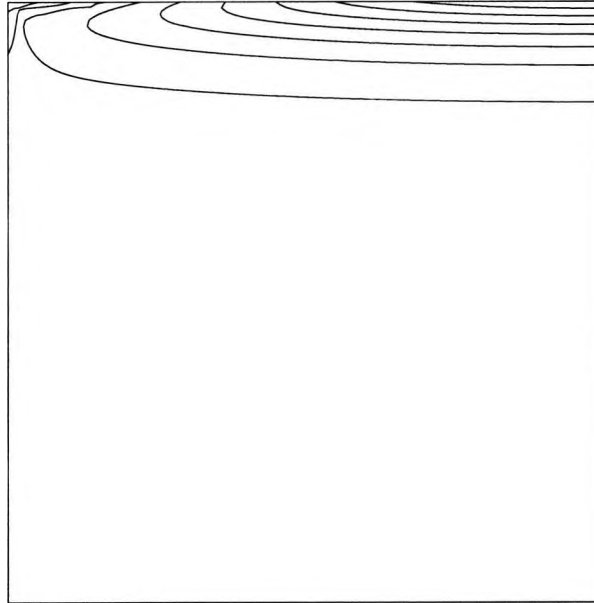
Figure 3.14: Isotherms from the numerical calculation for $R = 5000$ and $L = 1$
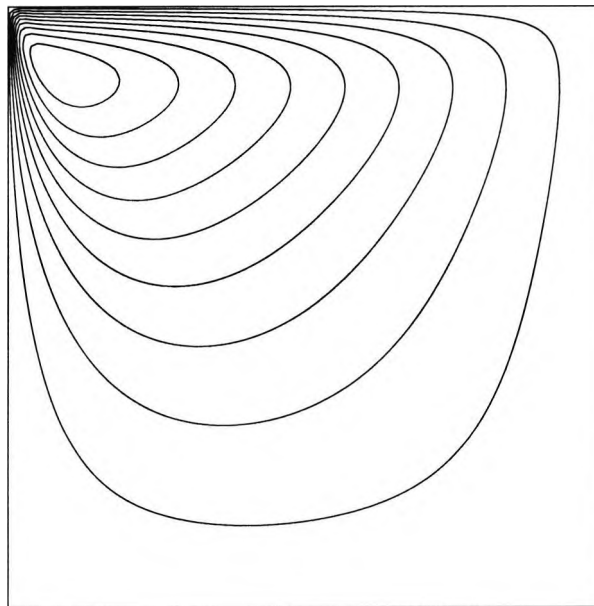
Figure 3.15: Streamlines from the numerical calculation for $R = 5000$ and $L = 1$
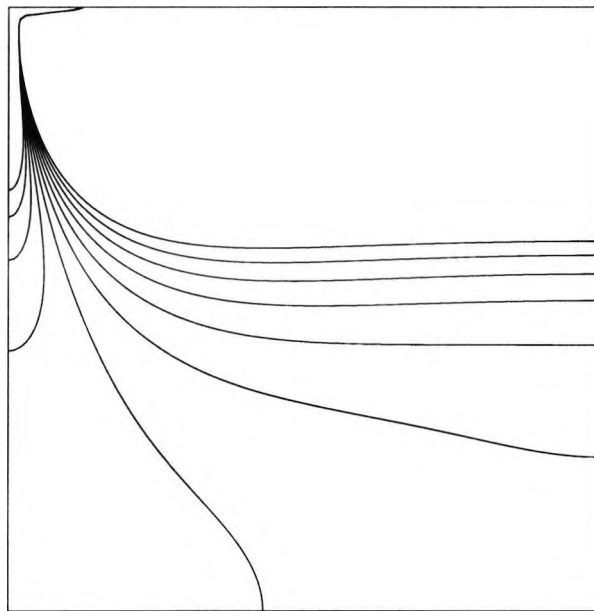
Figure 3.16: Isotherms between 0.23 and 0.24 from the numerical calculation for $R = 5000$ and $L = 1$
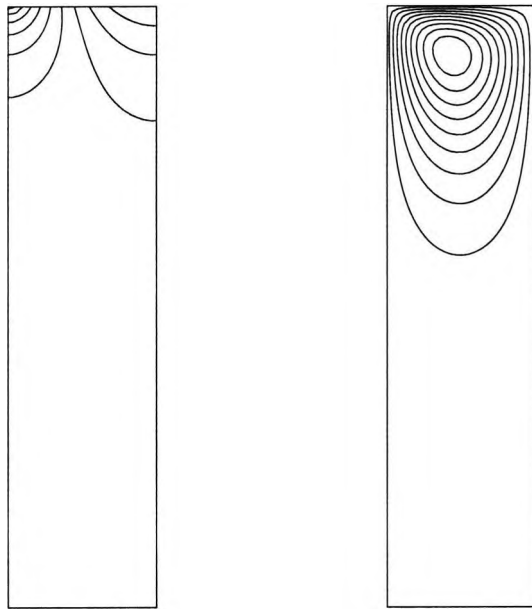
Figure 3.17: Isotherms and streamlines from the numerical calculation for $R = 5$ and $L = 0.25$
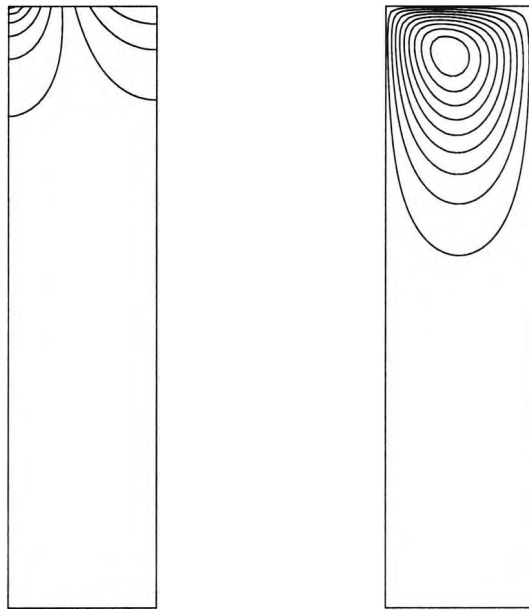
Figure 3.18: Isotherms and streamlines from the numerical calculation for $R = 30$ and $L = 0.25$
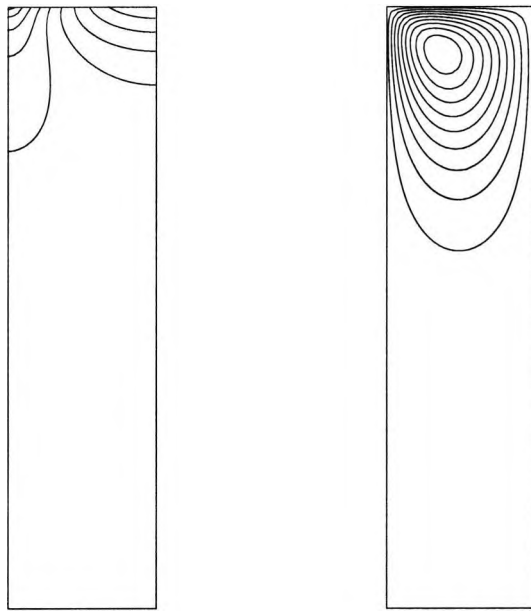
Figure 3.19: Isotherms and streamlines from the numerical calculation for $R =$ 200 and $L = 0.25$
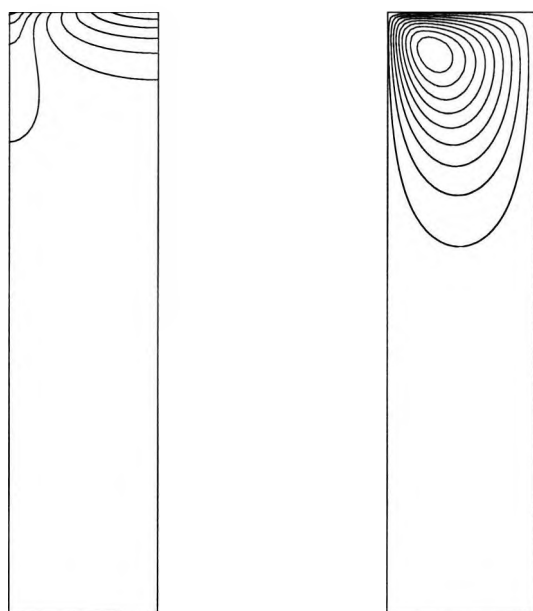
Figure 3.20: Isotherms and streamlines from the numerical calculation for $R = 500$ and $L = 0.25$
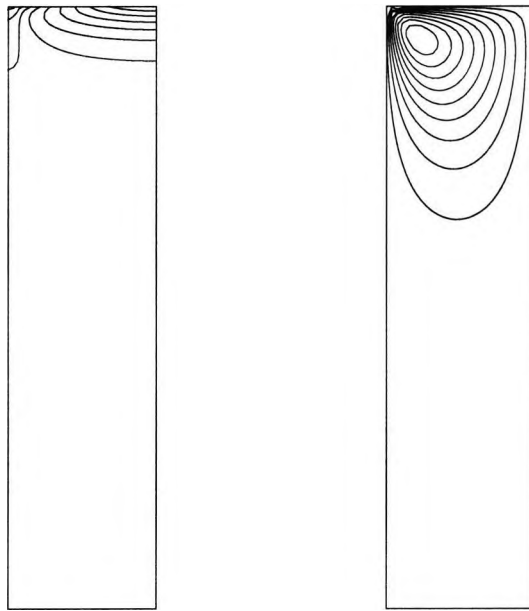
Figure 3.21: Isotherms and streamlines from the numerical calculation for $R = 1500$ and $L = 0.25$
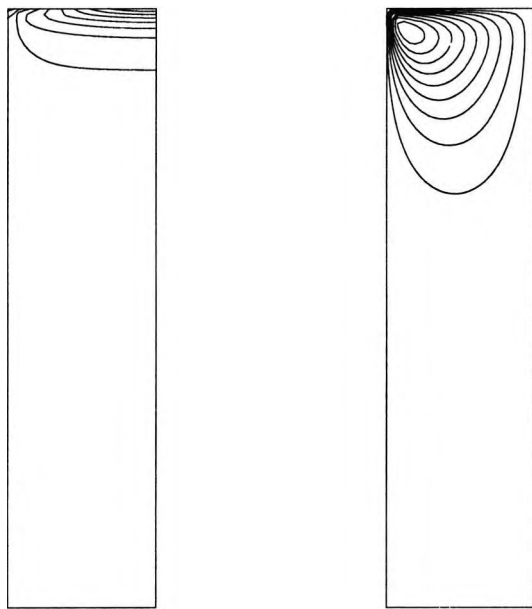
Figure 3.22: Isotherms and streamlines from the numerical calculation for $R = 5000$ and $L = 0.25$
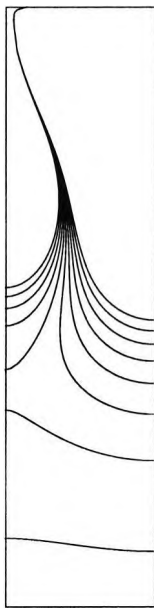
Figure 3.23: Isotherms between 0.2786 and 0.2787 for $R = 5000$ and $L = 0.25$
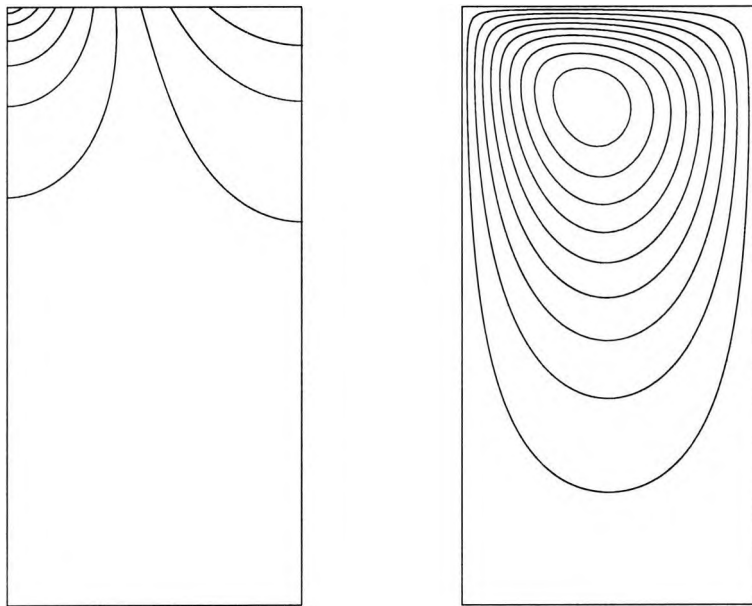
Figure 3.24: Isotherms and streamlines from the numerical calculation for $R = 5$ and $L = 0.5$
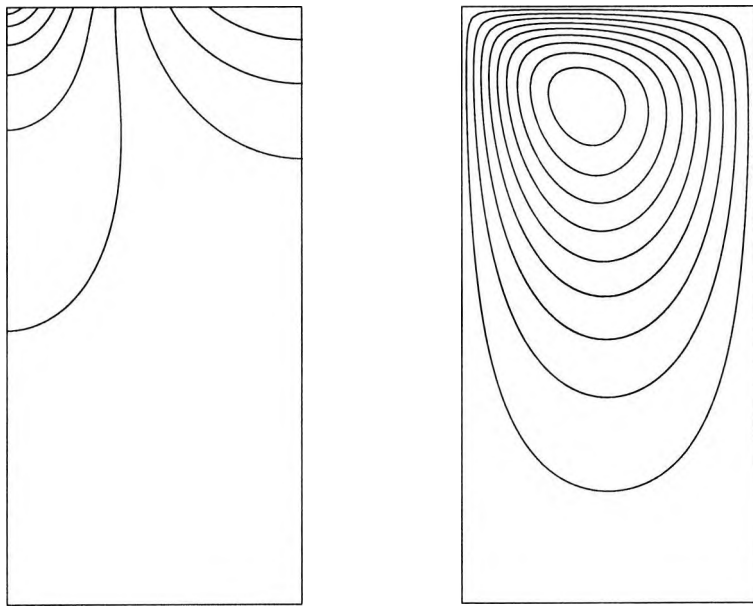
Figure 3.25: Isotherms and streamlines from the numerical calculation for $R = 30$ and $L = 0.5$
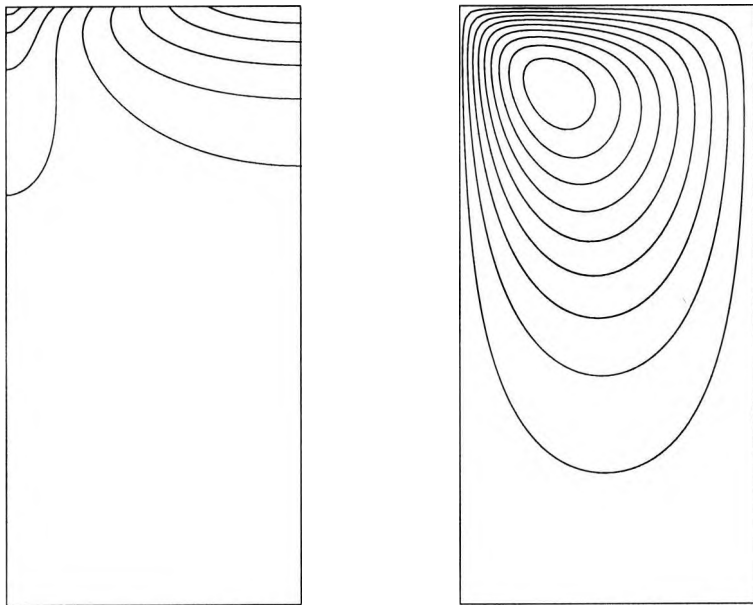
Figure 3.26: Isotherms and streamlines from the numerical calculation for $R = 200$ and $L = 0.5$
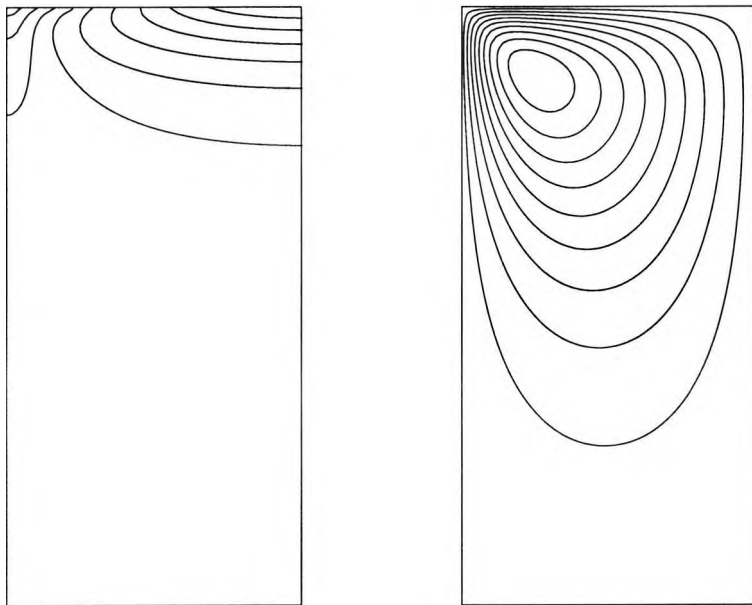
Figure 3.27: Isotherms and streamlines from the numerical calculation for $R = 500$ and $L = 0.5$
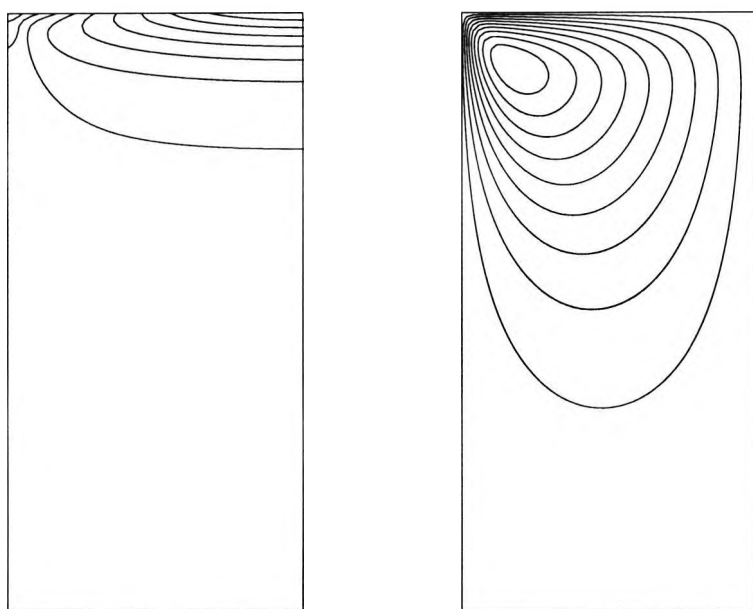
Figure 3.28: Isotherms and streamlines from the numerical calculation for $R = 1500$ and $L = 0.5$
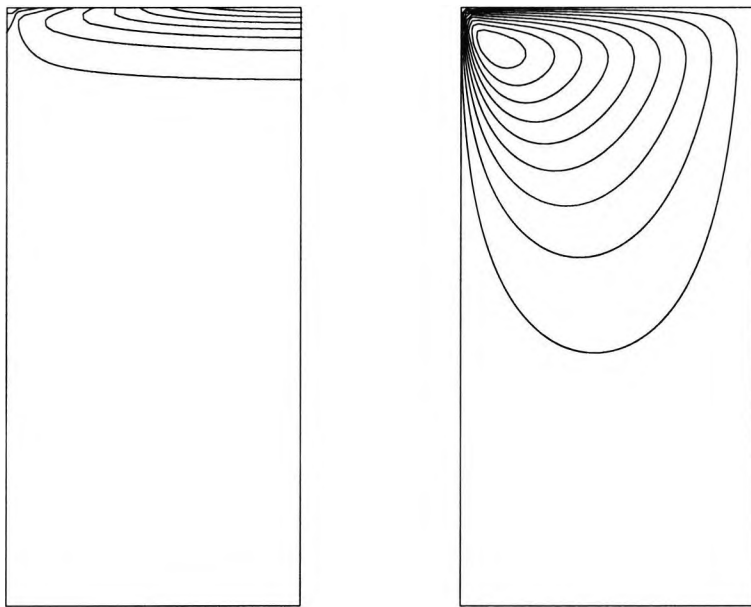
Figure 3.29: Isotherms and streamlines from the numerical calculation for $R = 5000$ and $L = 0.5$
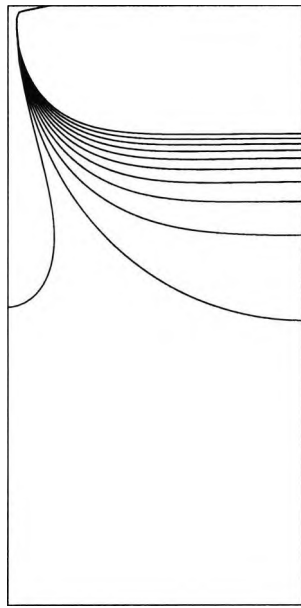
Figure 3.30: Isotherms between 0.25 and 0.26 for $R = 5000$ and $L = 0.5$
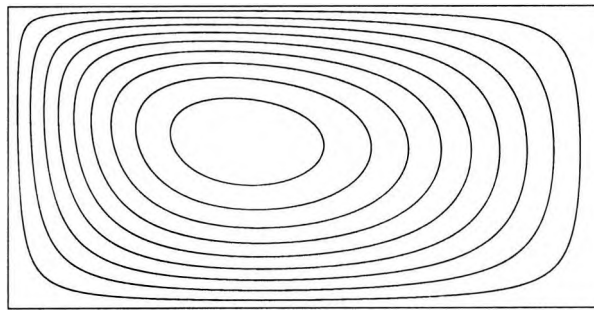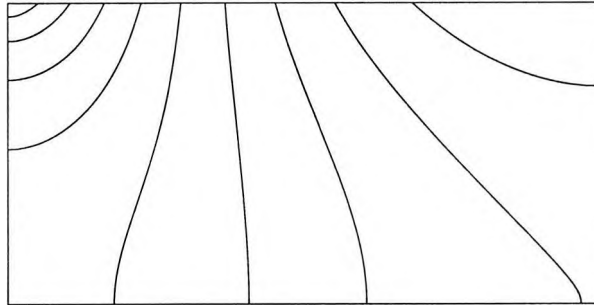
Figure 3.31: Isotherms and streamlines from the numerical calculation for $R = 5$ and $L = 2$
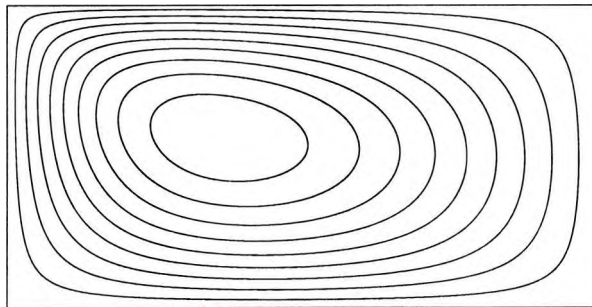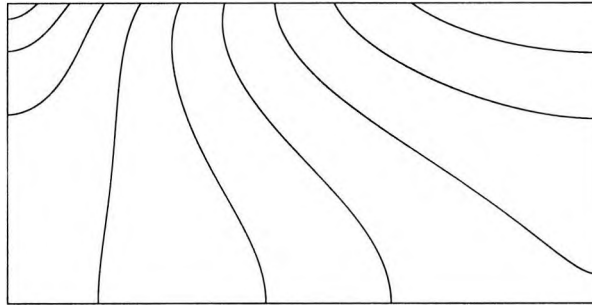
Figure 3.32: Isotherms and streamlines from the numerical calculation for $R = 30$ and $L = 2$
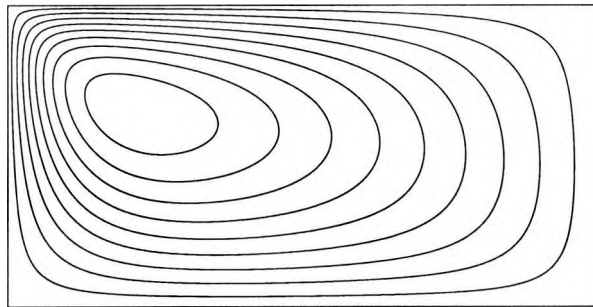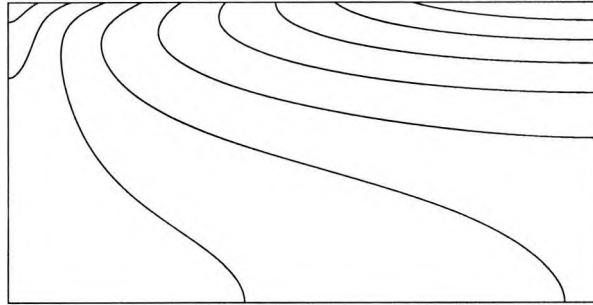
Figure 3.33: Isotherms and streamlines from the numerical calculation for $R = 200$ and $L = 2$
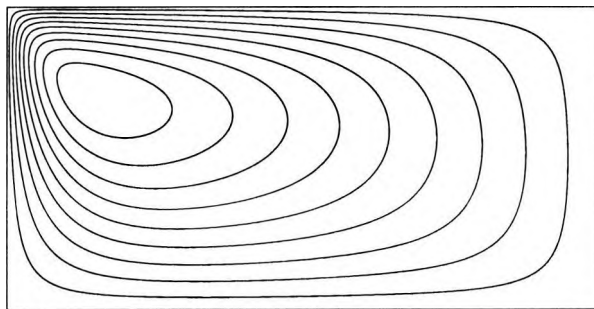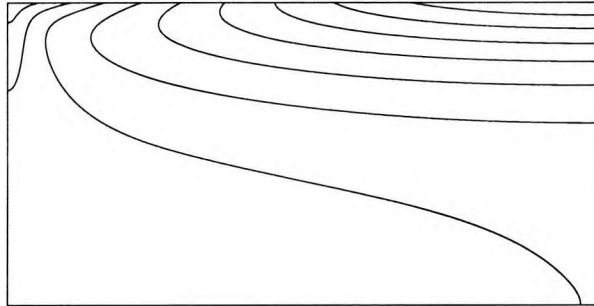
Figure 3.34: Isotherms and streamlines from the numerical calculation for $R = 500$ and $L = 2$
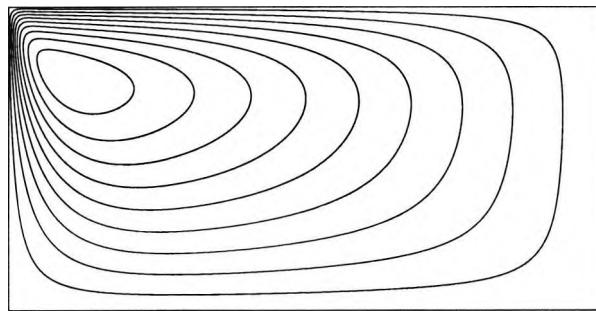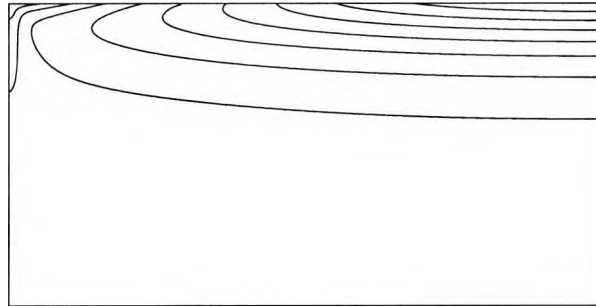
Figure 3.35: Isotherms and streamlines from the numerical calculation for $R = 1500$ and $L = 2$
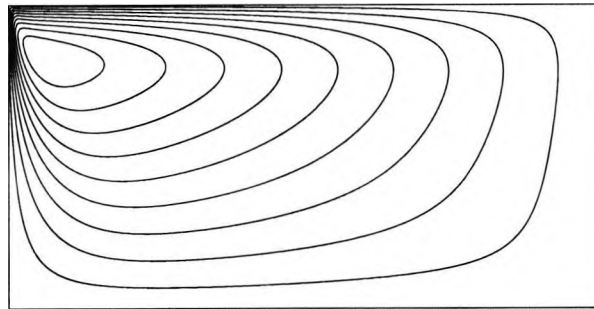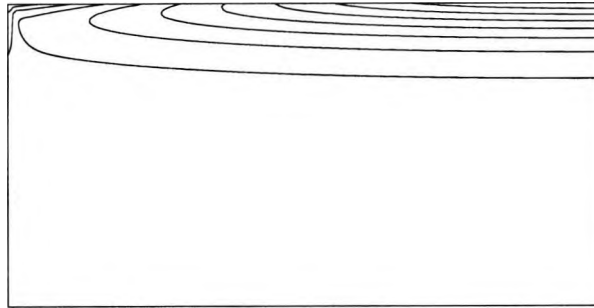
Figure 3.36: Isotherms and streamlines from the numerical calculation for $R = 5000$ and $L = 2$
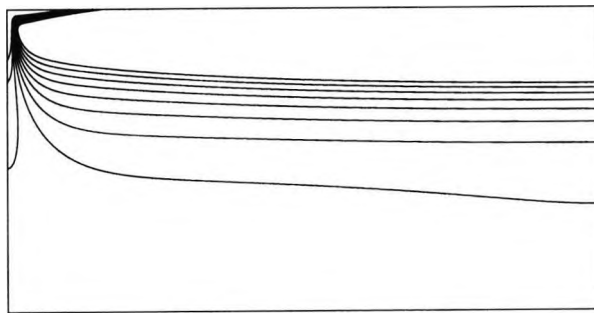
Figure 3.37: Isotherms between 0.2 and 0.3 from the numerical calculation for $R = 5000$ and $L = 2$
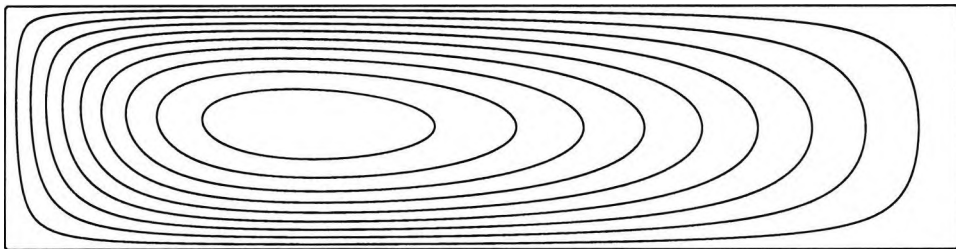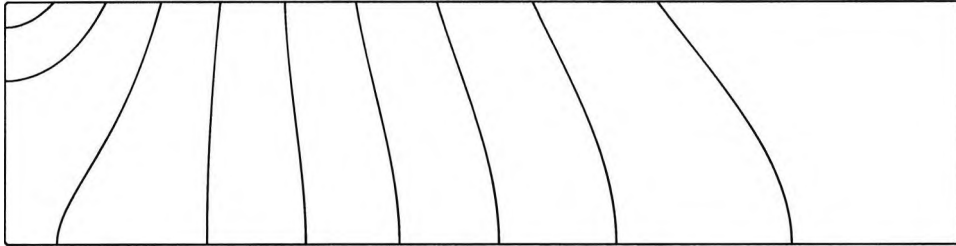
Figure 3.38: Isotherms and streamlines from the numerical calculation for $R = 5$ and $L = 4$
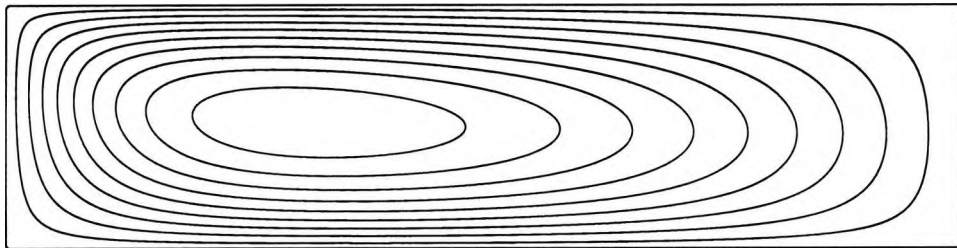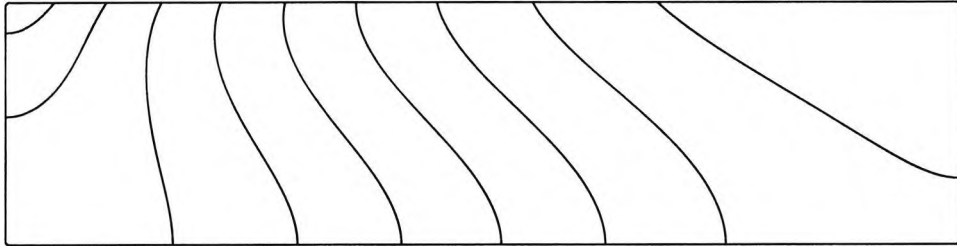
Figure 3.39: Isotherms and streamlines from the numerical calculation for $R = 30$ and $L = 4$
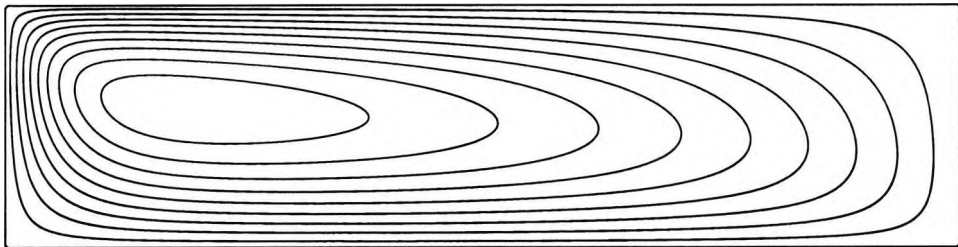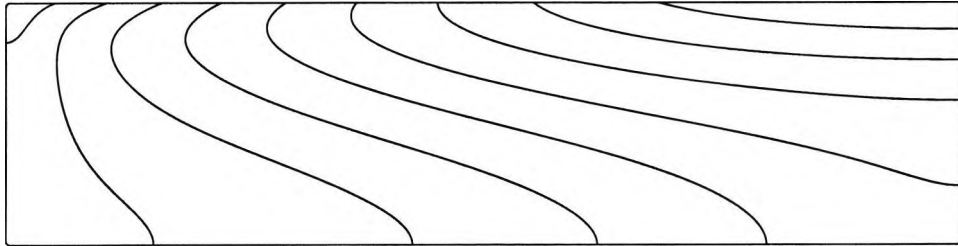
Figure 3.40: Isotherms and streamlines from the numerical calculation for $R = 200$ and $L = 4$
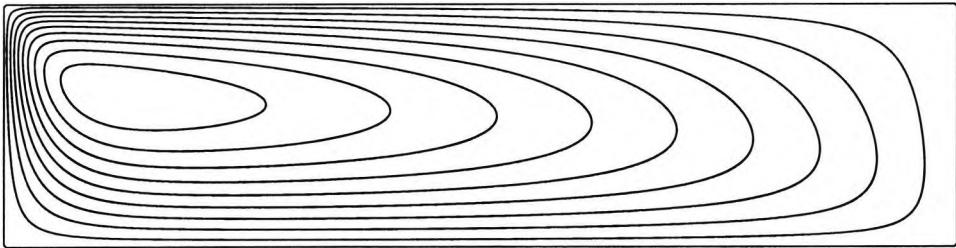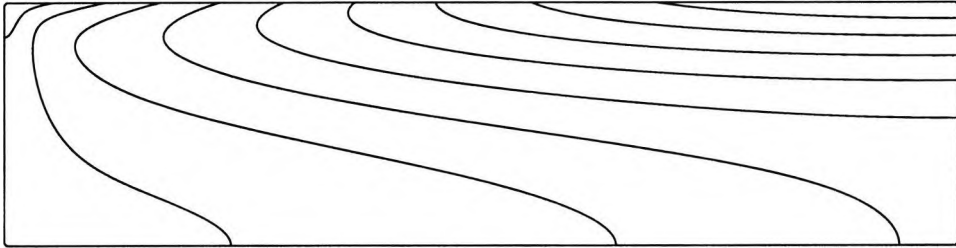
Figure 3.41: Isotherms and streamlines from the numerical calculation for $R = 500$ and $L = 4$
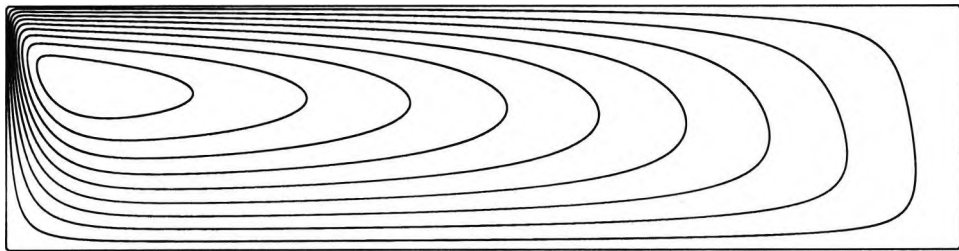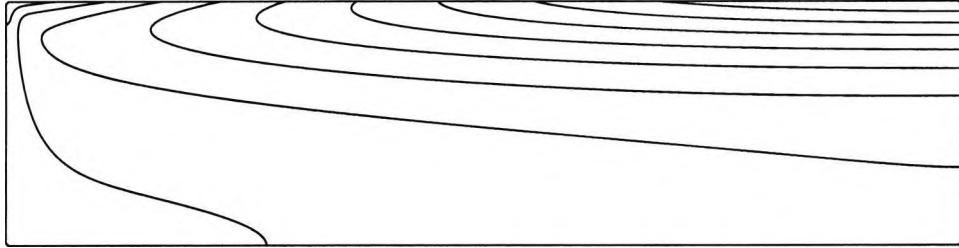
Figure 3.42: Isotherms and streamlines from the numerical calculation for $R = 1500$ and $L = 4$
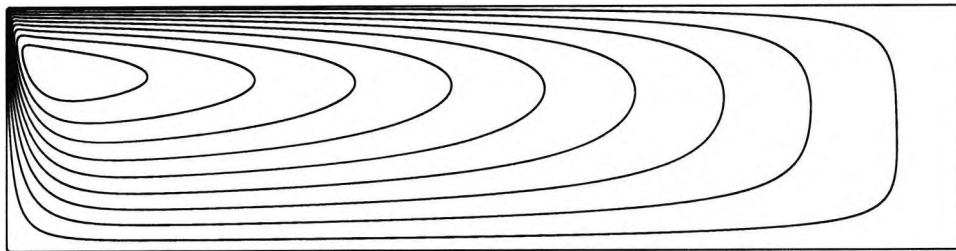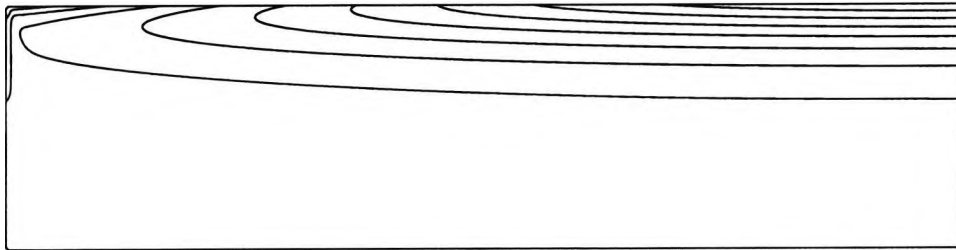
Figure 3.43: Isotherms and streamlines from the numerical calculation for $R = 5000$ and $L = 4$
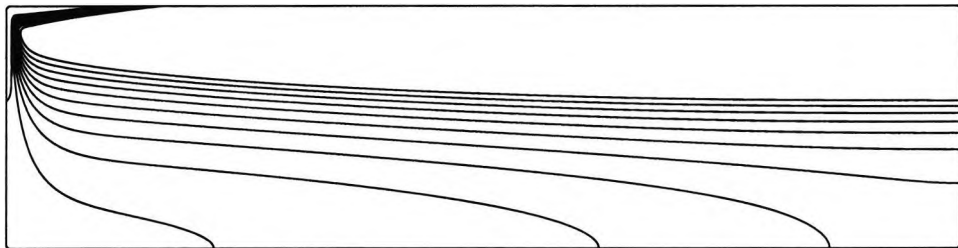
Figure 3.44: Isotherms between 0.2 and 0.3 from the numerical calculation for $R = 5000$ and $L = 4$

Chapter 4

An Approximate Theory for Large Darcy-Rayleigh Numbers

4.1 Introduction

Numerical calculations of the problems in Chapter 2 and Chapter 3 have shown that when R is large all the main features of the steady flow and temperature fields shift toward the upper boundary. In this chapter we obtain an approximate solution in the limit of large Darcy-Rayleigh number R by using an asymptotic method to investigate the flow in an upper horizontal boundary layer. By assuming that the temperature along the upper surface of the cavity is a quadratic function of x as in (3.1.1) a solution may be sought in which the temperature and stream function in the horizontal boundary layer depend on quadratic and linear functions of x respectively. In this way we can find an exact solution of the horizontal boundary layer equations as outlined in Section 4.2 below. Making use of this solution, the temperature in the cavity below the horizontal boundary layer can be obtained by considering the heat transfer in the horizontal boundary layer. This is undertaken in Section 4.3. Although we shall see that the results compare well, in some respects, with the full numerical calculations of Chapter 3, it emerges that the horizontal boundary layer solution discussed in this chapter can only be regarded as an approximate representation of the flow and temperature fields there. This is because the solution fails to take proper account of the flow near the cold end of the cavity. This is discussed further in Section 4.4.

4.2 Upper horizontal boundary layer approximation

We expect the main variation of the steady flow and temperature fields to be in a horizontal layer near $z = 1$. Assuming that $z = 1 - R^{-\alpha}\bar{z}$ near the upper boundary where $\bar{z} = O(1)$ and $\alpha > 0$ it follows that in the governing equations (3.1.2), (3.1.3), $\frac{\partial^2 \psi}{\partial z^2} >> \frac{\partial^2 \psi}{\partial x^2}$ and $\frac{\partial^2 T}{\partial z^2} >> \frac{\partial^2 T}{\partial x^2}$. Thus we try to balance

$$\frac{\psi}{z^2} \sim \frac{RT}{x}, \tag{4.2.1}$$

$$\frac{T}{z^2} \sim \frac{T\psi}{xz}. \tag{4.2.2}$$

Since $T \sim 1$ and $x \sim 1$ within the layer it follows from (4.2.1) that $\psi \sim Rz^2$ and then from (4.2.2)that $z^{-2} \sim Rz$ in which case $z \sim R^{-\frac{1}{3}}$ and $\psi \sim R^{\frac{1}{3}}$. Thus we set $\alpha = \frac{1}{3}$ (see figure 4.1) and the upper horizontal layer solution is constructed in the form

$$T(x, z) = \bar{T}(x, \bar{z}) + \cdots, \tag{4.2.3}$$

$$\psi(x, z) = R^{\frac{1}{3}}\bar{\psi}(x, \bar{z}) + \cdots, \tag{4.2.4}$$

where

$$z = 1 - R^{-\frac{1}{3}}\bar{z}. \tag{4.2.5}$$

Then $\bar{T}$ and $\bar{\psi}$ satisfy the horizontal boundary layer equations

$$\frac{\partial^2 \bar{T}}{\partial \bar{z}^2} = -\frac{\partial \bar{\psi}}{\partial \bar{z}}\frac{\partial \bar{T}}{\partial x} + \frac{\partial \bar{\psi}}{\partial x}\frac{\partial \bar{T}}{\partial \bar{z}}, \tag{4.2.6}$$

$$\frac{\partial^2 \bar{\psi}}{\partial \bar{z}^2} = -\frac{\partial \bar{T}}{\partial x}, \tag{4.2.7}$$

with boundary conditions

$$\bar{\psi} = 0, \quad \bar{T} = 1 - L^{-2}(x - L)^2, \quad \bar{z} = 0. \tag{4.2.8}$$

The actual boundary conditions as $\bar{z} \to \infty$ will emerge later, but we consider here what happens if we assume that

$$\frac{\partial \bar{\psi}}{\partial \bar{z}} \to 0, \quad \frac{\partial \bar{T}}{\partial \bar{z}} \to 0, \quad \bar{z} \to \infty. \tag{4.2.9}$$

100

We look for a solution of (4.2.6)-(4.2.9) in the form

$$\bar{\psi} = (L-x)\bar{\phi}_0(\bar{z}), \tag{4.2.10}$$

$$\bar{T} = -(L-x)^2\bar{\theta}_0(\bar{z}) + \bar{\theta}_1(\bar{z}). \tag{4.2.11}$$

Note that these solutions are consistent with the end conditions $\bar{\psi} = \frac{\partial \bar{T}}{\partial x} = 0$ at $x = L$ but do not satisfy the equivalent boundary conditions at $x = 0$. The existence of a vertical boundary layer near $x = 0$ is discussed in Section 4.4. Substitution in (4.2.6) and (4.2.7) gives

$$\bar{\theta}_1'' - \bar{\theta}_0''(L-x)^2 = -2(L-x)^2\bar{\phi}_0'\bar{\theta}_0 - \bar{\phi}_0(\bar{\theta}_1' - (L-x)^2\bar{\theta}_0'), \tag{4.2.12}$$

$$(L-x)\bar{\phi}_0'' = -2(L-x)\bar{\theta}_0, \tag{4.2.13}$$

from which it follows that the functions $\bar{\phi}_0$, $\bar{\theta}_0$ and $\bar{\theta}_1$ satisfy the nonlinear ordinary differential equations

$$\bar{\phi}_0'' = -2\bar{\theta}_0, \tag{4.2.14}$$

$$\bar{\theta}_0'' - 2\bar{\phi}_0'\bar{\theta}_0 + \bar{\phi}_0\bar{\theta}_0' = 0, \tag{4.2.15}$$

$$\bar{\theta}_1'' = -\bar{\phi}_0\bar{\theta}_1', \tag{4.2.16}$$

to be solved subject to the boundary conditions

$$\bar{\theta}_0 = L^{-2}, \quad \bar{\theta}_1 = 1, \quad \bar{\phi}_0 = 0 \quad (\bar{z} = 0), \tag{4.2.17}$$

$$\bar{\phi}_0', \quad \bar{\theta}_0', \quad \bar{\theta}_1' \to 0 \quad (\bar{z} \to \infty). \tag{4.2.18}$$

We can scale out L from the system (4.2.14)-(4.2.18) by setting

$$\bar{z} = L^{\frac{2}{3}}Z, \quad \bar{\phi}_0 = L^{-\frac{2}{3}}\phi(Z), \quad \bar{\theta}_0 = L^{-2}\theta_0(Z), \quad \bar{\theta}_1 = \theta_1(Z) \tag{4.2.19}$$

to obtain

$$\phi'' = -2\theta_0, \tag{4.2.20}$$

$$\theta_0'' - 2\phi'\theta_0 + \phi\theta_0' = 0, \tag{4.2.21}$$

$$\theta_1'' = -\phi\theta_1', \tag{4.2.22}$$

101

with boundary conditions

$$\theta_0 = 1, \quad \theta_1 = 1, \quad \phi = 0 \quad (Z = 0), \tag{4.2.23}$$

$$\phi', \quad \theta_0', \quad \theta_1' \to 0 \quad (Z \to \infty). \tag{4.2.24}$$

From (4.2.20) we have $\theta_0 = -\frac{1}{2}\phi''$ so (4.2.21) can be transformed to give the following fourth order system for ϕ :

$$\phi^{iv} + \phi\phi''' - 2\phi'\phi'' = 0, \tag{4.2.25}$$

$$\phi = 0, \quad \phi'' = -2 \quad (Z = 0), \tag{4.2.26}$$

$$\phi' \to 0 \quad (Z \to \infty). \tag{4.2.27}$$

The outer boundary condition rules out the behaviour $\phi \sim kZ \quad (Z \to \infty)$ and it follows from one integration of (4.2.25) that

$$\phi''' + \phi\phi'' - \frac{3}{2}\phi'^2 = 0, \tag{4.2.28}$$

$$\phi = 0, \quad \phi'' = -2 \quad (Z = 0), \tag{4.2.29}$$

$$\phi' \to 0 \quad (Z \to \infty). \tag{4.2.30}$$

At the edge of the layer ϕ has the behaviour

$$\phi \sim a - ke^{-aZ} \quad (Z \to \infty), \tag{4.2.31}$$

where a and k are constants to be determined. These are effectively fixed by satisfying the two boundary conditions at $Z = 0$. If the solution (4.2.31) were valid for all Z then it would follow that

$$k = a = 2^{\frac{1}{3}} \tag{4.2.32}$$

and the actual solution of (4.2.28)-(4.2.30) was found by using this as an initial guess in an iterative scheme, as follows.

Equation (4.2.28) was converted into a set of first order ordinary differential equations which were then integrated inwards from a suitable outer boundary $Z = Z_\infty$ using a fourth order Runge Kutta scheme. At $Z = Z_\infty$ (4.2.31) was assumed to apply, the values of k and a being set initially to those given by

(4.2.32). This results in values of ϕ and ϕ'' at $Z = 0$ which can be considered functions of a and k. Setting

$$\phi(0) \equiv p(a, k), \tag{4.2.33}$$

$$\phi''(0) + 2 \equiv q(a, k), \tag{4.2.34}$$

we then use Newton's method to solve the system of nonlinear equations

$$p(a, k) = 0, \tag{4.2.35}$$

$$q(a, k) = 0. \tag{4.2.36}$$

To find new approximations to a and k the functions p and q are expanded as Taylor series about the point (a, k), leading to the Newton equations

$$0 = p(a, k) + \frac{\partial p}{\partial a}(a, k)\delta a + \frac{\partial p}{\partial k}(a, k)\delta k, \tag{4.2.37}$$

$$0 = q(a, k) + \frac{\partial q}{\partial a}(a, k)\delta a + \frac{\partial q}{\partial k}(a, k)\delta k. \tag{4.2.38}$$

The four partial derivatives are calculated numerically by repeating the Runge-Kutta solution for neighbouring values of a and k. From the above equations we then solve for the increments $\delta a, \delta k$ to obtain the new approximations $a + \delta a$ and $k + \delta k$. The whole procedure is then repeated until the conditions (4.2.35),(4.2.36) at $Z = 0$ are satisfied. The computations were carried out with $Z_\infty = 8$ and steps of $\triangle Z = 0.01$ in the Runge-Kutta scheme. Checks were made with other outer boundaries and step sizes to confirm the accuracy of the solution. The constants a and k converged to the final values

$$a = 1.141, \quad k = 1.021 \tag{4.2.39}$$

and the first derivative of ϕ at the origin was found to be given by

$$c = \phi'(0) = 1.447. \tag{4.2.40}$$

The graph of ϕ is shown in figure 4.2.

Once $\phi(Z)$ is determined then θ_0 is found from $\theta_0 = -\frac{1}{2}\phi''$ and is shown in figure 4.3 ; note that $\theta_0 \to 0$ as $Z \to \infty$. Also θ'_1 is found by integrating (4.2.22)

103

once to give

$$\theta_1' = -Ae^{-\int_0^Z \phi dZ} \tag{4.2.41}$$

where A is an arbitrary constant. One further integration then gives

$$\theta_1 = 1 - A\Theta_1 \tag{4.2.42}$$

where

$$\Theta_1 = \int_0^Z exp\left(-\int_0^Z \phi dZ\right) dZ \tag{4.2.43}$$

and is shown in figure 4.4. We see that

$$\theta_1 \to 1 - A\chi_0 \quad \text{as} \quad Z \to \infty, \tag{4.2.44}$$

where

$$\chi_0 = \int_0^\infty exp\left(-\int_0^Z \phi dZ\right) dZ = 1.472. \tag{4.2.45}$$

4.3 Heat transfer in the horizontal boundary layer

In order to find the constant A and thus complete the horizontal boundary layer solution we appeal to the fact that the solution must be consistent with the heat flux property of the overall solution in the cavity,

$$\int_0^L \frac{\partial T}{\partial z}(x, 1) dx = 0. \tag{4.3.1}$$

This can readily be established from (3.1.3)-(3.1.6) and expresses the fact that since no heat can escape through the sides or base of the cavity, the net heat transfer through the upper surface must vanish. The main contribution to this transfer in the limit of large R must come from the horizontal boundary layer and so it follows that

$$\int_0^L \frac{\partial \bar{T}}{\partial \bar{z}}(x, 0) dx = 0, \tag{4.3.2}$$

which gives

$$\int_0^L \left(\bar{\theta}_1'(0) - (L - x)^2 \bar{\theta}_0'(0)\right) dx = 0. \tag{4.3.3}$$

In terms of the scaled variables defined by (4.2.19), this implies that

$$\theta_1'(0) - \frac{1}{3}\theta_0'(0) = 0. \qquad (4.3.4)$$

Now

$$\theta_1'(0) = -A \qquad (4.3.5)$$

and

$$\theta_0'(0) = -\frac{1}{2}\phi'''(0) = -\frac{3}{4}(\phi'(0))^2 = -\frac{3}{4}c^2 \qquad (4.3.6)$$

from (4.2.28) so that

$$A = \frac{1}{4}c^2 = 0.524. \qquad (4.3.7)$$

This completes the solution (4.2.42) for θ_1, which is shown in figure 4.5. It is seen that

$$\theta_1 \to b = 1 - \frac{1}{4}c^2\chi_0 = 0.229 \quad \text{as} \quad Z \to \infty. \qquad (4.3.8)$$

This predicts a temperature in the cavity below the horizontal layer which is constant and given by

$$T(x,z) \approx b = 0.229. \qquad (4.3.9)$$

This is in reasonable agreement with the numerical results described in Chapter 3 and suggests that in the large Darcy-Rayleigh number limit the temperature throughout most of the cavity is somewhat greater than that of the coldest point on the upper surface.

The transport of heat through the horizontal boundary layer can be analysed as follows. From the horizontal boundary layer equation (4.2.6) it follows that the local heat transfer at the upper surface of the cavity is

$$-\frac{\partial \bar{T}}{\partial \bar{z}}(x,0) = \frac{\partial}{\partial x}\int_0^\infty \bar{\psi}\frac{\partial \bar{T}}{\partial \bar{z}}d\bar{z}. \qquad (4.3.10)$$

Integration over the length of the upper surface then gives

$$-\int_0^L \frac{\partial \bar{T}}{\partial \bar{z}}(\bar{z}=0)dx = \int_0^\infty \bar{\psi}\frac{\partial \bar{T}}{\partial \bar{z}}d\bar{z}\bigg|_{x=0}^{x=L} = -\int_0^\infty \bar{\psi}\frac{\partial \bar{T}}{\partial \bar{z}}d\bar{z}\bigg|_{x=0}, \qquad (4.3.11)$$

where it has been assumed that $\bar{\psi} = 0$ at $x = L$. This relates the total heat transfer through the upper wall to that passing through the left hand end of the horizontal layer. Since the total heat transfer through the upper wall is

105

zero (equation (4.3.2)) it follows from (4.3.11) that the horizontal boundary layer solution will also satisfy

$$\int_0^\infty \bar{\psi} \frac{\partial \bar{T}}{\partial \bar{z}}(x = 0)d\bar{z} = 0. \qquad (4.3.12)$$

The choice of $A = \frac{1}{4}c^2$ ensures that this is the case so that $\bar{\phi}_0, \quad \bar{\theta}_0 \quad$ and $\bar{\theta}_1$ are such that

$$\int_0^\infty L\bar{\phi}_0(\bar{z}) \left(\frac{d\bar{\theta}_1}{d\bar{z}} - L^2 \frac{d\bar{\theta}_0}{d\bar{z}} \right) d\bar{z} = 0. \qquad (4.3.13)$$

In terms of the scaled functions $\phi, \quad \theta_0$ and θ_1 this implies that

$$\int_0^\infty \phi(\theta_1' - \theta_0')dZ = 0. \qquad (4.3.14)$$

4.4 Summary

The overall temperature profile at the end $x = 0$ of the horizontal boundary layer is given by

$$\bar{T}(0, \bar{z}) = \theta_1(Z) - \theta_0(Z) \qquad (4.4.1)$$

and is shown in figure 4.6. This indicates that the temperature gets higher as we move down the left-hand edge of the horizontal boundary layer until a maximum value $\bar{T} \approx 0.313$ is reached at $\bar{z} = L^{\frac{2}{3}}Z_0 \approx 0.96L^{\frac{2}{3}}$. As we move down further the temperature gets lower until the asymptote $\bar{T} \approx 0.229$ is reached as $\bar{z} \to \infty$.

In the case of the stream function at $x = 0$,

$$\bar{\psi}(0, \bar{z}) = L^{\frac{1}{3}}\phi(Z), \qquad (4.4.2)$$

where ϕ is the function shown in figure 4.2. As we move down the left-hand edge of the horizontal layer, the stream function increases from zero and reaches a maximum value of $\bar{\psi} \approx 1.141L^{\frac{1}{3}}$ as $\bar{z} \to \infty$. The scaled velocity profile $U = \phi'$ is shown in figure 4.7 which indicates that the horizontal velocity in the negative x direction is highest at the upper boundary and reduces to zero at the bottom of the horizontal layer.

The overall temperature and stream function fields in the horizontal boundary layer can be expressed in the form

$$\bar{T} = \theta_1(Z) - (1 - X)^2\theta_0(Z), \quad \bar{\psi} = L^{\frac{1}{3}}(1 - X)\phi(Z), \qquad (4.4.3)$$

106

where $X = x/L$ and the corresponding isotherms and streamlines are shown in the domain $0 \leq X \leq 1, \quad Z \geq 0$ in figures 4.8 and 4.9. The isotherms are consistent with the formation of the thermal layer at the upper surface of the cavity, in accordance with the full cavity calculations in Chapter 2 and Chapter 3. The streamlines indicate a flow drawn into the lower edge of the horizontal layer and then conveyed to the cold end, where it is expelled from the layer. Here the comparison with the full numerical calculations is less convincing, both in terms of the implied existence of a region of predominantly upward velocity below the thermal variation in the layer(not seen in the numerical calculations) and the non-existence of a closed eddy at the end of the layer(seen in the numerical calculations). The exact solution of the horizontal boundary layer equations found here imposes both a horizontal velocity and a temperature profile at the end $x = 0$ of the layer which must be adjusted in order to achieve the boundary conditions $\psi = \frac{\partial T}{\partial x} = 0$ on the side wall of the cavity. Although it seems likely that a vertical boundary layer must exist at the end of the horizontal layer, and that this will allow variations in both ψ and T there, it is not clear that such a layer can accommodate the two outer behaviours (4.4.1) and (4.4.2) specified by the horizontal boundary layer solution. This question is considered in detail in the next chapter, where it will emerge that the horizontal layer solution obtained here must be modified in both a qualitative and quantitative sense. Nevertheless, the solution obtained in this chapter still provides a useful approximation to the behaviour of the flow and temperature fields near the upper surface of the cavity and in particular appears to predict a constant temperature in the core region below which is in close agreement with that of the full numerical calculations at large Darcy-Rayleigh numbers.
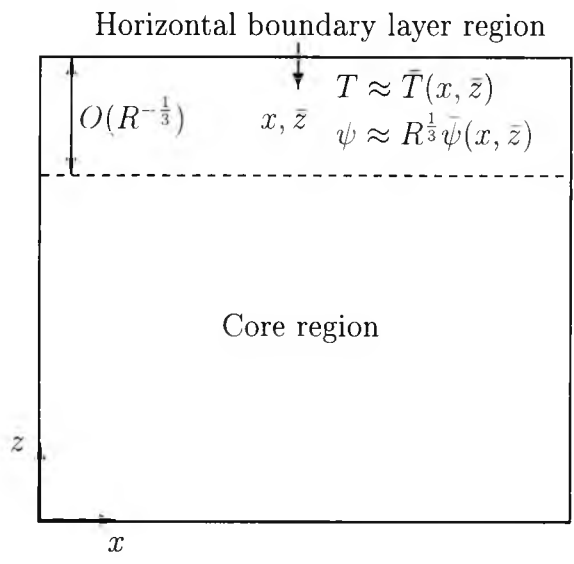
Figure 4.1: Horizontal boundary layer region
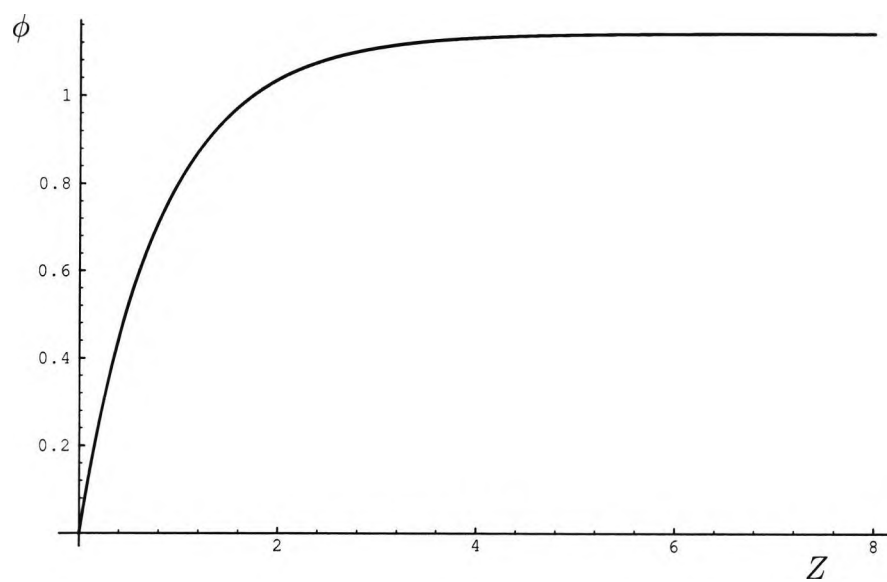
Figure 4.2: Graph of ϕ versus Z
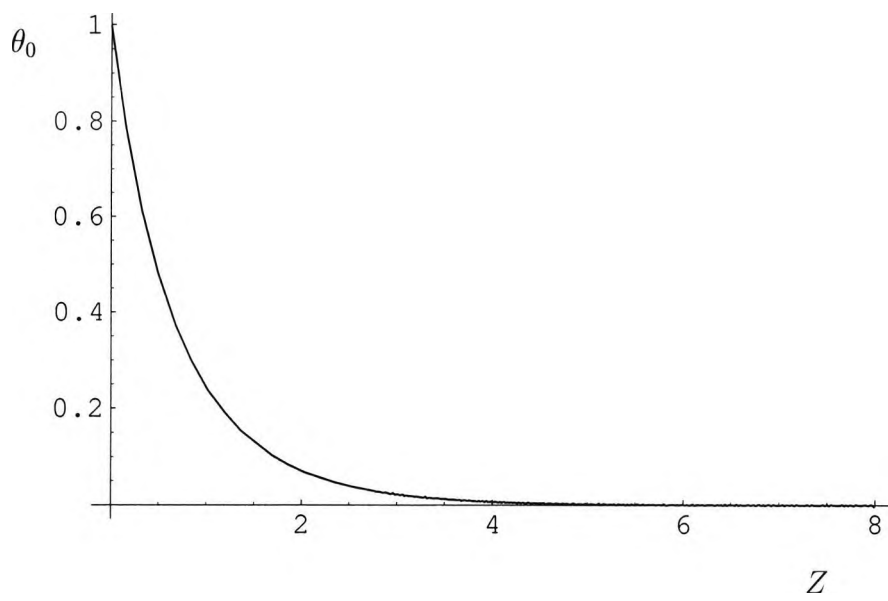
Figure 4.3: Graph of θ_0 versus Z
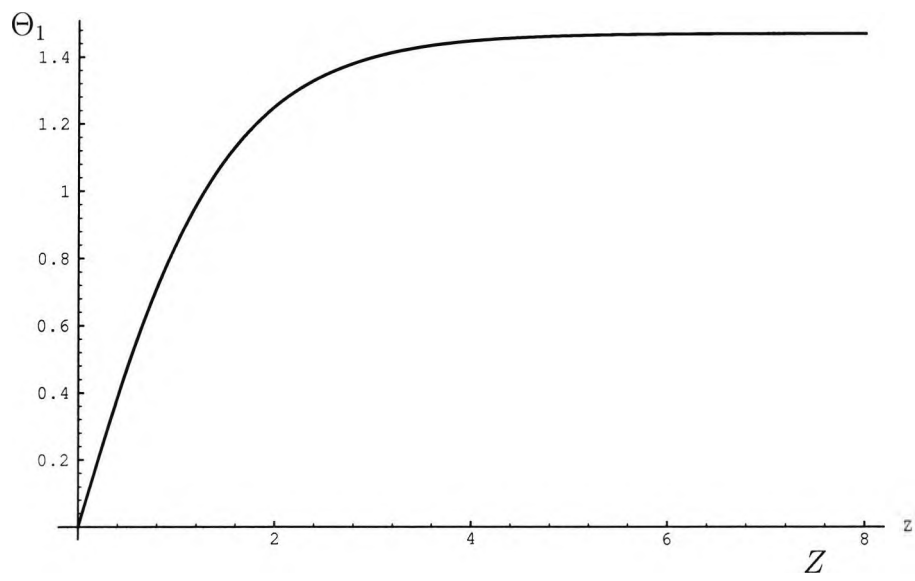
Figure 4.4: Graph of Θ_1 versus Z
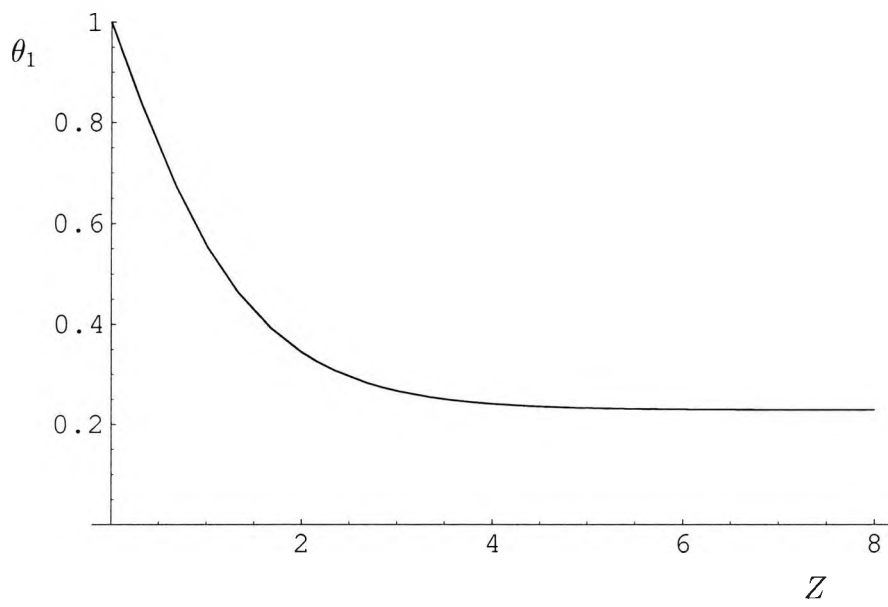
Figure 4.5: Graph of θ_1 versus Z
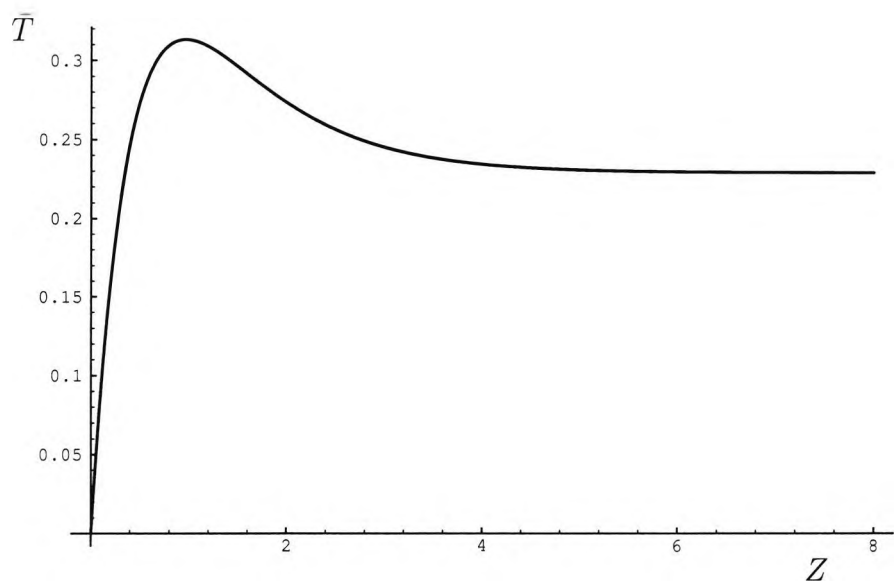
Figure 4.6: Graph of temperature $\bar{T} = \theta_1(Z) - \theta_0(Z)$ versus Z in the horizontal boundary layer at $x = 0$.
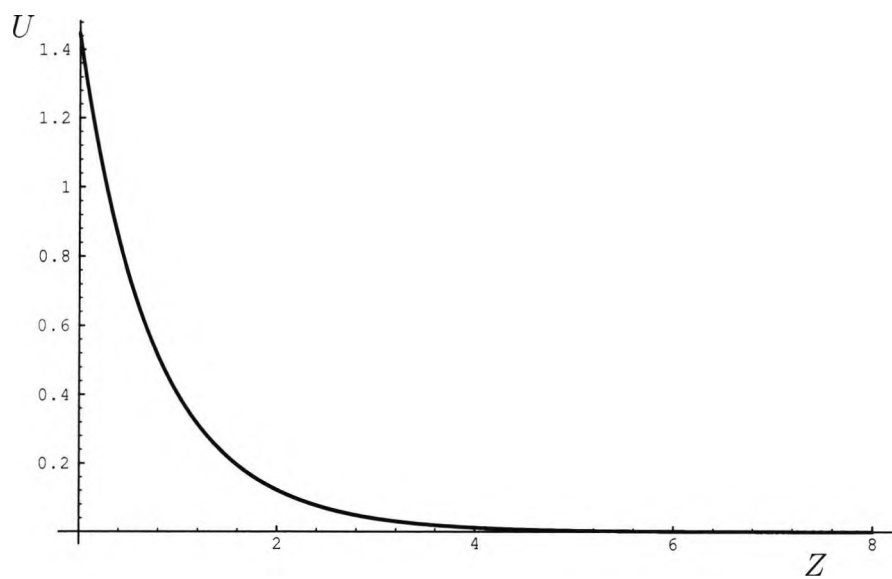
Figure 4.7: Graph of the scaled velocity profile $U = \phi'$ versus Z in the horizontal boundary layer at $x = 0$.
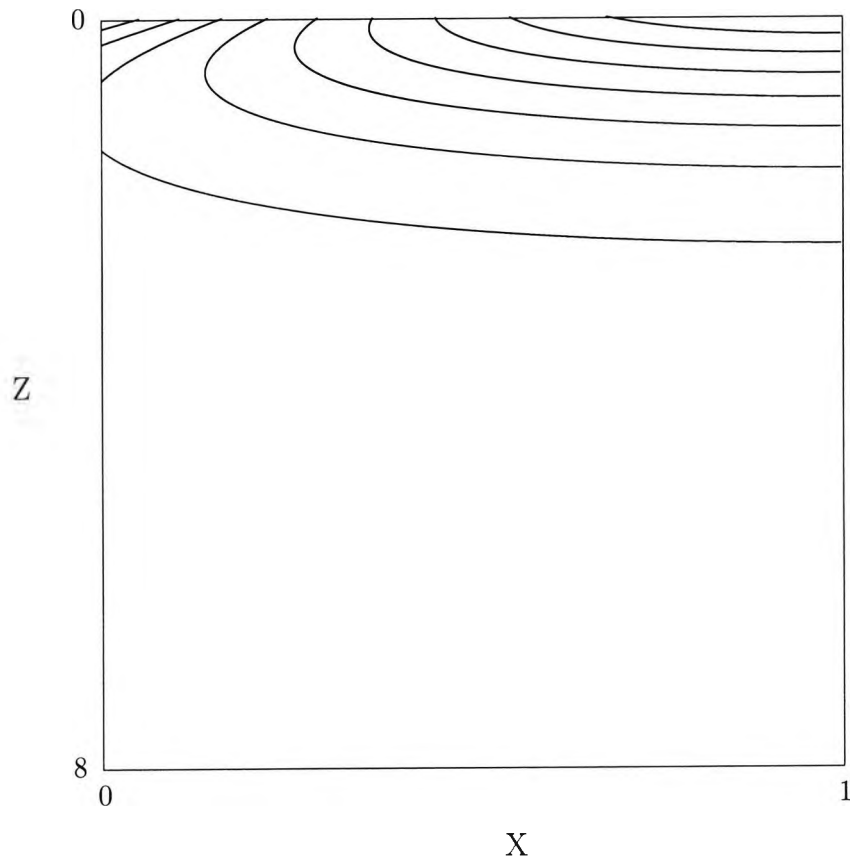
Figure 4.8: Isotherms of the temperature field in the horizontal boundary layer
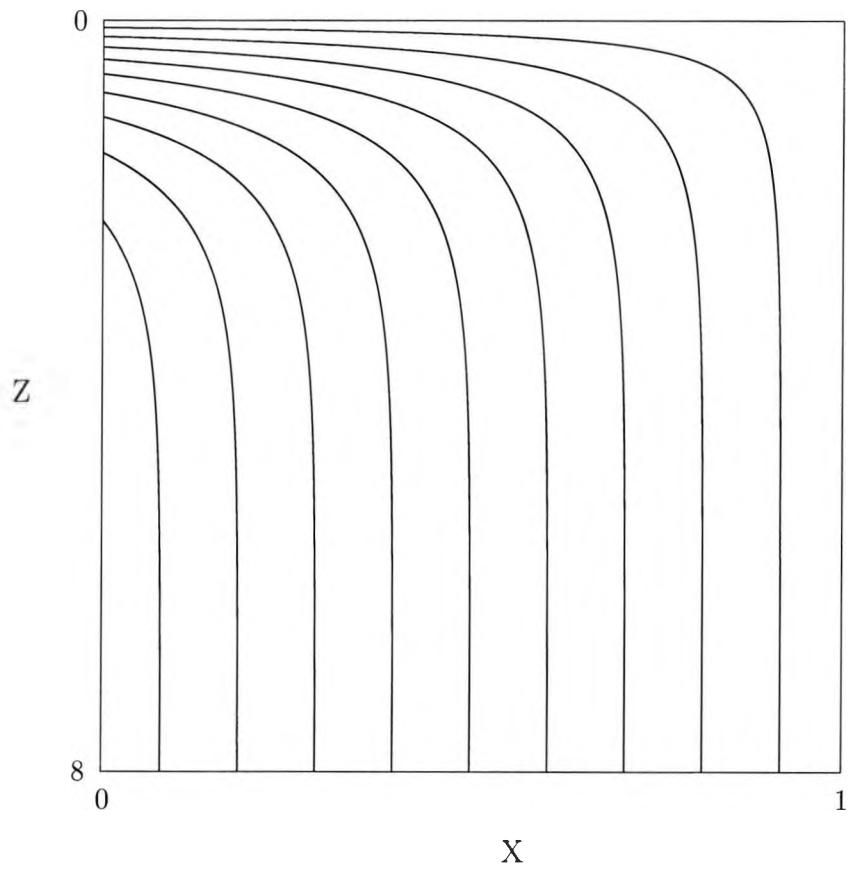
Figure 4.9: Contours of the stream function field in the horizontal boundary layer

Chapter 5

Vertical Boundary Layer

5.1   Introduction

In this chapter we consider the results of the horizontal boundary layer analysis of the previous chapter and investigate the implications of these results for the existence of a vertical boundary layer near the top of the wall, $x = 0$, in the limit of large Darcy-Rayleigh number. General properties of the vertical boundary layer equations are considered with a view to understanding whether they will admit a solution consistent with the profiles (4.4.1) and (4.4.2) at the end of the horizontal layer. The vertical boundary layer system is formulated in Section 5.2. Section 5.3 considers the behaviour of the solution at the outer edge of the layer, with particular reference to the profiles (4.4.1), (4.4.2). Various integral properties of the vertical boundary layer system are studied in Section 5.4 and in Section 5.5 an asymptotic solution is determined near the top of the layer, as $\bar{z} \to 0$. In Section 5.6 an integral method is used to shed further light on the properties of the solution for general $\bar{z}$ and in Section 5.7, asymptotic solutions are considered in the limit $\bar{z} \to \infty$. The results are summarized in Section 5.8.

5.2   Vertical boundary layer system

We consider the existence of a region near the top of the wall $x = 0$ in which the solution is generated by the incoming flow and temperature fields of the horizontal boundary layer. It follows that we must assume solutions for T and ψ which are order one and order $R^{\frac{1}{3}}$ respectively as $R \to \infty$, and that the vertical scale of

variation, also determined by the horizontal layer, is $\bar{z} = O(1)$, where

$$z = 1 - R^{-\frac{1}{3}}\bar{z}. \tag{5.2.1}$$

The terms in the heat equation

$$\frac{\partial^2 T}{\partial x^2} + \frac{\partial^2 T}{\partial z^2} = \frac{\partial T}{\partial x}\frac{\partial \psi}{\partial z} - \frac{\partial T}{\partial z}\frac{\partial \psi}{\partial x} \tag{5.2.2}$$

are then of order

$$\frac{1}{x^2}, R^{\frac{2}{3}} = \frac{R^{\frac{2}{3}}}{x}, \tag{5.2.3}$$

whilst the terms in the equation

$$\frac{\partial^2 \psi}{\partial x^2} + \frac{\partial^2 \psi}{\partial z^2} = -R\frac{\partial T}{\partial x} \tag{5.2.4}$$

are of order

$$\frac{R^{\frac{1}{3}}}{x^2}, R = \frac{R}{x}. \tag{5.2.5}$$

Since we must have $x \ll 1$ it follows that the only viable balance which allows T and ψ to vary in the horizontal direction is obtained by balancing the x derivative terms in the Laplace operators with the right-hand sides of (5.2.2) and (5.2.4), in which case $x \sim R^{-\frac{2}{3}}$ (see figure 5.1) and we set

$$x = R^{-\frac{2}{3}}\bar{x}. \tag{5.2.6}$$

The solutions for ψ and T are expanded in the form

$$\psi = R^{\frac{1}{3}}\tilde{\psi}(\bar{x}, \bar{z}) + \cdots, \tag{5.2.7}$$

$$T = \tilde{T}(\bar{x}, \bar{z}) + \cdots \tag{5.2.8}$$

and since the z derivatives in the Laplace operators may be neglected relative to the x derivatives we then obtain the vertical boundary layer equations

$$\frac{\partial^2 \tilde{\psi}}{\partial \bar{x}^2} = -\frac{\partial \tilde{T}}{\partial \bar{x}}, \tag{5.2.9}$$

$$\frac{\partial^2 \tilde{T}}{\partial \bar{x}^2} = -\frac{\partial \tilde{T}}{\partial \bar{x}}\frac{\partial \tilde{\psi}}{\partial \bar{z}} + \frac{\partial \tilde{T}}{\partial \bar{z}}\frac{\partial \tilde{\psi}}{\partial \bar{x}}, \tag{5.2.10}$$

118

with boundary conditions

$$\tilde{\psi} = \tilde{T} = 0, \quad \bar{z} = 0, \tag{5.2.11}$$

$$\tilde{\psi} = \frac{\partial \tilde{T}}{\partial \bar{x}} = 0, \quad \bar{x} = 0, \tag{5.2.12}$$

$$\tilde{\psi} \to \psi_\infty(\bar{z}), \quad \tilde{T} \to T_\infty(\bar{z}), \quad \bar{x} \to \infty, \tag{5.2.13}$$

where

$$\psi_\infty(\bar{z}) = \bar{\psi}(0, \bar{z}), \tag{5.2.14}$$

$$T_\infty(\bar{z}) = \bar{T}(0, \bar{z}). \tag{5.2.15}$$

Here (5.2.12) are the boundary conditions on the side wall of the cavity and (5.2.13)-(5.2.15) express the fact that the vertical boundary layer solution must match as $\bar{x} \to \infty$ with the horizontal boundary layer solution at $x = 0$. The conditions (5.2.11) express the fact that there is no flow through the upper surface of the cavity and that the temperature there is small ($o(1)$).

For the horizontal boundary layer solution of Chapter 4, the external profiles ψ_∞ and T_∞ are given by

$$\psi_\infty(\bar{z}) = L^{\frac{1}{3}}\phi(Z), \tag{5.2.16}$$

$$T_\infty(\bar{z}) = \theta_1(Z) - \theta_0(Z), \tag{5.2.17}$$

where $\bar{z} = L^{\frac{2}{3}}Z$ and ϕ and $\theta_1 - \theta_0$ are the functions shown graphically in figures 4.2 and 4.6.

Recall that ϕ is a monotonically increasing function of Z with the properties

$$\phi(0) = 0, \quad \phi'(0) = c = 1.447, \quad \phi''(0) = -2; \phi(\infty) = a = 1.141 \tag{5.2.18}$$

and that $\theta_1 - \theta_0$ has a local maximum at $Z = Z_0 = 0.96$ with

$$(\theta_1 - \theta_0)(0) = 0, \quad (\theta_1' - \theta_0')(0) = \frac{1}{2}c^2 = 1.047,$$
$$(\theta_1 - \theta_0)(Z_0) = 0.313, \quad (\theta_1 - \theta_0)(\infty) = b = 0.229. \tag{5.2.19}$$

Note that both ϕ and $\theta_1 - \theta_0$ approach their constant limiting forms as $Z \to \infty$ with exponential decay. In the following sections we investigate various properties

119

of the vertical boundary layer system (5.2.9)-(5.2.15).

5.3 Limiting form of the vertical boundary layer solution as $\bar{x} \to \infty$

Here we analyse the behaviour of the vertical boundary layer solution near the edge of the layer. Assuming an exponential decay to the external profiles T_∞ and ψ_∞ in the form

$$\widetilde{T} \sim T_{co} + Re \sum_\lambda A(\bar{z}) e^{-\lambda(\bar{z})\bar{x}}, \quad \bar{x} \to \infty, \tag{5.3.1}$$

$$\widetilde{\psi} \sim \psi_\infty + Re \sum_\lambda B(\bar{z}) e^{-\lambda(\bar{z})\bar{x}}, \quad \bar{x} \to \infty, \tag{5.3.2}$$

substitution into (5.2.9) implies that

$$\lambda^2 B = \lambda A \tag{5.3.3}$$

and substitution into (5.2.10) implies that

$$\lambda^2 A = -(-\lambda A \psi'_\infty + T'_\infty \lambda B). \tag{5.3.4}$$

Substituting $\lambda B = A$ from (5.3.3) then shows that the function $\lambda(\bar{z})$ must satisfy the quadratic equation

$$\lambda^2 - \lambda \psi'_\infty + T'_\infty = 0, \tag{5.3.5}$$

which yields two possible solutions

$$\lambda = \lambda_\pm = \frac{\psi'_\infty \pm (\psi'^{\,2}_\infty - 4T'_\infty)^{\frac{1}{2}}}{2}. \tag{5.3.6}$$

These are acceptable only if the real part of λ is positive, ensuring exponential decay in (5.3.1)and (5.3.2). For the horizontal boundary layer profiles (5.2.16),(5.2.17) we have two situations to consider, depending on whether $\bar{z}$ is below or above the value $\bar{z}_0 = L^{\frac{2}{3}} Z_0$:

(i) $0 < \bar{z} < \bar{z}_0$: here we have $\psi'_\infty > 0$, $T'_\infty > 0$ so both roots $\lambda_\pm$ correspond to solutions with positive real part (real if $\psi'^{\,2}_\infty > 4T'_\infty$ and complex conjugates if $\psi'^{\,2}_\infty < 4T'_\infty$). Thus we can expect it to be possible to specify both $\psi_\infty(\bar{z})$ and

120

$T_\infty(\bar{z})$ in this region.

(ii) $\bar{z} > \bar{z}_0$: here we have $\psi'_\infty > 0, T'_\infty < 0$ so $(\psi'^2_\infty - 4T'_\infty)^{\frac{1}{2}} > \psi'_\infty$ and hence only λ_+ has positive real part (λ_- has negative real part). Thus we can only expect to be able to specify one of $\psi_\infty(\bar{z})$ and $T_\infty(\bar{z})$ in this region.

For this reason we cannot expect the horizontal boundary layer solution obtained in Chapter 4 to be the correct one, as it determines both ψ_∞ and T_∞ in the region $\bar{z} > \bar{z}_0$. It might have been feasible if it had led to a horizontal boundary layer solution with $\psi'_\infty, \quad T'_\infty > 0$ for all $\bar{z}$, but clearly this is not the case.

5.4 Integral properties of the vertical boundary layer

Next we consider some general properties of the system (5.2.9)-(5.2.15). From (5.2.9), (5.2.13) it follows that

$$-\frac{\partial \widetilde{\psi}}{\partial \bar{x}} = \widetilde{T} - T_\infty(\bar{z}) \tag{5.4.1}$$

and (5.2.10) implies that

$$\frac{\partial \widetilde{T}}{\partial \bar{x}}\bigg|_{\bar{x}=\infty} - \frac{\partial \widetilde{T}}{\partial \bar{x}}\bigg|_{\bar{x}=0} = 0 = -\int_0^\infty \left(\frac{\partial}{\partial \bar{x}}(\widetilde{T}\frac{\partial \widetilde{\psi}}{\partial \bar{z}}) - \frac{\partial}{\partial \bar{z}}(\widetilde{T}\frac{\partial \widetilde{\psi}}{\partial \bar{x}}) \right) d\bar{x}$$

$$= -\psi'_\infty T_\infty + \frac{\partial}{\partial \bar{z}} \int_0^\infty \widetilde{T}\frac{\partial \widetilde{\psi}}{\partial \bar{x}} d\bar{x}. \tag{5.4.2}$$

Thus making use of (5.2.11)

$$\int_0^\infty \widetilde{T}\frac{\partial \widetilde{\psi}}{\partial \bar{x}} d\bar{x} = \int_0^{\bar{z}} \psi'_\infty T_\infty d\bar{z} \quad \text{for all } \bar{z} \tag{5.4.3}$$

or, alternatively

$$\int_0^\infty \widetilde{T}\frac{\partial \widetilde{\psi}}{\partial \bar{x}} d\bar{x} = \psi_\infty T_\infty - \int_0^{\bar{z}} \psi_\infty T'_\infty d\bar{z} \quad \text{for all } \bar{z}. \tag{5.4.4}$$

This is a heat-flux equation for the vertical boundary layer, sometimes referred to as an energy-integral equation (see, for example, Schlichting 1968, p.291). From

121

the horizontal boundary layer analysis we know from (4.3.12) that

$$\int_0^\infty \psi_\infty T'_\infty d\bar{z} = 0. \tag{5.4.5}$$

Hence letting $\bar{z} \to \infty$ in (5.4.3),(5.4.4) we have

$$\int_0^\infty \tilde{T} \frac{\partial \tilde{\psi}}{\partial \bar{x}} d\bar{x} \quad \to \quad \psi_\infty(\infty) T_\infty(\infty) = \int_0^\infty \psi'_\infty T_\infty d\bar{z}$$

$$= \quad L^{\frac{1}{3}} ab \quad \text{as} \quad \bar{z} \to \infty. \tag{5.4.6}$$

The vertical boundary layer must possess this integral property as $\bar{z} \to \infty$, implied by the overall heat transfer balance in the system. If a and b are both non zero, as in the analysis of Chapter 4, there is a heat transfer (down) associated with $-\int_{V.B.L} \tilde{w}\tilde{T} d\bar{x}$ which balances the transfer (up) $\int_0^L \bar{w}\bar{T} dx$ into the horizontal boundary layer from the core. For any horizontal cross-section AB of the cavity (see figure 5.2) we can integrate the heat equation (3.1.3) over the region $ABCD$ to give

$$\int_{AB} \frac{\partial T}{\partial z} dx \quad = \quad \int_0^L \int_0^{z_0} \frac{\partial}{\partial x}(T\frac{\partial \psi}{\partial z}) dx dz - \int_0^L \int_0^{z_0} \frac{\partial}{\partial z}(T\frac{\partial \psi}{\partial x}) dx dz,$$

$$= \quad \int_0^{z_0} \left[T\frac{\partial \psi}{\partial z} \right]\Big|_0^L dz - \int_0^L (T\frac{\partial \psi}{\partial x})_{AB} dx,$$

$$= \quad 0 - \int_0^L (T\frac{\partial \psi}{\partial x})_{AB} dx. \tag{5.4.7}$$

Hence along any cross-section AB

$$\int_A^B (\frac{\partial T}{\partial z} + T\frac{\partial \psi}{\partial x}) dx = 0. \tag{5.4.8}$$

At the top of the cavity $z = 1$ we recover $\int_A^B \frac{\partial T}{\partial z} dx = 0$. At the edge of the horizontal boundary layer we also have $\frac{\partial T}{\partial z} \approx 0$ so we must have

$$\int_A^B T\frac{\partial \psi}{\partial x} dx \approx 0. \tag{5.4.9}$$

This implies that

$$\int_{\substack{V.B.L \\ \bar{z} \to \infty}} \tilde{T} \frac{\partial \tilde{\psi}}{\partial \bar{x}} d\bar{x} + \int_{\substack{H.B.L \\ \bar{z} \to \infty}} \bar{T} \frac{\partial \bar{\psi}}{\partial x} dx = 0 \tag{5.4.10}$$

122

but

$$\int_{\substack{H.B.L \\ \bar{z}\to\infty}} \bar{T}\frac{\partial\bar{\psi}}{\partial x}dx = \left[(\bar{T}\bar{\psi})_{\bar{z}\to\infty}\right]_0^L - \int_0^L (\bar{\psi}\frac{\partial\bar{T}}{\partial x})_{\bar{z}=\infty}dx,$$
$$= -T_\infty(\infty)\psi_\infty(\infty) - 0$$
$$= -L^{\frac{1}{3}}ab \qquad (5.4.11)$$

and so (5.4.10) confirms the result (5.4.6).

5.5 Solution structure in the vertical boundary layer as $\bar{z} \to 0$

From the horizontal boundary layer solution we expect that the external profiles have the forms

$$\psi_\infty = a_\infty\bar{z} + \dots, \quad T_\infty = b_\infty\bar{z} + \dots, \quad \bar{z} \to 0, \qquad (5.5.1)$$

with $a_\infty, b_\infty > 0$ so a solution in the vertical boundary layer is sought in the form

$$\tilde{\psi} = \bar{z}f(\bar{x}) + \dots, \quad \tilde{T} = \bar{z}g(\bar{x}) + \dots, \quad \bar{z} \to 0. \qquad (5.5.2)$$

Substitution into (5.2.9), (5.2.10) gives

$$-f' = g - b_\infty, \qquad (5.5.3)$$
$$g'' = -fg' + f'g \qquad (5.5.4)$$

and from (5.2.12),(5.2.13) the boundary conditions are

$$f = g' = 0, \quad \bar{x} = 0, \qquad (5.5.5)$$
$$f \to a_\infty, \quad g \to b_\infty, \quad \bar{x} \to \infty. \qquad (5.5.6)$$

This implies that f satisfies the system

$$f''' + ff'' + f'(b_\infty - f') = 0, \qquad (5.5.7)$$
$$f = f'' = 0, \quad \bar{x} = 0, \qquad (5.5.8)$$
$$f \to a_\infty, \quad \bar{x} \to \infty. \qquad (5.5.9)$$

123

As $\bar{x} \to \infty$ we expect

$$f \sim a_\infty + Re(k_+ e^{-\bar{\lambda}_+ \bar{x}} + k_- e^{-\bar{\lambda}_- \bar{x}}), \qquad (5.5.10)$$

where $\bar{\lambda} = \bar{\lambda}_\pm$ are the two roots

$$\bar{\lambda}_\pm = \frac{a_\infty \pm (a_\infty^2 - 4b_\infty)^{\frac{1}{2}}}{2}, \qquad (5.5.11)$$

which are positive if $a_\infty^2 > 4b_\infty$ and complex conjugates with positive real part if $a_\infty^2 < 4b_\infty$. The constants $k_\pm$ in (5.5.10) must be chosen to ensure $f = f'' = 0$ at $\bar{x} = 0$.

One method of computing f is to let

$$f(\bar{x}) = b_\infty^{\frac{1}{2}} \hat{f}(\hat{x}), \quad \bar{x} = b_\infty^{-\frac{1}{2}} \hat{x} \qquad (5.5.12)$$

and then solve the system

$$\hat{f}''' \;+\; \hat{f}\hat{f}'' + \hat{f}'(1 - \hat{f}') = 0, \qquad (5.5.13)$$

$$\hat{f} \;=\; \hat{f}'' = 0, \quad \hat{f}' = k_0, \quad \hat{x} = 0, \qquad (5.5.14)$$

for different values of the constant k_0. The solution is computed outwards from the origin using a fourth order Runge-Kutta scheme to obtain

$$\hat{f}(\infty) = \hat{a}(k_0). \qquad (5.5.15)$$

Values of $\hat{a}$ for various values of k_0 in the range $0 < k_0 \le 1$ are shown in table 5.1 and typical graphs of the function $\hat{f}$ are shown in figures 5.3-5.13. For $k_0 \ge 1$ (figures 5.12, 5.13) $\hat{f}$ continues to increase with $\hat{x}$ and a constant limit (5.5.15) is not achieved as $\hat{x} \to \infty$.

From (5.5.9) we require $a_\infty = b_\infty^{\frac{1}{2}} \hat{a}(k_0)$ so that for given values of a_∞ and b_∞ the relevant value of $\hat{a}$ is determined by

$$\hat{a} = a_\infty b_\infty^{-\frac{1}{2}} \qquad (5.5.16)$$

and (in principle) the corresponding value of k_0 is determined from table 5.1. Note the oscillatory behaviour of the solution $\hat{f}$ in figures 5.3 - 5.9 for $\hat{a} < 2$, consistent with the existence of complex conjugate roots of (5.5.11) in this case.

124

k_0	$\hat{a}$
0.0	0.000
0.1	0.129
0.2	0.237
0.3	0.325
0.4	0.432
0.5	0.628
0.6	0.979
0.7	1.606
0.8	2.902
0.9	6.861
1.0	∞

Table 5.1:

Note also that as k_0 approaches the value 1, $\hat{f}$ approaches the exact solution $\hat{f} = \hat{x}$ of (5.5.13), (5.5.14) and in this case $\hat{a} \to \infty$.

From the horizontal boundary layer solution of Chapter 4 , $a_\infty = L^{-\frac{1}{3}}c$ and $b_\infty = \frac{1}{2}L^{-\frac{2}{3}}c^2$ where c is given by (4.2.40) , so that this solution corresponds to the case $\hat{a} = \sqrt{2}$ where the behaviour at the edge of the vertical boundary layer is oscillatory. Note also that for the marginal case $\hat{a} = 2$, the two roots $\bar{\lambda}_\pm$ in (5.5.11) are equal and then the two exponentials in (5.5.10) are replaced by the form $e^{-\bar{\lambda}_+ \bar{x}}(k_+ + k_- \bar{x})$.

5.6 Integral method for the region $\bar{z} > \bar{z}_0$

In this section we consider the lower section of the vertical boundary layer $\bar{z} \geq \bar{z}_0$ where $\bar{z}_0$ is defined as the position at which $T'_\infty = 0$. The analysis of Section 5.3 suggests that in this region only one of the two external profiles T_∞ and ψ_∞ can be specified at the edge of the layer. We can then attempt to use an integral method to determine an approximation to T_∞ if ψ_∞ is given (or vice versa) following the approach adopted by Simpkins and Blythe (1980). From (5.2.10),

$$0 = -\frac{\partial \tilde{T}}{\partial \bar{x}}\bigg|_{\bar{x}=0} = -\int_0^\infty \left(\frac{\partial}{\partial \bar{x}}(\tilde{T}\frac{\partial \tilde{\psi}}{\partial \bar{z}}) - \frac{\partial}{\partial \bar{z}}(\tilde{T}\frac{\partial \tilde{\psi}}{\partial \bar{x}}) \right) d\bar{x} \qquad (5.6.1)$$

and thus making use of (5.2.12) we have

$$
\begin{aligned}
0 &= \left[\tilde{T}\frac{\partial\tilde{\psi}}{\partial\bar{z}}\right]_0^\infty - \frac{d}{d\bar{z}}\int_0^\infty \tilde{T}(T_\infty - \tilde{T})d\bar{x}, \\
&= \psi_\infty' T_\infty - \frac{d}{d\bar{z}}\int_0^\infty \tilde{T}(T_\infty - \tilde{T})d\bar{x},
\end{aligned}
\tag{5.6.2}
$$

which can be rearranged to give

$$
\psi_\infty T_\infty' = \frac{d}{d\bar{z}}\int_0^\infty (\tilde{T} - T_\infty)^2 d\bar{x}.
\tag{5.6.3}
$$

Suppose we approximate

$$
\tilde{T} = \bar{T}_\infty(\bar{z})G(\eta) + b, \quad \eta = \frac{\bar{x}}{\delta(\bar{z})},
\tag{5.6.4}
$$

where $\bar{T}_\infty = T_\infty - b$ and then, from (5.2.9),

$$
\tilde{w} = -\frac{\partial\tilde{\psi}}{\partial\bar{x}} = -\bar{T}_\infty(1 - G) = -\bar{T}_\infty F(\eta),
\tag{5.6.5}
$$

where $F = 1 - G$. The boundary conditions require that $G'(0) = 0$ and $G(\infty) = 1$. Equation (5.6.3) implies that

$$
\psi_\infty \bar{T}_\infty' = \frac{d}{d\bar{z}}\left[\delta\bar{T}_\infty^2 \int_0^\infty F^2 d\eta\right]
\tag{5.6.6}
$$

and

$$
\psi_\infty = \bar{T}_\infty \delta \int_0^\infty F d\eta,
\tag{5.6.7}
$$

in which case

$$
0 = -\psi_\infty \bar{T}_\infty' + \frac{d}{d\bar{z}}(A\psi_\infty \bar{T}_\infty),
\tag{5.6.8}
$$

where

$$
A = \frac{\int_0^\infty F^2 d\eta}{\int_0^\infty F d\eta}.
\tag{5.6.9}
$$

Equation(5.6.8) can be rewritten as

$$
0 = (A - 1)\psi_\infty \bar{T}_\infty' + A\psi_\infty' \bar{T}_\infty
\tag{5.6.10}
$$

and solved to give

$$
\bar{T}_\infty = A_\infty \psi_\infty^{\frac{A}{1-A}},
\tag{5.6.11}
$$

126

where A_∞ is an arbitrary constant. Now if $\bar{T}_\infty = A_0$, $\psi_\infty = L^{\frac{1}{3}}A_1$ at $\bar{z} = \bar{z}_0$ then

$$A_\infty = A_0 (L^{\frac{1}{3}}A_1)^{\frac{A}{A-1}} \tag{5.6.12}$$

and this completes the solution (5.6.11) for $\bar{T}_\infty$ in terms of ψ_∞.

However in order that $\psi'_\infty > 0$ and $T'_\infty < 0$ in the region $\bar{z} > \bar{z}_0$ we need $A > 1$, that is

$$\int_0^\infty F^2 d\eta > \int_0^\infty F d\eta. \tag{5.6.13}$$

This cannot be ruled out because if $G(0) < 0$ then $F(0) > 1$ and so $F^2 > F$ for values of η near the wall. However, (5.6.11) would imply that $\bar{T}_\infty \to 0$ as $\bar{z} \to \infty$. Thus the integral method does not appear to give a reasonable solution on the basis that $\psi'_\infty > 0$ and $T'_\infty < 0$ in the region $\bar{z} > \bar{z}_0$. We note however that it could give a reasonable solution if $\psi'_\infty < 0$ and $T'_\infty < 0$ in which case $A < 1$ and the vertical layer expels fluid back into the horizontal boundary layer. Indeed, on the assumption that $\bar{T}_\infty \to 0$ as $\bar{z} \to \infty$ (so that $T_\infty \to b$ as $\bar{z} \to \infty$), (5.6.11) would then imply that $\psi_\infty \to 0$ as $\bar{z} \to \infty$ and the circulation would essentially be completed within the vertical/horizontal boundary layer system. The vertical boundary layer thickness $\delta(\bar{z})$ given by (5.6.7) is

$$\delta(\bar{z}) = \frac{\psi_\infty}{\bar{T}_\infty \int_0^\infty F d\eta} = \frac{\psi_\infty^{\frac{1-2A}{1-A}}}{A_\infty \int_0^\infty F d\eta} \tag{5.6.14}$$

and with $\frac{1}{2} < A < 1$ and $\psi_\infty \to 0$ as $\bar{z} \to \infty$, this predicts that $\delta \to \infty$ as $\bar{z} \to \infty$, which is not unreasonable in comparison with the full numerical solution at large Darcy-Rayleigh numbers in Chapter 3.

5.7   Asymptotic solution of the vertical boundary layer equations as $\bar{z} \to \infty$

In this section we investigate possible asymptotic forms of the vertical boundary layer system (5.2.9)-(5.2.13) as $\bar{z} \to \infty$. It is instructive to begin by considering solutions for which

$$\psi_\infty \to L^{\frac{1}{3}}a, \quad T_\infty \sim b + \frac{\bar{c}}{\bar{z}}, \quad \bar{z} \to \infty \tag{5.7.1}$$

so that the leading terms in both ψ_∞ and T_∞ are consistent with the horizontal boundary layer solution of Chapter 4. The algebraic correction to T_∞ involving $\bar{c} \geq 0$ is not consistent with that solution but is included to allow analytical insight to be gained into the general nature of the vertical boundary layer system; the horizontal boundary layer solution of Chapter 4 would imply an exponentially small correction as $\bar{z} \to \infty$ and so can be considered as the limiting case when $\bar{c} = 0$.

First note that if in the solution for $\tilde{T}$ as $\bar{z} \to \infty$, T_∞ were allowed to remain unchanged across the layer so that

$$\tilde{\psi} \sim \tilde{\psi}_0, \quad \tilde{T} \sim T_\infty(\bar{z}) + \tilde{T}_0, \tag{5.7.2}$$

say, then $\tilde{\psi}_0$ and the perturbation $\tilde{T}_0$ would satisfy the equations

$$\frac{\partial \tilde{\psi}_0}{\partial \bar{x}} = -\tilde{T}_0, \quad \frac{\partial \tilde{T}_0}{\partial \bar{x}^2} = T'_\infty \frac{\partial \tilde{\psi}_0}{\partial \bar{x}}, \tag{5.7.3}$$

in which case, assuming $T'_\infty < 0$,

$$\tilde{T}_0 = \tilde{A}_0 e^{-(-T'_\infty)^{\frac{1}{2}} \bar{x}}. \tag{5.7.4}$$

However, the wall condition requires $\frac{\partial \tilde{T}_0}{\partial \bar{x}} = 0$ at $\bar{x} = 0$ in which case $\tilde{A}_0 = 0$; a solution for $\tilde{\psi}_0$ consistent with the wall condition $\tilde{\psi}_0 = 0$ at $\bar{x} = 0$ and (5.7.1) cannot then be found.

Instead, a solution consistent with (5.7.1) must be sought in the form

$$\tilde{\psi} \sim \bar{F}(\bar{\eta}), \quad \tilde{T} \sim b + \bar{z}^{-1} \bar{G}(\bar{\eta}), \tag{5.7.5}$$

where the balance of terms in both (5.2.9) and the heat equation (5.2.10) requires that $\bar{\eta} = \bar{x}/\bar{z} = O(1)$. Substitution into (5.2.9) and (5.2.10) gives

$$\bar{G}'' + \bar{F}'\bar{G} = 0, \tag{5.7.6}$$

$$\bar{F}'' = -\bar{G}', \tag{5.7.7}$$

and the requirements that $\bar{G}(\infty) = \bar{c}$ and $\bar{F}'(\infty) = 0$ give

$$\bar{F}' = \bar{c} - \bar{G}. \tag{5.7.8}$$

128

Thus $\bar{F}'$ can be eliminated in (5.7.6) giving

$$\bar{G}'' + \bar{G}(\bar{c} - \bar{G}) = 0, \tag{5.7.9}$$

to be solved subject to

$$\bar{G}' = 0 \quad (\bar{\eta} = 0), \quad \bar{G} \to \bar{c} \quad (\bar{\eta} \to \infty). \tag{5.7.10}$$

One integration of (5.7.9) and use of (5.7.10) gives

$$\bar{G}'^2 = \frac{1}{3}(\bar{G} - \bar{c})^2(2\bar{G} + \bar{c}). \tag{5.7.11}$$

Inspection of the phase plane then shows that a solution for $\bar{G}$ consistent with (5.7.10) is then possible with $\bar{G}$ varying from $-\frac{1}{2}\bar{c}$ at $\bar{\eta} = 0$ to $\bar{c}$ at $\bar{\eta} = \infty$. This solution can be found by one further integration of (5.7.11) using the substitution $v^2 = 2\bar{G} + \bar{c}$ giving

$$\bar{G} = \frac{1}{2}\bar{c}\left(3\tanh^2(\bar{c}^{\frac{1}{2}}\bar{\eta}/2) - 1\right) \tag{5.7.12}$$

and the corresponding solution for $\bar{F}'$ is

$$\bar{F}' = \frac{3}{2}\bar{c}\,\text{sech}^2(\bar{c}^{\frac{1}{2}}\bar{\eta}/2), \tag{5.7.13}$$

which indicates a downward vertical velocity $(\bar{F}' > 0)$ reaching a maximum value $(\bar{F}' = \frac{3}{2}\bar{c})$ at the sidewall $\bar{\eta} = 0$. The solution for $\bar{F}$ satisfying $\bar{F}(0) = 0$ is

$$\bar{F} = 3\bar{c}^{\frac{1}{2}}\tanh(\bar{c}^{\frac{1}{2}}\bar{\eta}/2) \tag{5.7.14}$$

and the value of $\bar{c}$ is finally fixed by requiring that $\bar{F}(\infty) = L^{\frac{1}{3}}a$ in which case

$$L^{\frac{1}{3}}a = 3\bar{c}^{\frac{1}{2}}. \tag{5.7.15}$$

This shows that for a specified external form ψ_∞, the corresponding form of T_∞ can be calculated from the vertical boundary layer (or vice versa). This is consistent with the results of Section 5.3, given that here $T'_\infty < 0$.

The asymptotic solution found here assumes that $\tilde{\psi}$ is of order one and $\tilde{T} - b$ is of order $\bar{z}^{-1}$ as $\bar{z} \to \infty$. It seems likely that in fact a whole family of possible solutions will exist for other orders of magnitude of $\tilde{\psi}$ and $\tilde{T} - b$ as $\bar{z} \to \infty$, and

that the correct orders of magnitude must be determined by matching with a consistent structure in the horizontal boundary layer. For example a structure in which $\widetilde{\psi} \to 0$ as $\bar{z} \to \infty$ would correspond, essentially, to a solution in which both $L^{\frac{1}{3}}a$ and $\bar{c}$ are small in the above analysis (with $L^{\frac{1}{3}}a \sim \bar{c}^{\frac{1}{2}}$) and the vertical layer width $\bar{\eta}$ is large (since it scales with $\bar{c}^{-\frac{1}{2}}$). This structure is considered in detail in Chapter 6.

5.8 Summary

Our analysis of the various properties of the vertical boundary layer system shows that we cannot find a satisfactory solution in the vertical boundary layer if we use the results from the horizontal boundary layer solution of Chapter 4. We must therefore consider how to solve the horizontal and vertical boundary layers together to ensure solutions in both regions which match consistently across the boundary between the regions. This will be done in the next chapter.
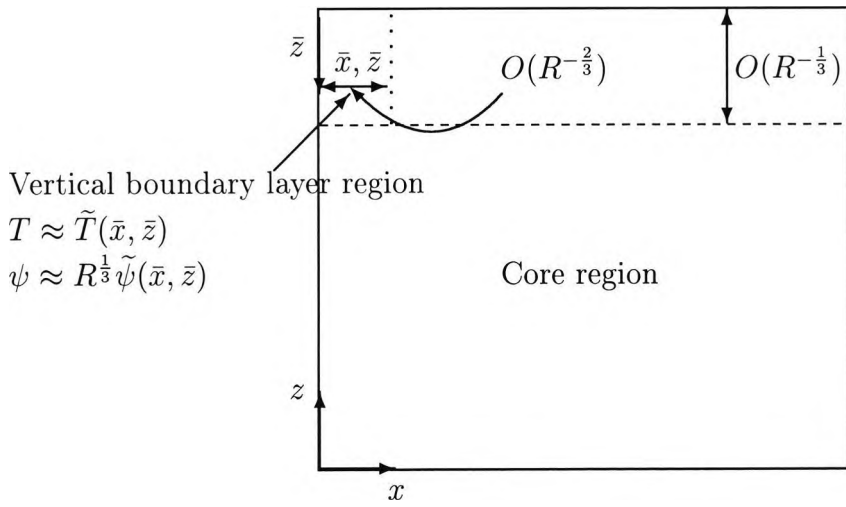
Figure 5.1: Vertical boundary layer region
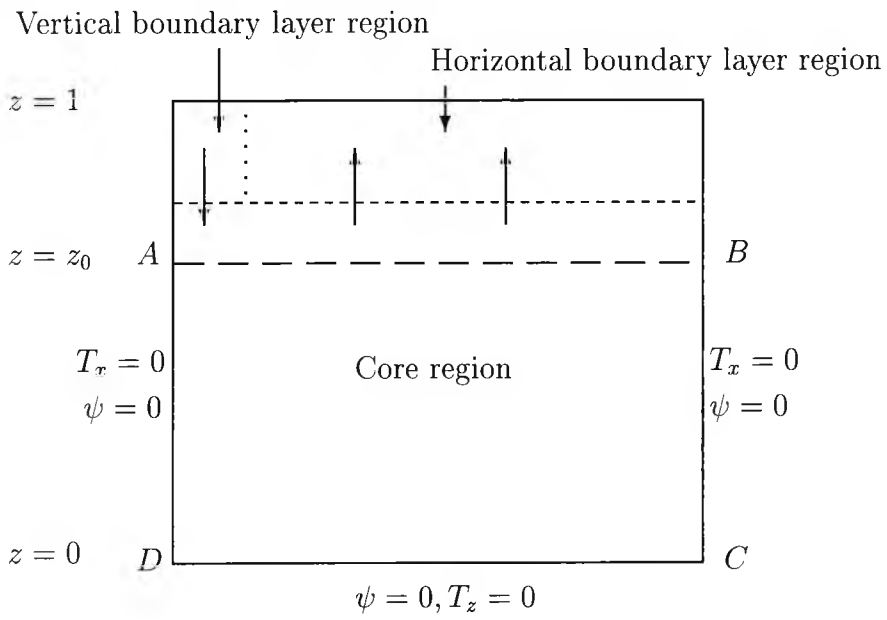
Figure 5.2: Cavity heat transfer

131
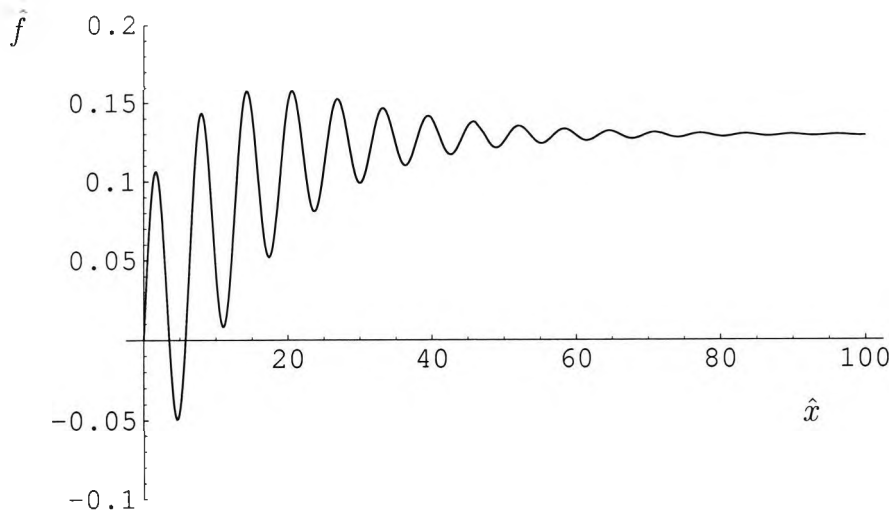
Figure 5.3: Graph for $k_0 = 0.1$
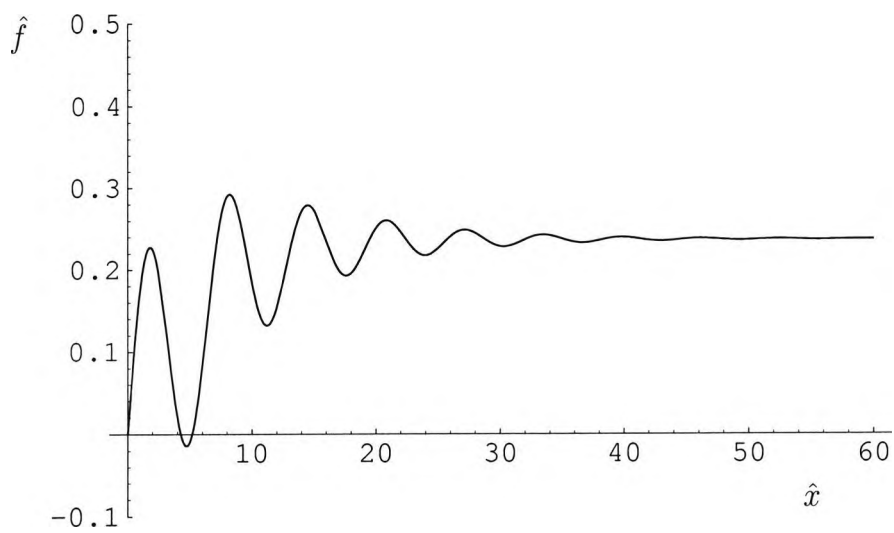
Figure 5.4: Graph for $k_0 = 0.2$

132
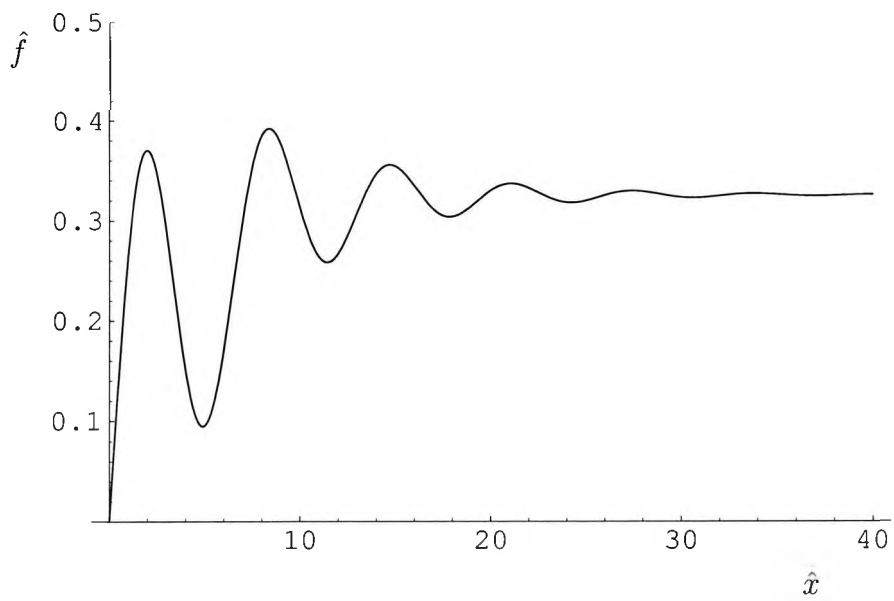
Figure 5.5: Graph for $k_0 = 0.3$
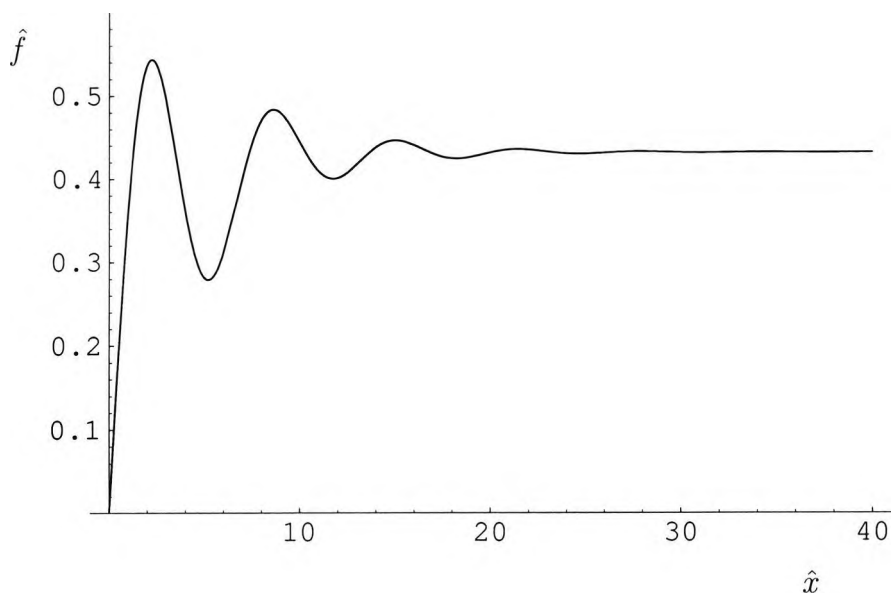
Figure 5.6: Graph for $k_0 = 0.4$

133
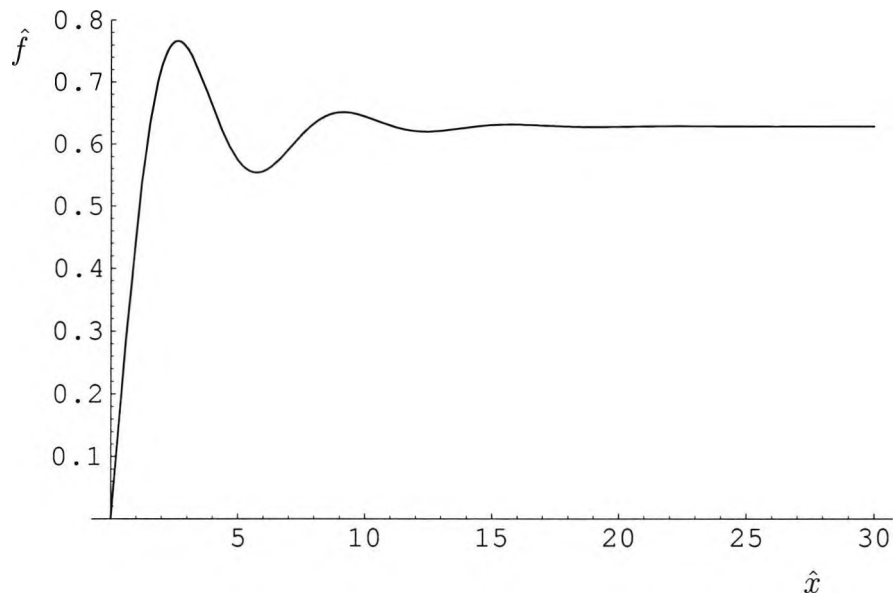
Figure 5.7: Graph for $k_0 = 0.5$
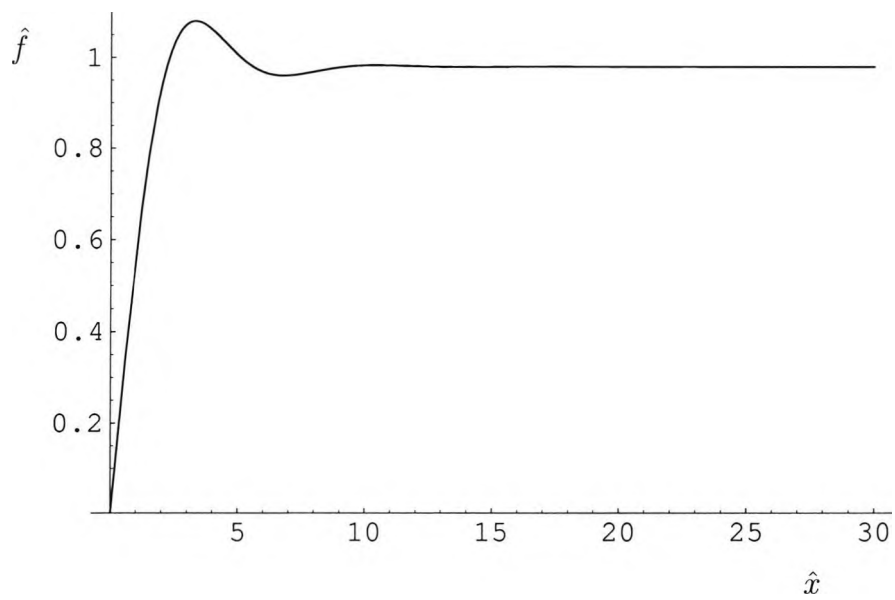
Figure 5.8: Graph for $k_0 = 0.6$

134
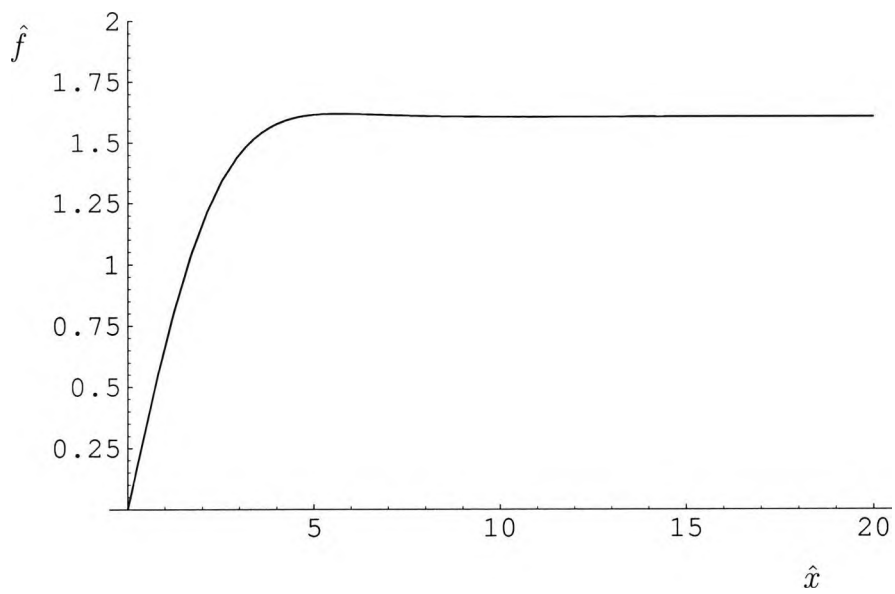
Figure 5.9: Graph for $k_0 = 0.7$
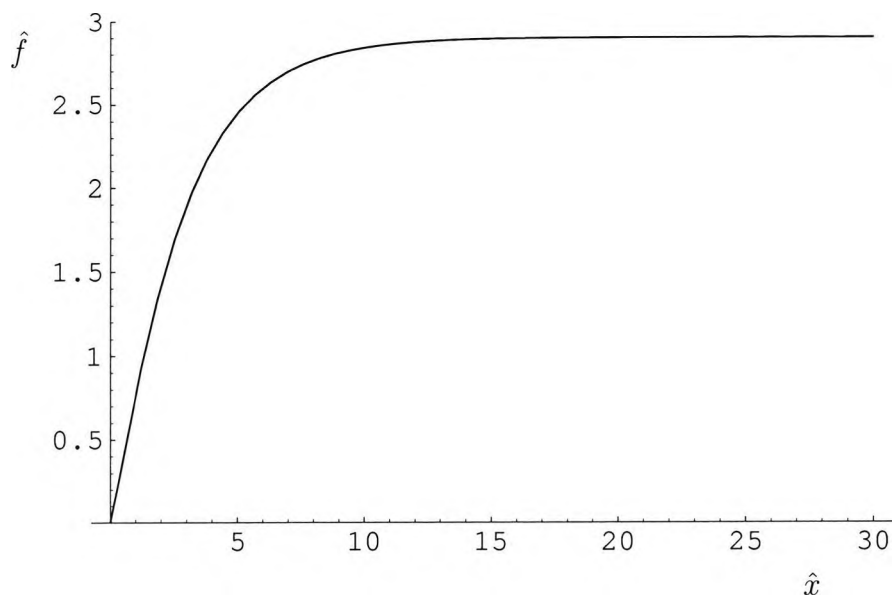
Figure 5.10: Graph for $k_0 = 0.8$

135
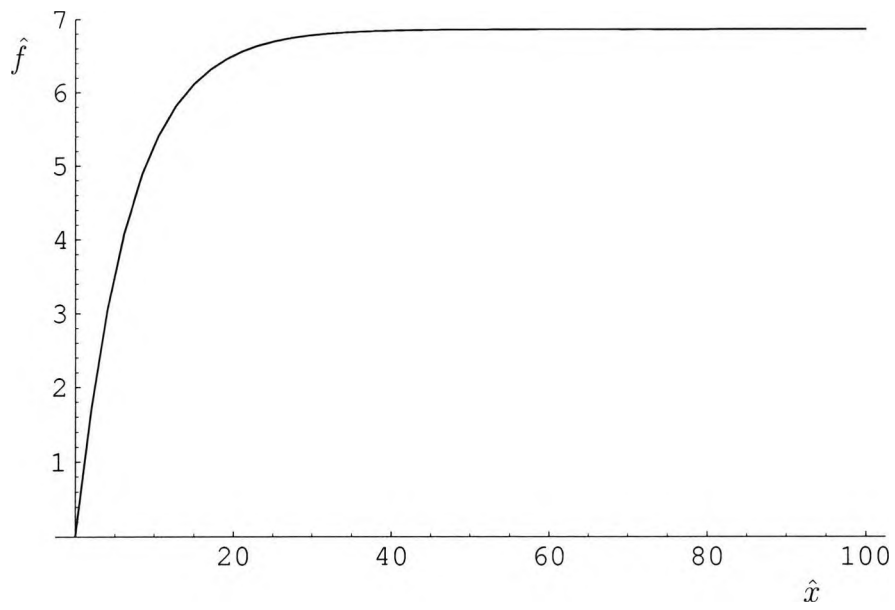
Figure 5.11: Graph for $k_0 = 0.9$
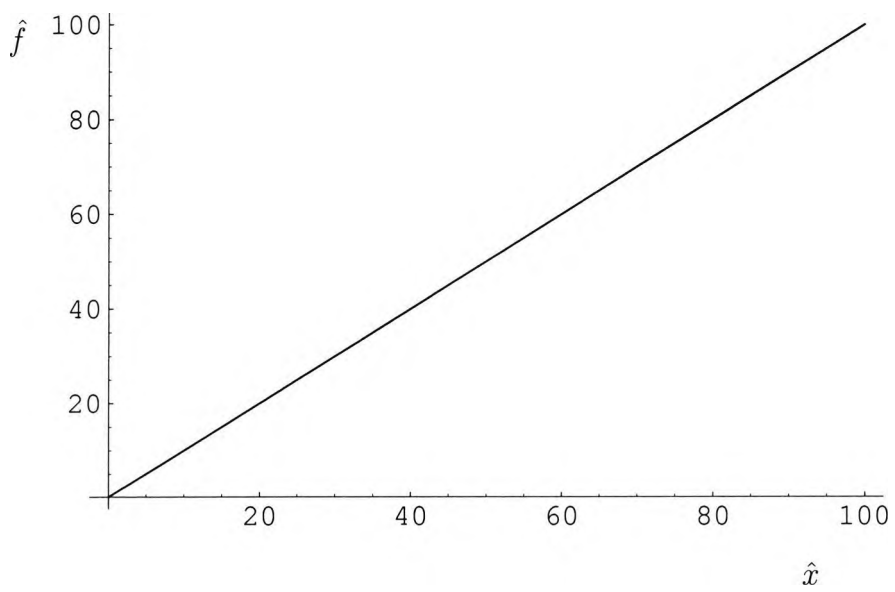
Figure 5.12: Graph for $k_0 = 1.0$

136
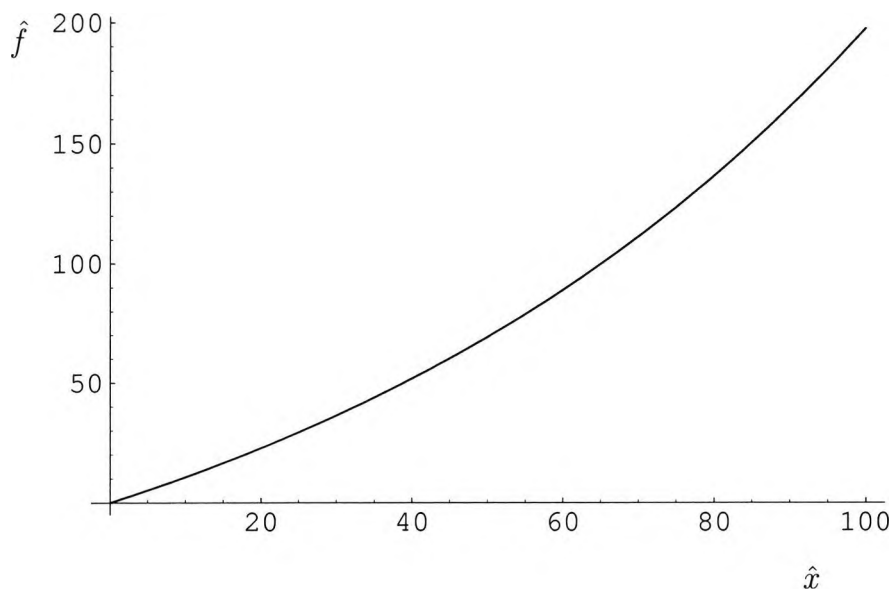
Figure 5.13: Graph for $k_0 = 1.1$

Chapter 6

Solution at Large Darcy-Rayleigh Numbers

6.1 Introduction

In this chapter we investigate the horizontal and vertical boundary layers together, with the aim of finding the correct limiting solution in the cavity as the Darcy-Rayleigh number $R \to \infty$. The problem is formulated in its simplest terms in Section 6.2 and in Section 6.3 an asymptotic solution as the boundary layer coordinate $\bar{z} \to \infty$ is determined, consistent with both the horizontal and vertical boundary layer regions. The implications of this asymptotic solution for the solution in the core region below the boundary layers are considered in Section 6.4. In Section 6.5 the asymptotic solution of Section 6.3 is combined with the approximate theory of Chapter 4 to yield an improved 'approximate' solution of the boundary layer problem. A numerical scheme for the complete solution of the combined boundary layer problem is discussed in Section 6.6 and the results are summarized in Section 6.7.

6.2 The combined boundary layer problem

Here we briefly summarize the mathematical problem posed by the combined solution of the horizontal and vertical boundary layer regions as $R \to \infty$. In order to present the problem in its simplest terms it is noted that the cavity aspect ratio L can be scaled out of the problem as follows.

138

In the horizontal boundary layer we write

$$T(x,z) = \bar{\theta}(X,Z) + \cdots, \quad \psi(x,z) = R^{\frac{1}{3}}L^{\frac{1}{3}}\bar{\phi}(X,Z) + \cdots, \qquad (6.2.1)$$

where

$$x = LX, \quad 1 - z = R^{-\frac{1}{3}}L^{\frac{2}{3}}Z \qquad (6.2.2)$$

to obtain the governing equations

$$\frac{\partial^2 \bar{\phi}}{\partial Z^2} = -\frac{\partial \bar{\theta}}{\partial X}, \qquad (6.2.3)$$

$$\frac{\partial^2 \bar{\theta}}{\partial Z^2} = \frac{\partial \bar{\phi}}{\partial X}\frac{\partial \bar{\theta}}{\partial Z} - \frac{\partial \bar{\phi}}{\partial Z}\frac{\partial \bar{\theta}}{\partial X}, \qquad (6.2.4)$$

with the boundary conditions

$$\bar{\phi} = 0, \quad \bar{\theta} = 1 - (X-1)^2, \quad Z = 0, \qquad (6.2.5)$$

$$\bar{\phi} = \frac{\partial \bar{\theta}}{\partial X} = 0, \quad X = 1, \qquad (6.2.6)$$

$$\bar{\phi} \to 0, \quad \frac{\partial \bar{\theta}}{\partial Z} \to 0 \quad , Z \to \infty. \qquad (6.2.7)$$

Here we assume a quadratic temperature profile (6.2.5) on the upper surface of the cavity and in (6.2.7) that the main circulation is completed within the horizontal and vertical boundary layers following the arguments developed in Chapter 5.

In the vertical boundary layer we write

$$T(x,z) = \tilde{\theta}(\widetilde{X},Z) + \cdots, \quad \psi(x,z) = R^{\frac{1}{3}}L^{\frac{1}{3}}\tilde{\phi}(\widetilde{X},Z) + \cdots, \qquad (6.2.8)$$

where

$$x = R^{-\frac{2}{3}}L^{\frac{1}{3}}\widetilde{X} \qquad (6.2.9)$$

to obtain the governing equations

$$\frac{\partial^2 \tilde{\phi}}{\partial \widetilde{X}^2} = -\frac{\partial \tilde{\theta}}{\partial \widetilde{X}}, \qquad (6.2.10)$$

$$\frac{\partial^2 \tilde{\theta}}{\partial \widetilde{X}^2} = \frac{\partial \tilde{\phi}}{\partial \widetilde{X}}\frac{\partial \tilde{\theta}}{\partial Z} - \frac{\partial \tilde{\phi}}{\partial Z}\frac{\partial \tilde{\theta}}{\partial \widetilde{X}}, \qquad (6.2.11)$$

with boundary conditions

$$\widetilde{\phi} \;=\; \widetilde{\theta} = 0, \quad Z = 0, \tag{6.2.12}$$

$$\widetilde{\phi} \;=\; \frac{\partial \widetilde{\theta}}{\partial \widetilde{X}} = 0, \quad \widetilde{X} = 0, \tag{6.2.13}$$

$$\widetilde{\phi} \;\to\; \widetilde{\phi}_\infty(Z), \quad \widetilde{\theta} \to \widetilde{\theta}_\infty(Z), \quad \widetilde{X} \to \infty, \tag{6.2.14}$$

and where, from matching with the horizontal boundary layer,

$$\widetilde{\phi}_\infty(Z) = \bar{\phi}(0, Z), \quad \widetilde{\theta}_\infty(Z) = \bar{\theta}(0, Z). \tag{6.2.15}$$

The combined boundary layer problem stated in (6.2.3)-(6.2.7) and (6.2.10)-(6.2.15) is independent of L and the aim of this chapter is to determine its solution.

6.3   Asymptotic solution as $Z \to \infty$

The previous analysis in Chapter 5 suggests that we need a different balance (from that of the approximate solution of Chapter 4) in the horizontal boundary layer as $Z \to \infty$ in order to match with the vertical boundary layer. We consider now the possibility that $\bar{\phi}$ and $\bar{\theta}$ have the asymptotic behaviour

$$\bar{\phi} \sim \frac{A(X)}{Z^\alpha}, \quad \bar{\theta} \sim b + \frac{C(X)}{Z^\beta}, \quad Z \to \infty, \tag{6.3.1}$$

where b is a constant and α and β are constants to be determined. The need for a balance in (6.2.3) requires that

$$\beta = \alpha + 2. \tag{6.3.2}$$

In the heat equation (6.2.4) the conduction term on the left hand side is of order $Z^{-\beta-2}$ whilst the convection terms on the right hand side are of order $Z^{-\alpha-\beta-1}$. Thus a full balance requires $\alpha = 1$, in which case $\beta = 3$ from (6.3.2). If $\alpha > 1$ the conduction term dominates leading to $C(X) = 0$ and then $A(X) = 0$ from (6.2.3), so that this is not consistent. If $\alpha < 1$ the convection term dominates and then

$$\alpha A C' - \beta A' C = 0, \tag{6.3.3}$$

140

giving

$$C = C_0 A^{\frac{\beta}{\alpha}} \tag{6.3.4}$$

where C_0 is a constant. Then (6.2.3) gives

$$A' = \frac{-\alpha^2(\alpha+1)}{C_0\beta} A^{2-\frac{\beta}{\alpha}}. \tag{6.3.5}$$

Since $\alpha < 1$ and $\beta = \alpha + 2$ it follows that $2 - \frac{\beta}{\alpha} < -1$ and since we can expect that $A(1) = 0$ it follows that $A'(1)$ is infinite. This would imply a local structure near $X = 1$, contrary to the implications of the full numerical results of Chapter 3.

Consider next the implications for the structure of the vertical boundary layer as $Z \to \infty$. Here a solution consistent with (6.3.1) would require

$$\tilde{\phi} \sim \frac{\widetilde{F}(\tilde{\eta})}{Z^\alpha}, \quad \tilde{\theta} \sim b + \frac{\widetilde{G}(\tilde{\eta})}{Z^\beta}, \tag{6.3.6}$$

where $\tilde{\eta} = \frac{\widetilde{X}}{Z^\gamma}$ and γ is a further constant to be determined. Substitution of (6.3.6) into (6.2.10) shows that

$$\gamma = \beta - \alpha \tag{6.3.7}$$

and, from (6.3.2), it follows that $\gamma = 2$. In the heat equation a balance between conduction and convection then requires $\alpha = 1$, whilst if $\alpha < 1$ the convection terms dominate. Whilst the latter possibility can be pursued it does not appear to lead to a consistent structure within a conductive sublayer near the wall, certainly not for general values of $\alpha < 1$. Here we also appeal to the asymptotic structure identified in Section 5.7 which showed that, in the present notation, if $\tilde{\phi}_\infty \sim a$, $\tilde{\theta}_\infty \sim b + \bar{c}Z^{-1}$ as $Z \to \infty$ then a and $\bar{c}$ are related by the formula

$$a = 3\bar{c}^{\frac{1}{2}}. \tag{6.3.8}$$

The more general structure (6.3.6) is equivalent to a of order $Z^{-\alpha}$ and $\bar{c}$ of order $Z^{1-\beta}$ in which case (6.3.8) suggests that α and β should be related by

$$-2\alpha = 1 - \beta. \tag{6.3.9}$$

This, together with (6.3.2), gives

$$\alpha = 1, \quad \beta = 3. \tag{6.3.10}$$

These arguments, then, suggest that an asymptotic structure as $Z \to \infty$ should be investigated in which $\alpha = 1$ and $\beta = 3$ and there is a full balance between conduction and convection as $Z \to \infty$ in both the horizontal and vertical boundary layers. Further evidence for the correctness of this structure is discussed in relation to the implied structure of the core region below the horizontal and vertical boundary layers, which is considered in Section 6.4 below. We proceed then by assuming that

$$\widetilde{\phi}_\infty \sim A_0 Z^{-1}, \quad \widetilde{\theta}_\infty \sim b + C_0 Z^{-3}, \quad Z \to \infty, \tag{6.3.11}$$

where A_0 and C_0 are constants to be determined. In the vertical boundary layer

$$\widetilde{\phi} \sim Z^{-1} \widetilde{F}(\widetilde{\eta}), \quad \widetilde{\theta} \sim b + Z^{-3} \widetilde{G}(\widetilde{\eta}), \tag{6.3.12}$$

where $\widetilde{\eta} = \frac{\widetilde{X}}{Z^2}$. Substitution into (6.2.10) and use of (6.3.11) gives

$$-\widetilde{F}' = \widetilde{G} - C_0 \tag{6.3.13}$$

and from (6.2.11)

$$\widetilde{G}'' = \widetilde{F}\widetilde{G}' - 3\widetilde{F}'\widetilde{G}. \tag{6.3.14}$$

Elimination of $\widetilde{G}$ then shows that $\widetilde{F}$ satisfies the third order system

$$\widetilde{F}''' - \widetilde{F}\widetilde{F}'' - 3\widetilde{F}'(C_0 - \widetilde{F}') = 0, \tag{6.3.15}$$

with boundary conditions

$$\widetilde{F} = \widetilde{F}'' = 0, \quad \widetilde{\eta} = 0, \tag{6.3.16}$$

$$\widetilde{F}' \to 0, \quad \widetilde{\eta} \to \infty. \tag{6.3.17}$$

The constant C_0 is assumed positive and can be eliminated using the transformation

$$\widetilde{F}(\widetilde{\eta}) = C_0^{\frac{1}{2}} \hat{F}(\hat{\eta}), \quad \widetilde{\eta} = C_0^{-\frac{1}{2}} \hat{\eta} \tag{6.3.18}$$

142

to obtain

$$\hat{F}''' \quad - \quad \hat{F}\hat{F}'' + 3\hat{F}'(\hat{F}' - 1) = 0, \tag{6.3.19}$$

$$\hat{F} \quad = \quad \hat{F}'' = 0, \quad \hat{\eta} = 0, \tag{6.3.20}$$

$$\hat{F}' \quad \to \quad 0, \quad \hat{\eta} \to \infty. \tag{6.3.21}$$

We expect the solution of this system to yield the numerical value of $\hat{F}(\infty) = k$, say, in which case (6.3.18) and (6.3.11) together imply that A_0 and C_0 are related by the equation

$$A_0 = kC_0^{\frac{1}{2}}. \tag{6.3.22}$$

The solution of (6.3.19)-(6.3.21) is not straightforward and it is by no means clear that a solution exists for which $\hat{F}$ approaches a constant value as $\hat{\eta} \to \infty$, given that $\hat{F} = \hat{\eta}$ is one solution of (6.3.19) which satisfies both of the conditions (6.3.20) at the origin, but does not have the required behaviour at large $\hat{\eta}$. Computations of (6.3.19) using a shooting method based on a fourth order Runge Kutta scheme and starting from the conditions (6.3.20) together with $\hat{F}' = k_1$ at $\hat{\eta} = 0$ were inconclusive and generally approached the singular form

$$\hat{F} \sim 6(\hat{\eta} - \hat{\eta}_0)^{-1} \quad \text{as} \quad \hat{\eta} \to \hat{\eta}_{0-}, \tag{6.3.23}$$

with the value of $\hat{\eta}_0$ depending on the value of k_1. However, there are solutions for which $\hat{F}$ approaches a finite value ,k, as $\hat{\eta} \to \infty$ in which

$$\hat{F} \sim k + k_1 e^{-c_1 \hat{\eta}} + k_2 e^{-2c_1 \hat{\eta}}. \tag{6.3.24}$$

Substitution into (6.3.19) shows that if $k > 0$ a non-zero solution for c_1 is possible with

$$c_1 = \frac{1}{2}\left\{-k + (k^2 + 12)^{\frac{1}{2}}\right\} \tag{6.3.25}$$

and

$$k_2 = \frac{k_1^2 c_1}{4c_1^2 + 2kc_1 - 3}. \tag{6.3.26}$$

In fact, if $\hat{F}$ is approximated by (6.3.24) for all $\hat{\eta}$ and the boundary conditions $\hat{F} = \hat{F}'' = 0$ applied at $\hat{\eta} = 0$ we obtain the equations

$$k + k_1 + k_2 \quad = \quad 0, \tag{6.3.27}$$

143

$$c_1^2(k_1 + 4k_2) = 0, \qquad (6.3.28)$$

giving $k_1 = -\frac{4}{3}k$ and $k_2 = \frac{1}{3}k$ and then (6.3.26) together with (6.3.25) yields the result

$$k = \frac{27}{(858)^{\frac{1}{2}}} \approx 0.922, \qquad (6.3.29)$$

with

$$c_1 = \left(\frac{39}{22}\right)^{\frac{1}{2}} \approx 1.331, \quad k_1 = -\frac{4}{3}k \approx -1.229, \quad k_2 = \frac{1}{3}k \approx 0.307. \qquad (6.3.30)$$

The corresponding gradient of $\hat{F}$ at the origin is

$$\hat{F}'(0) = \frac{2}{3}kc_1 \approx 0.818. \qquad (6.3.31)$$

This approximate solution based on the expansion (6.3.24) about $\hat{\eta} = \infty$ gives some confidence that there may be a suitable solution of (6.3.19)-(6.3.21). In fact, it can be expected that a suitable solution of (6.3.19)-(6.3.21) is only possible if $\hat{F}'(0) > 1$. Assuming that the magnitude of the downward velocity (associated with $\hat{F}'$) reaches a maximum at the wall $\hat{\eta} = 0$ (where $\hat{F}'' = 0$) rather than a minimum, it follows that $\hat{F}'''(0) \leq 0$. But (6.3.19) evaluated at $\hat{\eta} = 0$ gives $\hat{F}'''(0) = 3\hat{F}'(0)(1 - \hat{F}'(0))$ and since the solution for which $\hat{F}'(0) = 1$ does not have the required behaviour as $\hat{\eta} \to \infty$ it follows that a consistent solution requires both $\hat{F}'''(0) < 0$ and $\hat{F}'(0) > 1$.

A numerical solution of (6.3.19)-(6.3.21) was obtained as follows. The expansion (6.3.24) was used in a numerical scheme based on shooting inwards from a suitably large value $\hat{\eta}_\infty$ of $\hat{\eta}$ using a fourth order Runge Kutta scheme. At $\hat{\eta} = 0$ the values of $\hat{F}$ and $\hat{F}''$ define the two quantities

$$p(k, k_1) = \hat{F}(0), \qquad (6.3.32)$$
$$q(k, k_1) = \hat{F}''(0), \qquad (6.3.33)$$

as functions of the arbitrary parameters k and k_1 in the asymptotic form (6.3.24). We then use Newton's method to solve the pair of nonlinear equations

$$p(k, k_1) = 0, \quad q(k, k_1) = 0. \qquad (6.3.34)$$

The values given in (6.3.29) and (6.3.30) are used as initial estimates of k and

144

k_1 and to find new approximations the functions p and q are expanded in Taylor series about the point (k,k_1) leading to the Newton equations

$$p(k, k_1) + \frac{\partial p}{\partial k}(k, k_1)\delta k + \frac{\partial p}{\partial k_1}(k, k_1)\delta k_1 = 0, \qquad (6.3.35)$$

$$q(k, k_1) + \frac{\partial q}{\partial k}(k, k_1)\delta k + \frac{\partial q}{\partial k_1}(k, k_1)\delta k_1 = 0, \qquad (6.3.36)$$

for the increments δk and δk_1. The four partial derivatives are calculated numerically using neighbouring values of k and k_1. The new approximations $k + \delta k$ and $k_1 + \delta k_1$ are thus determined and the whole procedure repeated until the conditions (6.3.34) at $\hat{\eta} = 0$ are satisfied. The computations were carried out with $\hat{\eta}_\infty = 10$ and a step length $\Delta\hat{\eta} = 0.01$ in the Runge Kutta scheme. The final solutions for $\hat{F}$ and $\hat{F}''$ are shown in figures 6.1 and 6.2 and the value of $\hat{F}(\infty)$ is found to be

$$k = 2.598, \qquad (6.3.37)$$

significantly larger than the estimate given by (6.3.29). The value of $\hat{F}'(0)$ was found to be

$$\hat{F}'(0) = 1.125. \qquad (6.3.38)$$

Once the numerical solution for $\hat{F}$ was found, the temperature profile is given by

$$\widetilde{G}(\tilde{\eta}) = C_0 \hat{G}(\hat{\eta}), \qquad (6.3.39)$$

where

$$\hat{G} = 1 - \hat{F}' \qquad (6.3.40)$$

and this function is shown in figure 6.3. We note that

$$\hat{G}(0) = -0.125, \qquad (6.3.41)$$

so that the wall temperature at $x = 0$ given by (6.3.12) is an increasing function of Z, which is physically plausible.

The solution for $\hat{F}$ was checked by using the symbolic algebra package MATHEMATICA to compute the solution forwards from $\hat{\eta} = 0$ using the initial conditions (6.3.20) together with (6.3.38). Figures 6.4-6.6 show the effect of changing the value of $\hat{F}'(0)$ by a small amount, leading to the onset of the singularity (6.3.23). This onset is delayed to higher values of $\hat{\eta}$ by a fine adjustment of $\hat{F}'(0)$

but the solution is extremely sensitive to its value, making the backward shooting method a much better option.

In the horizontal boundary layer

$$\bar{\phi} \sim A(X)Z^{-1}, \quad \bar{\theta} \sim b + C(X)Z^{-3}, \quad Z \to \infty \qquad (6.3.42)$$

and substitution into (6.2.3) and (6.2.4) gives

$$2A = -C', \qquad (6.3.43)$$
$$12C = AC' - 3A'C. \qquad (6.3.44)$$

The boundary conditions (6.2.6) are equivalent to the requirement that

$$A = C' = 0 \quad \text{at} \quad X = 1. \qquad (6.3.45)$$

Substitution of A in (6.3.44) using (6.3.43) gives a second order equation for C:

$$3CC'' - C'^2 - 24C = 0, \qquad (6.3.46)$$

which can be converted to the first order equation

$$\frac{dP}{dC} - \frac{P}{3C} = \frac{8}{P} \qquad (6.3.47)$$

using the substitution $P = C'$. This can be integrated using the further substitution $V = P^2$, giving

$$V = C'^2 = 48C - KC^{\frac{2}{3}} \qquad (6.3.48)$$

where K is a constant. Since $C' = -2A = -2A_0$ at $X = 0$ and $C = C_0$ at $X = 0$ it follows that

$$K = 48C_0^{\frac{1}{3}}(1 - \frac{1}{12}k^2), \qquad (6.3.49)$$

where A_0 has been replaced in terms of C_0 using (6.3.22). Since $k = 2.598$ from (6.3.37) it follows that K is positive. Another integration of (6.3.48), making use of the fact that $C = C_0$ at $X = 0$, gives

$$\int_{C_0}^{C} \frac{dC}{(48C - KC^{\frac{2}{3}})^{\frac{1}{2}}} = -X, \qquad (6.3.50)$$

where it is assumed that $C' \leq 0$, so that $A > 0$ in (6.3.13), consistent with the

fact that the stream function should be positive. The integral can be evaluated by the substitution

$$U = \left(\frac{C}{C_0}\right)^{\frac{1}{3}} - 1 + \frac{1}{12}k^2 \tag{6.3.51}$$

to obtain

$$3\left(\frac{C_0}{48}\right)^{\frac{1}{2}} \int_{\frac{1}{12}k^2}^{U} \frac{(U + 1 - \frac{1}{12}k^2)}{U^{\frac{1}{2}}} dU = -X. \tag{6.3.52}$$

From the boundary condition (6.3.45) at $X = 1$, together with (6.3.48), it follows that

$$C(1) = \left(\frac{K}{48}\right)^3 = (1 - \frac{1}{12}k^2)^3 C_0, \tag{6.3.53}$$

so that

$$U = 0 \quad \text{at} \quad X = 1. \tag{6.3.54}$$

Setting $X = 1$ in (6.3.52) now determines the value of C_0 as

$$C_0 = 16k^{-2}\left(1 - \frac{1}{18}k^2\right)^{-2} \approx 6.068 \tag{6.3.55}$$

and from (6.3.22), the corresponding value of A_0 is

$$A_0 = kC_0^{\frac{1}{2}} = 6.400. \tag{6.3.56}$$

The complete solution for $C(X)$ is given implicitly from (6.3.52) as

$$\left(\frac{C_0}{12}\right)^{\frac{1}{2}} U^{\frac{1}{2}}(U + 3 - \frac{1}{4}k^2) = 1 - X, \tag{6.3.57}$$

where C is related to U by (6.3.51), and is shown in figure 6.7. The corresponding solution for $A(X)$ is then given from (6.3.43) and (6.3.48) as

$$A = (12C_0)^{\frac{1}{2}} U^{\frac{1}{2}} \left(U + 1 - \frac{1}{12}k^2\right) \tag{6.3.58}$$

and is shown in figure 6.8. We note from (6.3.53) that

$$C(1) = 0.508, \tag{6.3.59}$$

so that the wall temperature at $x = L$ given by (6.3.42) is a decreasing function of Z, consistent with the maximum value ($\bar{\theta} = 1$) which occurs at the upper corner

147

$x = L, \quad z = 1.$

The asymptotic structure found here provides a solution as $Z \to \infty$ consistent across both the horizontal and vertical boundary layer regions. In the next section we briefly consider the implications of this structure for the flow and temperature fields in the main core region of the cavity.

6.4 Core region

Summarizing the results of Section 6.3, it has been found that at the lower edge of the horizontal boundary layer the temperature and stream function have the forms

$$T \sim b + \frac{C(X)}{Z^3}, \qquad \psi \sim R^{1/3}L^{1/3}\frac{A(X)}{Z} \tag{6.4.1}$$

as $Z \to \infty$, where $X = x/L$ and $Z = R^{1/3}L^{-2/3}(1-z)$. Also, at the lower end of the vertical boundary layer the temperature and stream function have the forms

$$T \sim b + \frac{\widetilde{G}(\tilde{\eta})}{Z^3}, \qquad \psi \sim R^{1/3}L^{1/3}\frac{\widetilde{F}(\tilde{\eta})}{Z} \tag{6.4.2}$$

as $Z \to \infty$, where

$$\tilde{\eta} = \widetilde{X}/Z^2 = Lx/(1-z)^2 \tag{6.4.3}$$

These results suggest that on the scale of the core region, where $0 \le z < 1$ and $0 \le x \le L$, the solutions for the temperature and stream function have the forms

$$T = b + R^{-1}\Theta(x,z) + \ldots, \quad \psi = \Psi(x,z) + \ldots \tag{6.4.4}$$

as $R \to \infty$, where Θ and Ψ are order one functions of x and z. Note that to leading order the temperature has the constant value b determined by the horizontal and vertical boundary layer problems, this being consistent with the conditions of thermal insulation on the sidewalls and lower surface of the cavity.

Substitution of (6.4.4) into the full governing equations (2.1.2) and (2.1.3) shows that Θ and Ψ satisfy the equations

$$\nabla^2\Psi = -\frac{\partial\Theta}{\partial x}, \tag{6.4.5}$$

$$\nabla^2\Theta = \frac{\partial(\Theta,\Psi)}{\partial(x,z)}, \tag{6.4.6}$$

148

which are, in fact, the full equations with the Darcy-Rayleigh number scaled out. On the sidewalls the appropriate boundary conditions are

$$\Psi = \frac{\partial \Theta}{\partial x} = 0 \qquad (x = 0, L) \tag{6.4.7}$$

and on the lower wall

$$\Psi = \frac{\partial \Theta}{\partial z} = 0 \qquad (z = 0). \tag{6.4.8}$$

Finally, the solution must match with the boundary layer forms (6.4.1) and (6.4.2), requiring that

$$\Psi \sim LA(x/L)(1-z)^{-1}, \qquad \Theta \sim L^2 C(x/L)(1-z)^{-3} \quad \text{as} \quad z \to 1$$
$$\text{for} \quad 0 < x \leq L \tag{6.4.9}$$

and that

$$\Psi \sim L\widetilde{F}(\tilde{\eta})(1-z)^{-1}, \qquad \Theta \sim L^2 \widetilde{G}(\tilde{\eta})(1-z)^{-3} \quad \text{as} \quad z \to 1$$
$$\text{for} \quad 0 < \tilde{\eta} < \infty \tag{6.4.10}$$

where $\tilde{\eta} = Lx/(1-z)^2$.

Thus the core problem (6.4.5)-(6.4.10) involves a solution which is singular at the upper boundary where it matches with the horizontal boundary-layer solution and in the upper corner $x = 0, z = 1$ where it matches with the vertical boundary layer (see figure 6.9). The solution for Ψ must complete the circulation of fluid emanating from the vertical boundary layer at the order one level of the stream function, effecting its movement into the bottom of the horizontal boundary layer. The main circulation, at the order $R^{1/3}$ level of the stream function, is completed within the horizontal and vertical boundary layers themselves. As far as the temperature is concerned, it is seen that in the core region this assumes the constant value b to a first approximation, and that relative to this value, there is an order R^{-1} variation of temperature which, from the forms of $\widetilde{G}$ and $C(X)$ determined in Section 6.3, is negative near the sidewall $x = 0$ and positive elsewhere. This is consistent with the pattern of isotherms computed from the full set of equations and boundary conditions at $R = 5000$ in Chapter 3, shown in figure 6.10. The isotherm $T = b$ on which $\Theta = 0$ emanates from the bottom of the vertical boundary layer and intersects the lower boundary of the cavity. Note

149

that since $C(X)$ is a decreasing function of X, the isotherms emanating from the vertical boundary layer should turn upwards near the base of the horizontal boundary layer, and this can also be observed in figure 6.10. The corresponding streamlines are shown in figure 6.11 and would appear to be consistent with the proposed core structure.

Because of the singular nature of the core problem (6.4.5)-(6.4.10), its solution will require a careful numerical treatment and this is not attempted here. It appears, however, that this region will complete the overall asymptotic structure in the limit of large Darcy-Rayleigh number and have a solution which matches consistently with both the horizontal and vertical boundary-layer regions.

6.5   Improved solution of the boundary layer problem

In Chapter 4 an approximate solution of the horizontal boundary-layer problem was obtained by neglecting the vertical boundary layer and looking for an exact solution of the horizontal boundary layer equations which in the present notation is given by

$$\bar{\theta} = \theta_1(Z) - (1 - X)^2 \theta_0(Z), \qquad (6.5.1)$$

$$\bar{\phi} = (1 - X)\phi(Z), \qquad (6.5.2)$$

where X and Z are defined in (6.2.2) and θ_0, θ_1 and ϕ are the functions determined numerically in Chapter 4 and shown graphically in figures 4.3, 4.5 and 4.2 respectively. The constant A which appears in the solution for θ_1 is assumed to be given by (4.3.7) so that the total heat flux through the upper surface $Z = 0$ is zero. We have seen that the solution (6.5.1), (6.5.2) does not have the correct asymptotic behaviour as $Z \to \infty$ but can expect that it provides a good approximation near the upper wall where it satisfies not only the governing equations but also the boundary conditions on $Z = 0$ and on $X = 1$, as well as the heat flux condition referred to above.

In this section we shall obtain an improved approximate solution of the combined horizontal/vertical boundary layer problem by assuming that the solution (6.5.1), (6.5.2) is valid in the upper part of the horizontal layer, say $Z \leq Z_c$, where Z_c is to be determined. In the region $Z \geq Z_c$ we shall assume that the

solution in the horizontal layer is given by a generalization of the asymptotic solution (6.3.42)

$$\bar{\theta} = b + C(X)(Z + K_c)^{-3}, \tag{6.5.3}$$

$$\bar{\phi} = A(X)(Z + K_c)^{-1}, \tag{6.5.4}$$

where K_c is a constant to be determined. Note that K_c is equivalent to an origin shift in the large Z expansion, and is therefore arbitrary as far as the asymptotic theory is concerned. In practice, its value should be determined by the solution of the combined boundary value problem. The functions $A(X)$ and $C(X)$ are those determined in Section 6.3 and shown graphically in figures 6.8 and 6.7. We cannot, of course, expect the solutions (6.5.1), (6.5.2) and (6.5.3), (6.5.4) to join smoothly at $Z = Z_c$ for $0 \leq X \leq 1$, but we can look for a solution in which certain continuity conditions are applied at $Z = Z_c$ on $X = 0$. Since the boundary conditions at $X = 1$ are satisfied by (6.5.1)-(6.5.4), as well as the governing equations, and since the solution (6.5.3), (6.5.4) matches consistently with the solution in the lower part of the vertical boundary layer ($Z \geq Z_c$), we might expect the overall solution to provide a reasonably good approximation to the actual solution.

We proceed then by considering the forms (6.5.1)-(6.5.4) on $X = 0$, where we have

$$\bar{\theta}(0, Z) = \theta_1(Z) - \theta_0(Z), \quad Z \leq Z_c \tag{6.5.5}$$

$$\bar{\phi}(0, Z) = \phi(Z), \quad Z \leq Z_c \tag{6.5.6}$$

and

$$\bar{\theta}(0, Z) = b + C_0(Z + K_c)^{-3}, \quad Z \geq Z_c \tag{6.5.7}$$

$$\bar{\phi}(0, Z) = A_0(Z + K_c)^{-1}, \quad Z \geq Z_c \tag{6.5.8}$$

where $C_0 = C(0) = 6.068$ and $A_0 = A(0) = 6.400$. At $Z = Z_c$ we require continuity of $\bar{\theta}(0, Z)$, $\bar{\phi}(0, Z)$ and $(\partial \bar{\theta}/\partial Z)(0, Z)$, giving

$$\theta_1(Z_c) - \theta_0(Z_c) = b + C_0(Z_c + K_c)^{-3}, \tag{6.5.9}$$

$$\phi(Z_c) = A_0(Z_c + K_c)^{-1} \tag{6.5.10}$$

and

$$\theta_1'(Z_c) - \theta_0'(Z_c) = -3C_0(Z_c + K_c)^{-4} \tag{6.5.11}$$

respectively. We cannot ask for continuity of $(\partial\bar\phi/\partial Z)(0, Z)$ at Z_c because (6.5.6) is a monotonically increasing function of Z, whereas (6.5.8) is a monotonically decreasing function of Z. The three equations (6.5.9)-(6.5.11) may now be solved to obtained the three unknown constants Z_c, K_c and b. This may be done by substituting for $Z_c + K_c$ on the right-hand side of (6.5.11) from (6.5.10), giving

$$\theta_1'(Z_c) - \theta_0'(Z_c) + \frac{3C_0}{A_0^4}(\phi(Z_c))^4 = 0 \tag{6.5.12}$$

which now contains the single unknown Z_c. A plot of the left-hand side of (6.5.12) is shown in figure 6.12, from which it is seen that there are two zeros, one at $Z_c = 3.04$ and another at $Z_c = 0.98$. In practice, we select the one which gives the smallest discontinuity in $(\partial\bar\phi/\partial Z)(0, Z_c)$, namely

$$Z_c = 3.04 \tag{6.5.13}$$

and then the corresponding values of K_c and b are given from (6.5.10) and (6.5.9) respectively. This gives

$$K_c = 2.73 \tag{6.5.14}$$

and

$$b = 0.213 \tag{6.5.15}$$

The complete profiles $\bar\theta(0, Z)$ and $\bar\phi(0, Z)$ with these values of Z_c, K_c and b are shown in figures 6.13 and 6.14. Note that $Z = Z_c$ defines the position of the maximum value of the stream function,

$$\bar\phi(0, Z_c) = 1.108. \tag{6.5.16}$$

The maximum value of the temperature occurs within the upper section $Z \leq Z_c$ and is thus the value $Z = Z_0 = 0.96$ found in Chapter 4, with

$$\bar\theta(0, Z_0) = 0.313. \tag{6.5.17}$$

As $Z \to \infty$, the temperature approaches the value (6.5.15), which is slightly different from that determined in Chapter 4.

152

Figures 6.15 and 6.16 show the isotherms and streamlines in the horizontal boundary layer, as determined by the composite solutions (6.5.1)-(6.5.4) and the results (6.5.13)-(6.5.15). Note that the stream function is discontinuous along the line $Z = Z_c$, $0 < X < 1$ because the linear dependence on X in (6.5.2) does not quite match the nonlinear dependence of $A(X)$ in (6.5.4). In other respects the solution has all the features expected of the actual solution, and in particular provides for the transportation of fluid from the lower part of the vertical boundary layer to the upper part.

6.6 Numerical scheme for the boundary layer problem

In this section we propose a numerical scheme for solving the combined horizontal and vertical boundary layer problem (6.2.3)-(6.2.7) and (6.2.10)-(6.2.15) and report some initial results. Further work is needed to complete the numerical solution.

In the horizontal layer we allow the solution to evolve to a steady state by solving the artificial time-dependent system

$$\frac{\partial \bar{\phi}}{\partial t} = \frac{\partial^2 \bar{\phi}}{\partial Z^2} + \frac{\partial \bar{\theta}}{\partial X}, \tag{6.6.1}$$

$$\frac{\partial \bar{\theta}}{\partial t} = \frac{\partial^2 \bar{\theta}}{\partial Z^2} - \frac{\partial \bar{\phi}}{\partial X} \frac{\partial \bar{\theta}}{\partial Z} + \frac{\partial \bar{\phi}}{\partial Z} \frac{\partial \bar{\theta}}{\partial X}, \tag{6.6.2}$$

with $\bar{\phi}$ and $\bar{\theta}$ regarded as functions of X, Z and t. The approximate solution found in the previous section is taken as the initial state at $t = 0$. The boundary conditions applied to the above equations in the Z direction are taken to be

$$\bar{\phi} = 0, \quad \bar{\theta} = 1 - (X - 1)^2 \quad \text{on} \quad Z = 0 \tag{6.6.3}$$

and

$$\bar{\phi} \sim A(X)Z^{-1}, \quad \frac{\partial \bar{\theta}}{\partial Z} \sim -3C(X)Z^{-4}, \quad Z \to \infty, \tag{6.6.4}$$

where $A(X)$ and $C(X)$ are the functions determined in Section 6.3. In the X direction, it is assumed that

$$\bar{\phi} = \frac{\partial \bar{\theta}}{\partial X} = 0 \quad \text{at} \quad X = 1 \tag{6.6.5}$$

153

and that

$$\bar{\theta} = \tilde{\theta}_\infty(Z) \quad \text{at} \quad X = 0 \quad \text{for} \quad Z \geq Z_0 \tag{6.6.6}$$

where $\tilde{\theta}_\infty(Z)$ is taken to be the temperature profile determined by the approximate solution of the previous section and shown in figure 6.13. Note that only the section $Z \geq Z_0$ is used, where $Z_0 = 0.96$ is the point at which $\tilde{\theta}'_\infty = 0$.

The equations (6.6.1) and (6.6.2) are discretized on a uniform mesh in X and Z in the region $0 \leq X \leq 1$, $0 \leq Z \leq Z_\infty$ where Z_∞ is a suitably large outer boundary. In practice this must be taken quite large because of the algebraic decay of the solution in (6.6.4). An explicit finite difference scheme is used similar to that applied to the full cavity problem in Chapters 2 and 3 except, of course, that the second order derivatives in X are missing from (6.6.1) and (6.6.2). This allows new values of $\bar{\phi}$ and $\bar{\theta}$ to be determined at successive time steps at all internal grid points. New values of $\bar{\phi}$ and $\bar{\theta}$ on $Z = 0$ and $Z = Z_\infty$ are determined using (6.6.3) and (6.6.4), in the latter case applying a quadratic extrapolation for $\bar{\theta}$ based on two internal grid points. New values of $\bar{\phi}$ and $\bar{\theta}$ on $X = 1$ are determined using (6.6.5) and again a quadratic extrapolation is used in the case of $\bar{\theta}$. No conditions are applied on $\bar{\theta}$ and $\bar{\phi}$ for $Z < Z_0$ when $X = 0$ and new values are set there simply by a linear extrapolation of the solution at two internal grid points. The same method is used to set the new values of $\bar{\phi}$ in $Z \geq Z_0$; the values of the temperature in $Z \geq Z_0$ are fixed by (6.6.6). Results of computations with step sizes $\Delta X = \Delta Z = 0.1$ and an outer boundary $Z_\infty = 24$ are shown in figures 6.17-6.20. These were obtained after 48000 time steps, using $\Delta t = 0.004$, at which point the solution had reached a steady state, to within variations of $\bar{\theta}$ and $\bar{\phi}$ in the fourth significant figure. Figures 6.17 and 6.18 show the new profiles of $\bar{\theta}$ and $\bar{\phi}$ on $X = 0$, which we shall denote by $\tilde{\theta}_\infty(Z)$ and $\tilde{\phi}_\infty(Z)$ respectively and these may be compared with the initial profiles at $t = 0$ shown in figures 6.13 and 6.14. Of course the temperature is unchanged in the region $Z \geq Z_0$. There is a slight change in the temperature for $Z < Z_0$ and the position of maximum stream function moves from $Z = 3.04$ at $t = 0$ to $Z = 2.4$. Its value changes from 1.108 to $\tilde{\phi}_{\infty max} = 0.92$. Isotherms and streamlines of the steady-state horizontal boundary layer solution are shown in figures 6.19 and 6.20. The initial discontinuity in $\bar{\phi}$ (see figure 6.16) is smoothed out.

The next stage of the numerical scheme is to take the new steady-state profiles of $\tilde{\phi}_\infty$ and $\tilde{\theta}_\infty$ (the latter for $Z < Z_0$ only) and use these as boundary conditions for $\tilde{\phi}$ and $\tilde{\theta}$ at the edge of the vertical boundary layer. The steady-state vertical

boundary-layer equations (6.2.10), (6.2.11) are parabolic in Z, although there may be slight upward velocities near the edge of the layer if the outward exponential decay is oscillatory -see Section 5.5. This suggests that the vertical boundary layer system could be solved numerically by marching down the layer in the Z direction. This should determine a new temperature profile $\tilde{\theta}_\infty$ at the edge of the layer for $Z \geq Z_0$ (and an adjustment in the location of Z_0). As $Z \to \infty$ we expect the asymptotic form (6.3.12) to emerge, including an adjustment in the value of b. The vertical boundary layer widens considerably as $Z \to \infty$ but use of a coordinate transformation $(\widetilde{X}, Z) \to (\eta, Z)$ where $\eta = \widetilde{X} \tilde{f}(Z)$ will enable a uniform grid in η and Z to be used over a finite domain $0 \leq \eta \leq \eta_\infty$, $0 \leq Z \leq Z_\infty$. The function $\tilde{f}(Z)$ can be chosen to be unity at $Z = 0$ and to have the asymptotic behaviour $\tilde{f} \sim Z^{-2}$, $Z \to \infty$ to accommodate the spreading of the layer as Z increases. The governing equations then become

$$\tilde{f} \frac{\partial^2 \tilde{\phi}}{\partial \eta^2} + \frac{\partial \tilde{\theta}}{\partial \eta} = 0, \qquad (6.6.7)$$

$$\tilde{f} \frac{\partial^2 \tilde{\theta}}{\partial \eta^2} + \frac{\partial \tilde{\phi}}{\partial Z} \frac{\partial \tilde{\theta}}{\partial \eta} - \frac{\partial \tilde{\phi}}{\partial \eta} \frac{\partial \tilde{\theta}}{\partial Z} = 0, \qquad (6.6.8)$$

where we now regard $\tilde{\phi}$ and $\tilde{\theta}$ as functions of Z and η. It is anticipated that a Crank-Nicolson scheme can be used to solved this system and the resulting profile $\tilde{\theta}_\infty$ obtained in $Z \geq Z_0$ then used to find an improved solution in the horizontal boundary layer. The whole process will then be repeated until convergence is achieved. In fact, some solutions in the vertical boundary layer region were obtained, based on inserting artificial time derivatives on the right-hand sides of (6.6.7) and (6.6.8). However, this method did not prove robust and so the results are not described in detail here. We believe that the difficulty in using this method lies in the fact that it requires information to propagate into the layer from the region $Z \geq Z_0$ as time progresses and this is contrary to the physical processes involved. Solution of the steady-state system (6.6.7), (6.6.8) will avoid this difficulty, but is less straightforward to implement and is left for future investigation.

Nevertheless, the results shown in figures 6.17-6.20 probably represent a good approximation of the final solution; the adjustment to the stream function profile $\tilde{\phi}_\infty$ in this first iteration of the scheme is relatively small and suggests that the subsequent adjustment to the temperature profile arising from the vertical

155

boundary layer will also be small.

6.7   Summary

In this chapter we have considered the solution of the combined horizontal/vertical boundary layer system involved in the leading order asymptotic structure in the cavity as the Darcy-Rayleigh number tends to infinity. We have found properties of this solution, including its limiting form as $Z \to \infty$, which suggest that it is consistent with the limiting behaviour observed in the numerical calculations of Chapter 3 and that it matches consistently with a solution in the core region of the cavity. A complete numerical solution of both the core problem and the boundary layer problem remains to be found. However, it is interesting to compare the predictions of the preliminary results of Section 6.5 and 6.6 with the numerical calculations of Chapter 3. According to the results of Section 6.5, the temperature maximum at the end of the horizontal boundary layer is $T \approx 0.313$ and occurs at a height

$$z = 1 - R^{-1/3}L^{2/3}Z_0 \qquad (6.7.1)$$

where $Z_0 = 0.96$. For a square cavity (L=1)and a Darcy-Rayleigh number $R = 5000$ the formula (6.7.1) gives $z = 0.94$, which compares quite well with the numerical results of figure 3.14. The maximum value of T is also consistent with the results shown in figure 3.14. According to the results of Section 6.6, the stream function maximum at the end of the horizontal layer occurs at

$$z = 1 - R^{-1/3}L^{2/3}Z_1, \qquad (6.7.2)$$

where $Z_1 = 2.4$. Again, with $L = 1$ and $R = 5000$, this gives $z = 0.86$ which compares reasonably well with the position of the centre of the eddy in figure 3.15, given in table 3.1 as $z_{max} = 0.90$. The value of the stream function at this point given by the results of Section 6.6 is

$$\psi \approx R^{1/3}L^{1/3}\tilde{\phi}_{\infty max} \qquad (6.7.3)$$

where $\tilde{\phi}_{\infty max} = 0.92$. With $L = 1$ and $R = 5000$ this gives $\psi \approx 15.7$ which compares well with the numerical value $\psi_{max} = 13.9$ given in table 3.1. Hopefully these comparisons will be improved by completing the numerical solution of

the combined boundary layer problem, although it must be recognized that the asymptotic theory presented here provides only leading approximations to T and ψ as $R \to \infty$.
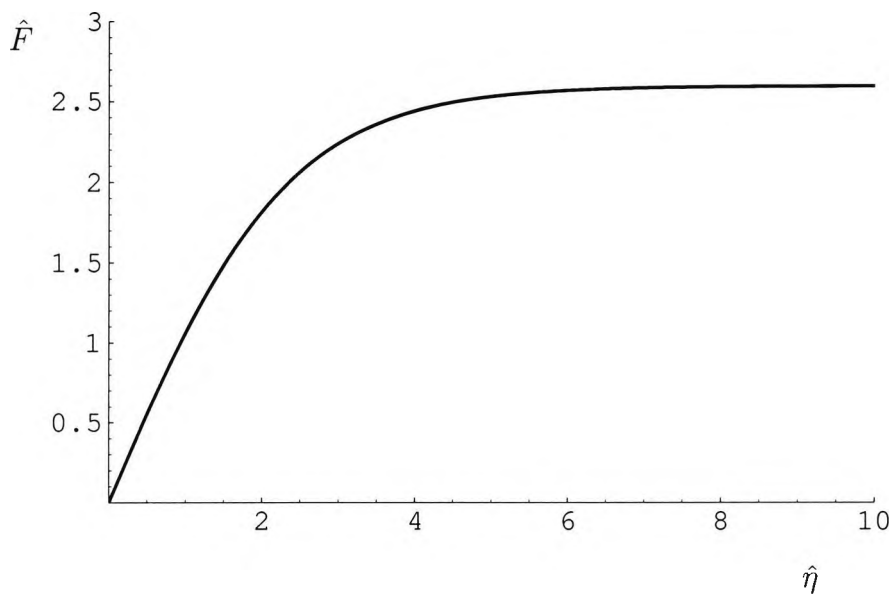
Figure 6.1: Graph for $\hat{F}(\hat{\eta})$ calculated by backward shooting method
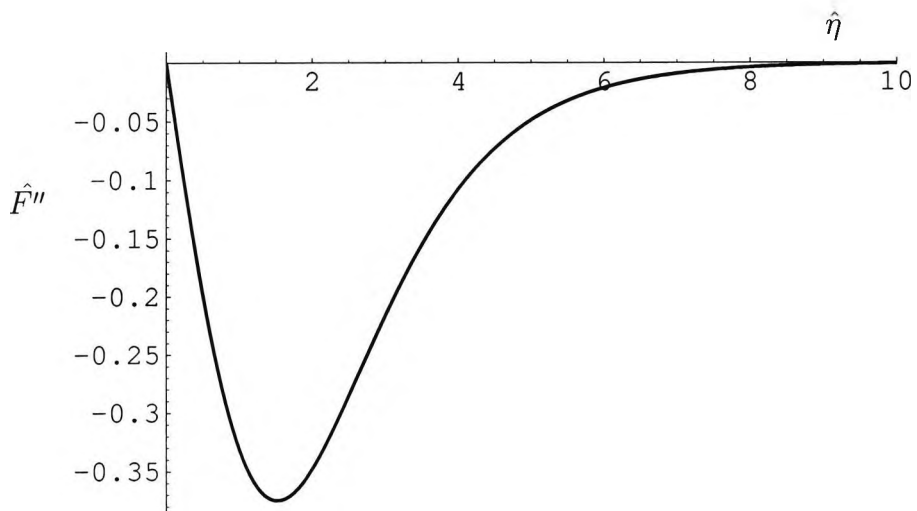
Figure 6.2: Graph of $\hat{F}''(\hat{\eta})$ calculated by backward shooting method
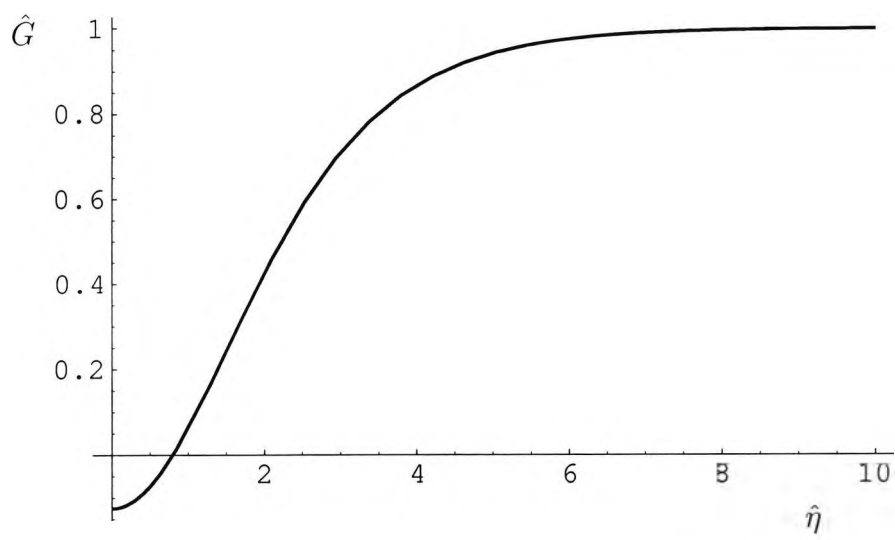
Figure 6.3: Graph of $\hat{\hat{G}}(\hat{\eta})$
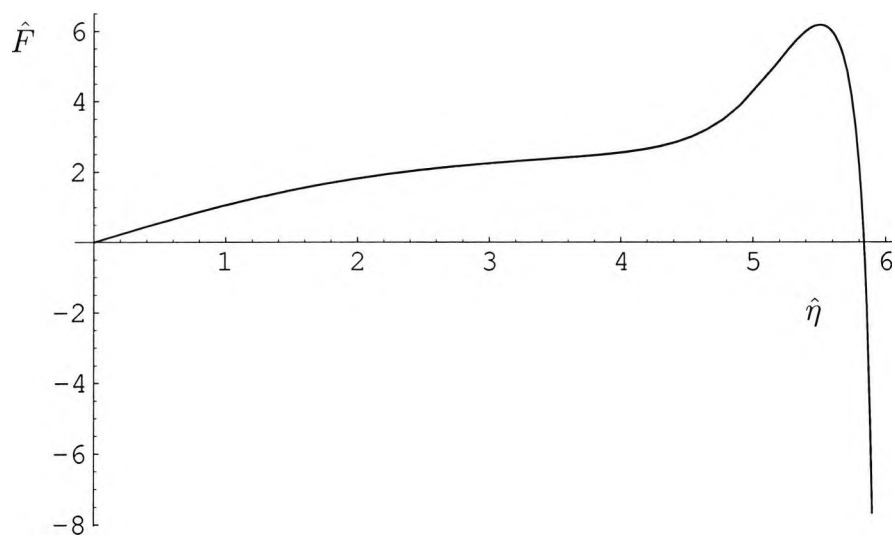
Figure 6.4: Graph of $\hat{F}$ computed outwards using MATHEMATICA with $\hat{F}'(0) = 1.124$
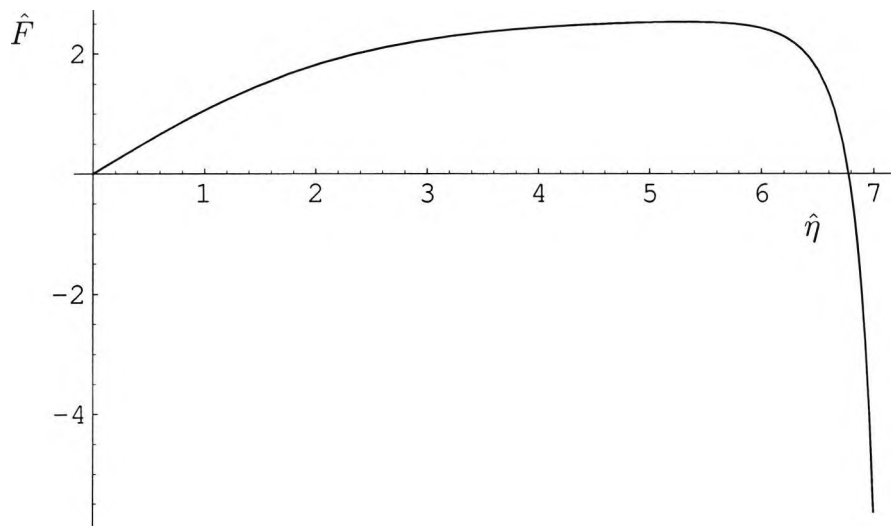
Figure 6.5: Graph of $\hat{F}$ computed outwards using MATHEMATICA with $\hat{F}'(0) = 1.125$
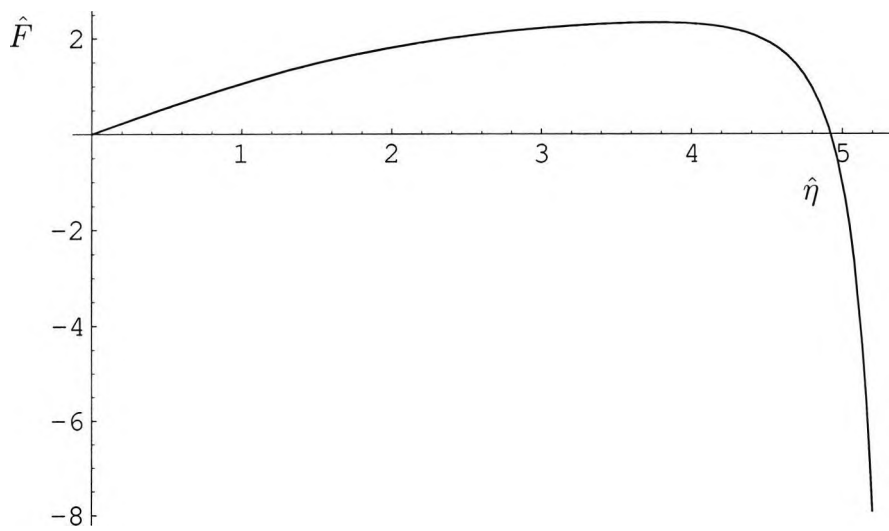
Figure 6.6: Graph of $\hat{F}$ computed outwards using MATHEMATICA with $\hat{F}'(0) = 1.126$
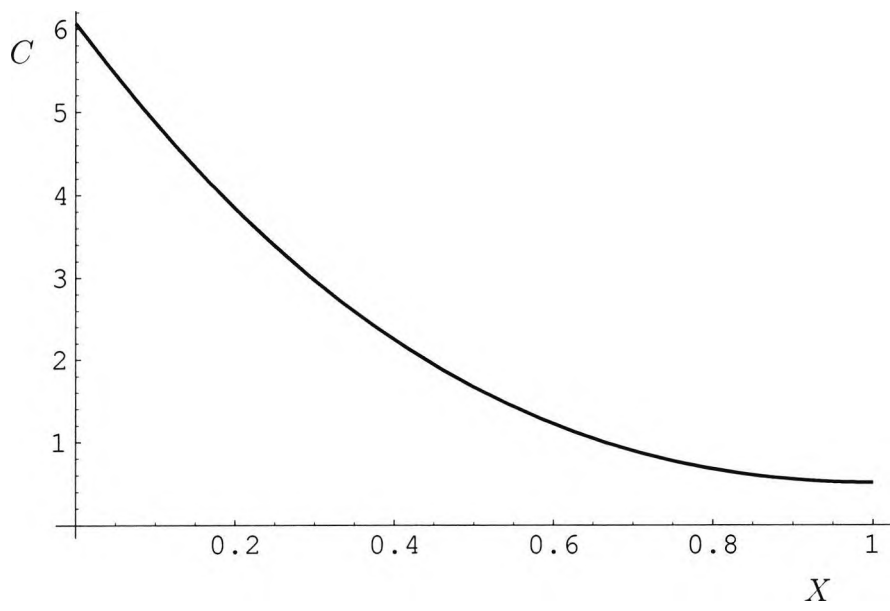
Figure 6.7: Graph of $C(X)$
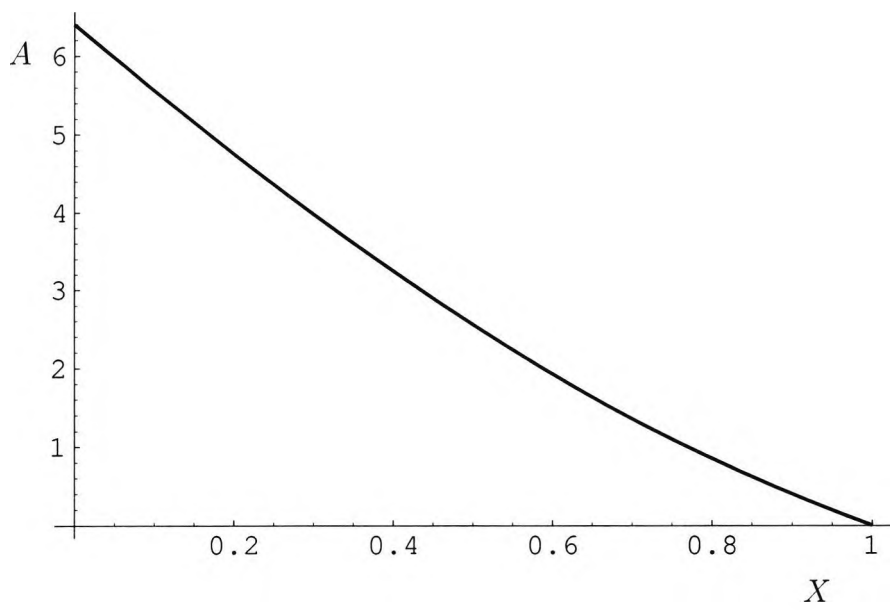
Figure 6.8: Graph of $A(X)$
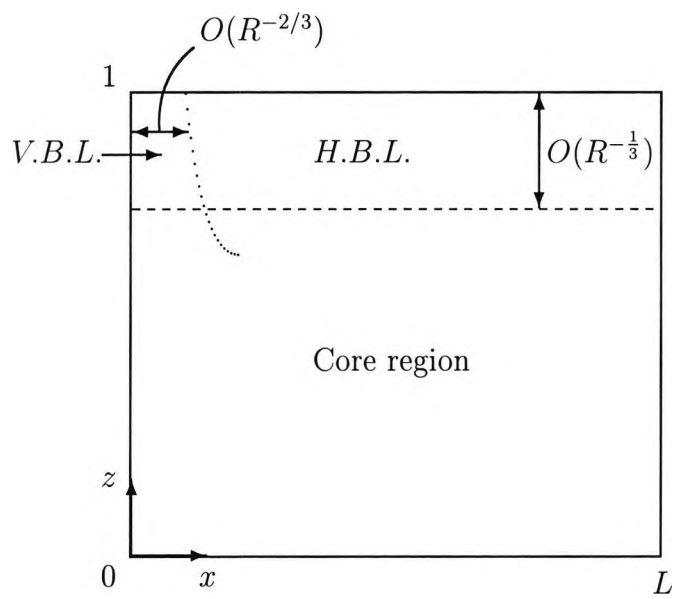
Figure 6.9: The main flow regions in the large Darcy-Rayleigh number limit.
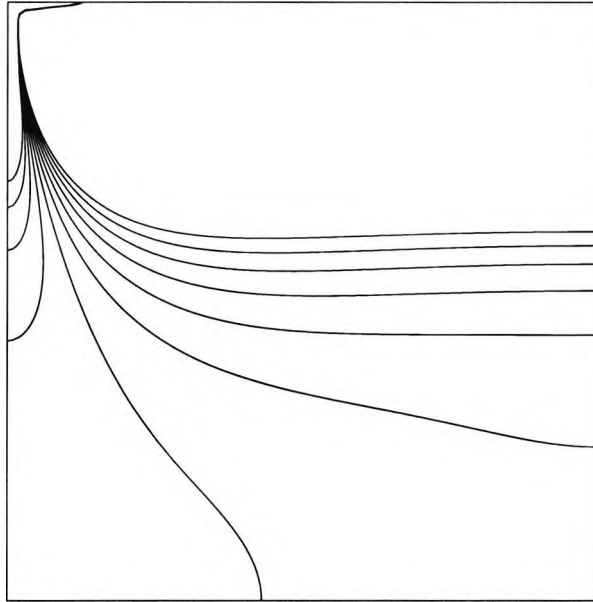
Figure 6.10: Isotherms between 0.23 and 0.24 from the numerical calculation for $R = 5000$ and $L = 1$
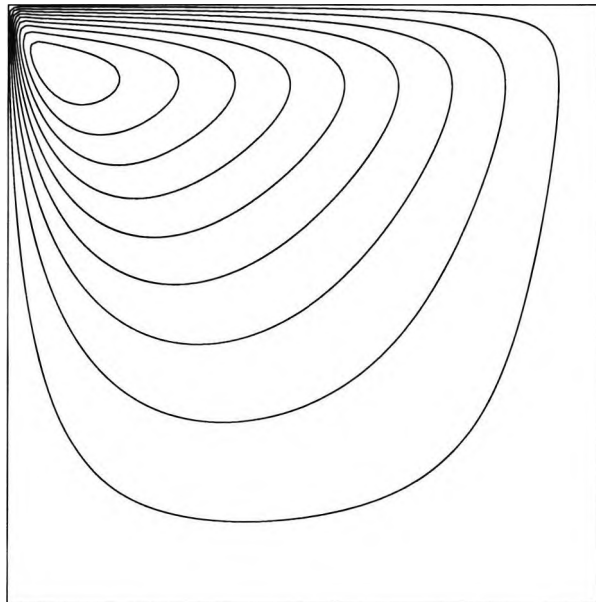
Figure 6.11: Streamlines from the numerical calculation for $R = 5000$ and $L = 1$
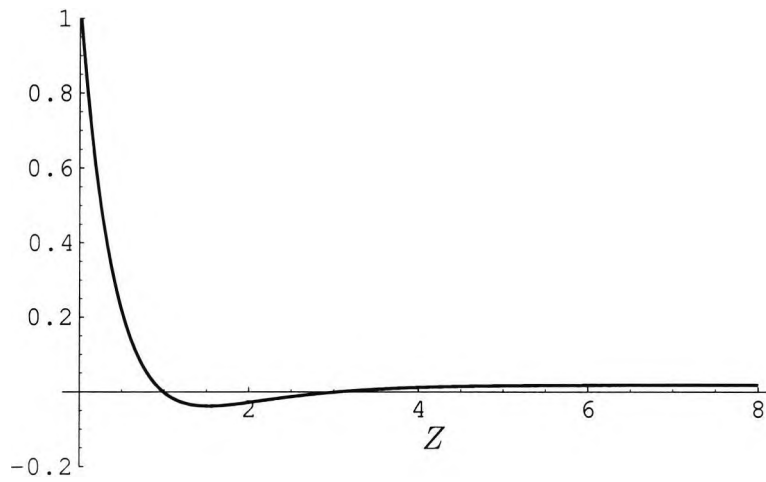
Figure 6.12: Graph of $\theta_1'(Z) - \theta_0'(Z) + \frac{3C_0}{A_0^4}(\phi(Z))^4$
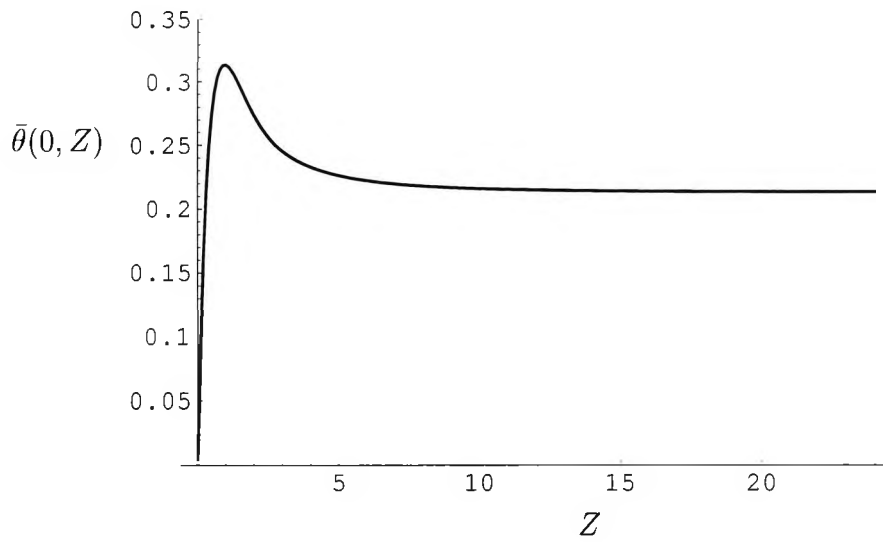
Figure 6.13: Temperature at $X = 0$
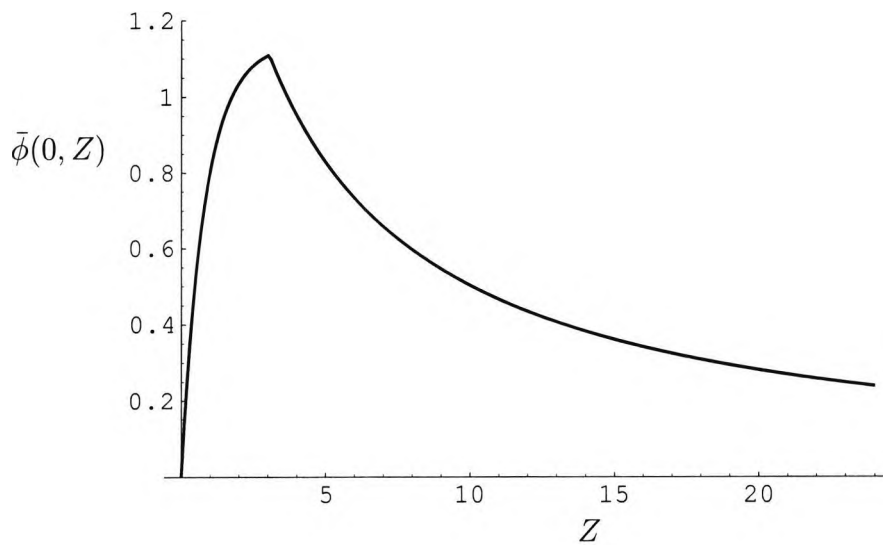
Figure 6.14: Stream function at $X = 0$

169
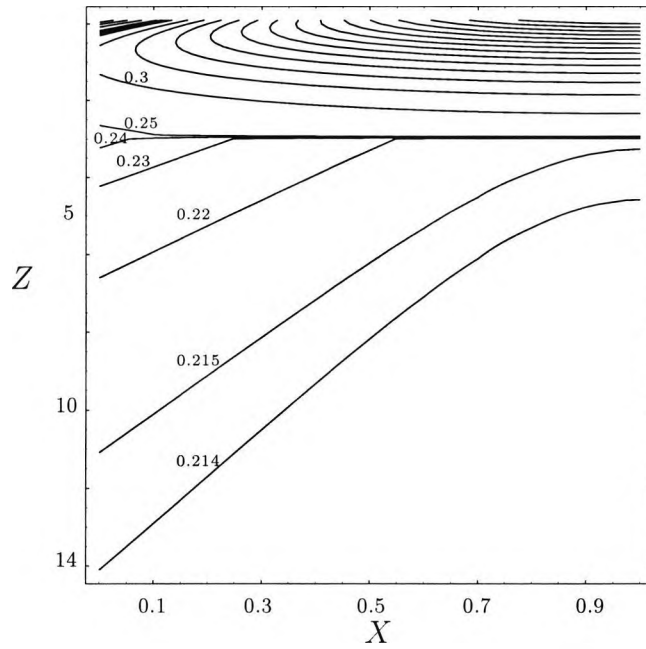
Figure 6.15: Isotherms in the horizontal boundary layer. The upper contours are at intervals of 0.05 in $\bar{\theta}$.
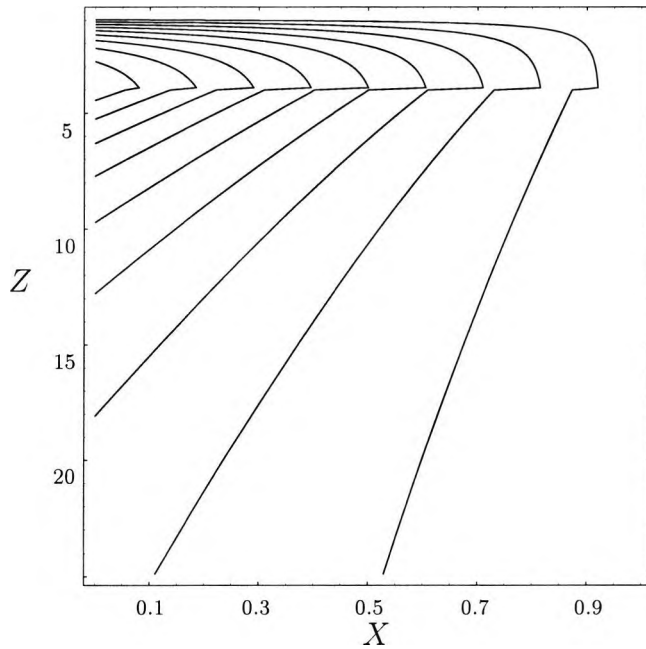
Figure 6.16: Streamlines in the horizontal boundary layer
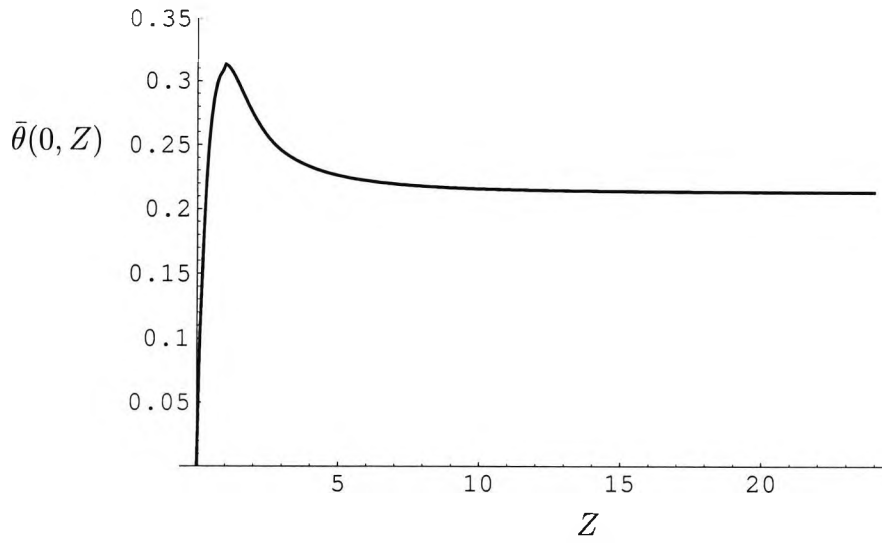
Figure 6.17: Temperature at $X = 0$ from the numerical solution of the horizontal boundary layer equations
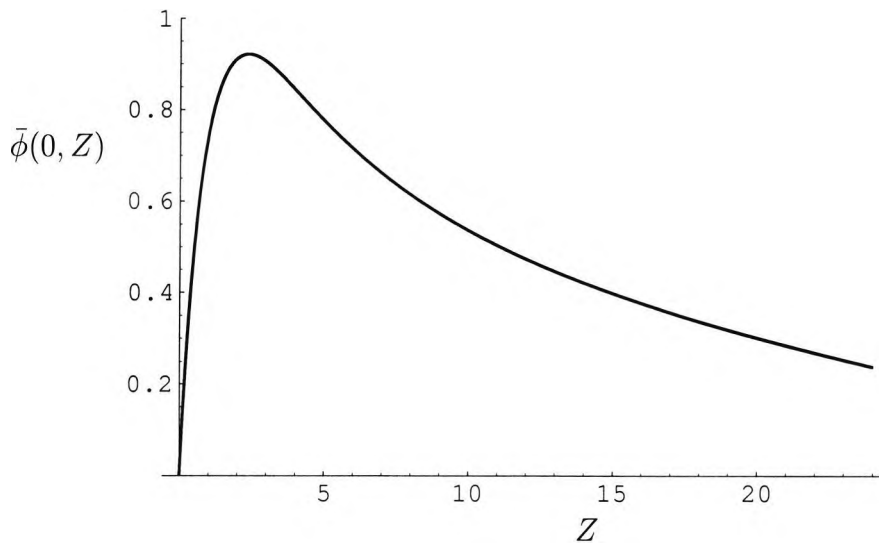
Figure 6.18: Stream function at $X = 0$ from the numerical solution of the horizontal boundary layer equations

171
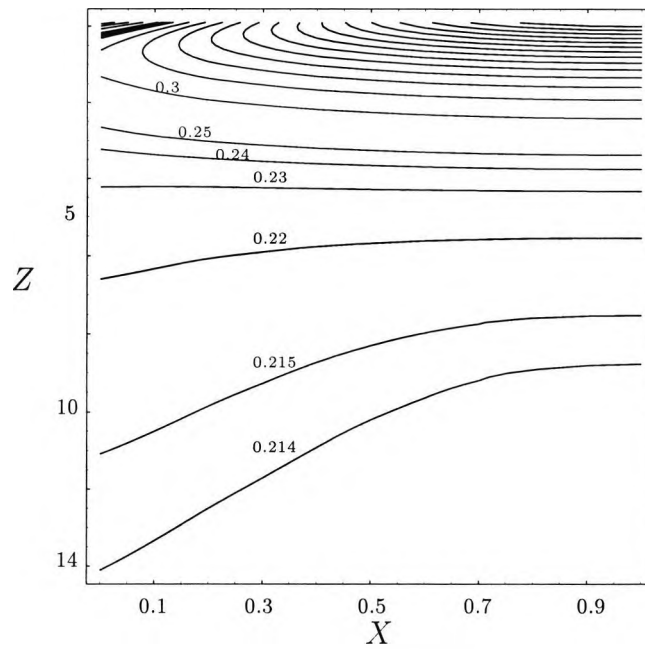
Figure 6.19: Isotherms from the numerical solution of the horizontal boundary layer equations. The upper contours are at intervals of 0.05 in $\bar{\theta}$
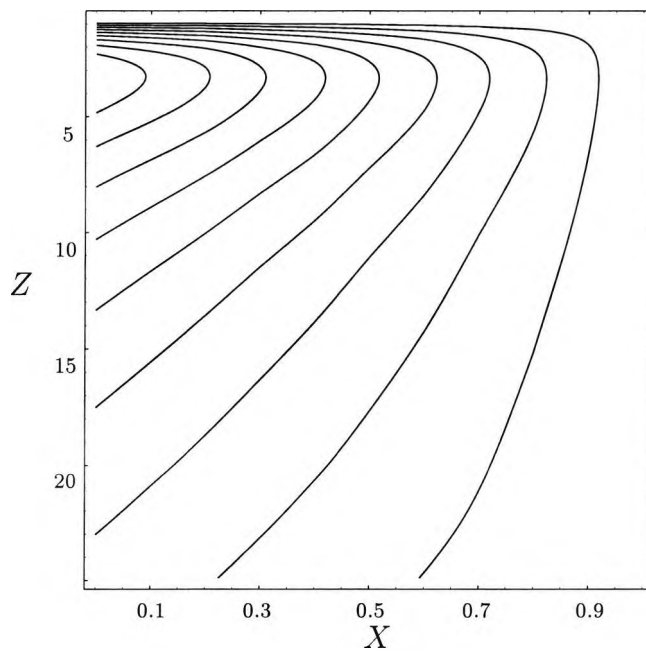
Figure 6.20: Streamlines from the numerical solution of the horizontal boundary layer equations

Chapter 7

Conclusion

7.1 Summary

This thesis has been concerned with steady two-dimensional flow in a rectangular cavity filled with a fluid-saturated porous medium. The upper surface of the cavity is differentially heated, whereas both sides of the cavity and the bottom are thermally insulated. In Chapter 2 we investigated the case where the non dimensional temperature on the upper surface is a cosine function varying from zero at the cold end to unity at the hot end. Focusing on the case of a square cavity we found that the fluid circulates in a single-cell pattern, rising in the hotter half of the cavity and descending in the colder half. The centre of circulation moves towards the upper cold end of the cavity as the Darcy-Rayleigh number R increases, with the maximum non-dimensional stream function, ψ_{max}, varying from a value proportional to R as $R \to 0$ to a value proportional to $R^{1/3}$ as $R \to \infty$. The isotherms migrate towards the hot end of the cavity as R increases, forming a horizontal boundary layer in the upper part of the cavity as $R \to \infty$. The temperature below the horizontal boundary layer reaches an almost constant value of about 0.1 in this limit.

In Chapter 3 we investigated the case where the non-dimensional temperature on the upper surface is a quadratic function varying from zero at the cold end to unity at the hot end. Numerical results were obtained for aspect ratios in the range $1/4 \leq L \leq 4$ and in each case the behaviour of the flow with increasing R was found to be similar to that observed in the case of the cosine profile, although the linear temperature variation in the upper cold corner leads to a more vigorous motion there. The temperature in the lower part of the cavity

was found to approach a value of between 0.2-0.3 in the limit of large R. The quadratic temperature variation at the upper surface allowed an exact solution of the horizontal boundary layer equations to be obtained in Chapter 4. This solution on a vertical scale of $O(R^{-1/3})$ near the upper surface does not satisfy the correct boundary conditions at the cold end of the layer but by considering the heat flux though the upper surface, predicts the temperature below the horizontal boundary layer to be 0.229 in the limit of large R, which is in good agreement with the numerical results.

In Chapter 5 we investigated the implications of the horizontal boundary layer solution for the solution in a vertical boundary layer at the cold end. We showed that it is not possible to find a satisfactory solution in the vertical boundary layer if we use the exact solution of Chapter 4 in the horizontal boundary layer. This is because the vertical layer cannot accept specification of both the temperature and stream function at the edge of the layer in any region where the vertical temperature gradient is positive. Furthermore, it was found that no solutions of the vertical layer were possible in which the stream function approaches a nonzero value at the lower end of the layer. This led to the proposal, explored in detail in Chapter 6, that the fluid descending in the vertical layer must empty back into the horizontal layer on the vertical scale of $O(R^{-1/3})$ near the upper surface, so that the combined horizontal/vertical boundary layer system encompasses the centre of the eddy observed in the numerical calculations. An asymptotic solution was found across the lower edge of the vertical/horizontal boundary layers which confirmed the consistency of this approach and the possibility of matching with a solution in the core region in which the variations in temperature and stream function are order R^{-1} and order one respectively. The vertical layer is of width $O(R^{-2/3})$ but expands as the square of the downstream distance, thereby merging with the core in the upper cold corner. An improved solution of the boundary layer system was obtained using a combination of the asymptotic solution and the approximate solution of Chapter 4, and this led to the prediction of a constant core temperature of 0.213, in good agreement with the numerical computations. Some preliminary results were also obtained for a complete numerical solution of the boundary layer system which indicated reasonable agreement of both the position and values of maximum temperature and maximum stream function at the cold end of the horizontal layer.

7.2 Future work

The immediate task following on from this work is to complete the numerical solution of the combined vertical/horizontal boundary layer problem formulated in Chapter 6 and thus, in particular, to find an accurate prediction of the core temperature. A numerical solution of the core problem (6.4.5)-(6.4.10) is also needed to verify the overall consistency of the large Darcy-Rayleigh number structure proposed here.

One modification of the present work would be to consider cases where the temperature profile at the upper surface is not monotonic, leading to the possibility of two (or more)-cell flows and, if a temperature minimum occurs at a point somewhere in the middle of the upper surface, the existence of a vertical shear layer there in the limit of large Darcy-Rayleigh number.

The present results may be useful in describing the large Darcy-Rayleigh number structure in a number of other, related, thermally-driven flows. For example, the structure identified here may also be applicable(with modification) in the case of the side-heated cavity ($T = 0$ at $x = 0$ and $T = 1, x = L$) with conducting upper and lower boundaries ($T = x/L$ at $z = 0$ and $z = 1$). The equivalent horizontal boundary layer structure in the case of insulating upper and lower boundaries ($\partial T/\partial z = 0$ at $z = 0$ and $z = 1$) was found by Daniels, Blythe and Simpkins(1982) but this structure is no longer applicable in the conducting case.

Other extensions of this and related work would be to consider the solution structure which emerges for very tall ($L \to 0$) or very shallow ($L \to \infty$) cavities, where there are applications in cavity wall insulation and geophysics, respectively. The numerical computations of Chapter 3 will provide useful guidance in this respect. Variation of material properties (such as the thermal expansion coefficient and the fluid viscosity) with temperature are also relevant, particularly in geophysical applications, and would be interesting to investigate, as would the various modifications to Darcy's law.

References

Ansari, A. and Daniels, P. G. 1993 Thermally driven tall cavity flows in porous media. *Proc. Roy. Soc. London A* **433**, 163-181.

Ansari, A. and Daniels, P. G. 1994 Thermally driven tall cavity flows in porous media: the convective regime. *Proc. Roy. Soc. London A* **444**, 375-388.

Bankvall, C. G. 1974 Natural convection in a vertical permeable space. *Wärme- und Stoffübertragung* **7**, 22-30.

Bear, J. 1988 *Dynamics of Fluids in Porous Media.* Dover Publications, New York.

Blythe, P. A., Daniels, P. G. and Simpkins, P. G. 1982 Thermally driven cavity flows in porous media. I. The vertical boundary layer structure near the corners. *Proc. Roy. Soc. London A* **380**, 119-136.

Blythe, P. A., Daniels, P. G. and Simpkins, P. G. 1985 Convection in a fluid saturated porous medium due to internal heat generation. *Int. Comm. Heat Mass Transfer* **12**, 493-504.

Blythe, P. A., Simpkins, P. G. and Daniels, P. G. 1983 Thermal convection in a cavity filled with a porous medium: a classification of limiting behaviours. *Int. J. Heat Mass Transfer* **26**, 701-708.

Boussinesq, J. 1903 *Théory Analytique de la Chaleur* . Gauthier-Villars, Paris. vol. 2.

Chan, B. K. C., Ivey, C. M. and Barry, J. M. 1970 Natural convection in enclosed porous media with rectangular boundaries. *J. Heat Transfer* **92**, 21-27.

Chang, I. D. and Cheng, P. 1983 Matched asymptotic expansions for free convection about an impermeable horizontal surface in a porous medium. *Int. J. Heat Mass Transfer* **26**, 163-173.

Cheng, P. and Chang, I. D. 1976 On buoyancy induced flows in a saturated porous medium adjacent to impermeable horizontal surfaces. *Int. J. Heat Mass Transfer* **19**, 1267-1272.

Cheng, P. and Minkowycz, W. J. 1977 Free convection about a vertical flat plate embedded in a porous medium with application to heat transfer from a dike. *J. Geophys. Res.* **82**, 2040-2044.

Chery, J., Bonneville, A., Vilotte, P. J. and Yuen, D. 1991 Numerical modelling of caldera dynamical behaviour. *Geophys. J. Int.* **105**, 365-379.

Combarnous, M. A. and Bories, S. A. 1975 Hydrothermal convection in saturated porous media. *Adv. Hydrosci.* **10**, 232-307.

Daniels, P. G., Blythe, P. A. and Simpkins, P. G. 1982 Thermally driven cavity flows in porous media II. The horizontal boundary layer structure. *Proc. Roy. Soc. London A* **382**, 135-154.

Daniels, P. G., Blythe, P. A. and Simpkins, P. G. 1986 Thermally driven shallow cavity flows in porous media: the intermediate régime. *Proc. Roy. Soc. London A* **406**, 263-285.

Daniels, P. G. and Simpkins, P. G. 1984 The flow induced by a heated vertical wall in a porous medium. *Quart. J. Mech. Appl. Math.* **37**, 339-354.

Daniels, P. G.,Simpkins, P. G. and Blythe, P. A. 1989 Thermally driven cavity flows in porous media: the merged-layer régime. *Proc. Roy. Soc. London A* **426**, 107-124.

de Boer, R. 2000 *Theory of Porous Media.* Springer-Verlag.

Gill, A. E. 1966 The boundary-layer regime for convection in a rectangular cavity. *J. Fluid Mech.* **26**, 515-536.

Haajizadeh, M., Ozguc, A. F. and Tien, C. L. 1984 Natural convection in a vertical porous enclosure with internal heat generation. *Int. J. Heat Mass Transfer* **27**, 1893-1920.

Hickox, C. E. and Gartling, D. K. 1981 A numerical study of natural convection in a horizontal porous layer subjected to an end-to-end temperature difference. *ASME J. Heat Transfer* **103**, 797-802.

Ingham, D. B. and Brown, S. N. 1986 Flow past a suddenly heated vertical plate in a porous medium. *Proc. Roy. Soc. London A* **403**, 51-80.

Ingham, D. B., Merkin, J. H. and Pop, I. 1982 Flow past a suddenly cooled vertical flat surface in a saturated porous medium. *Int. J. Heat Mass Transfer* **25**, 1916-1919.

Ingham, D. B. and Pop, I. 1987 Free convection from a semi-infinite vertical surface bounded by a horizontal wall in a porous medium. *Int. J. Heat Mass Transfer* **30**, 1615-1622.

Joshi, V. and Gebhart, B. 1984 Vertical natural convection flows in porous media: calculations of improved accuracy. *Int. J. Heat Mass Transfer* **27**, 69-75.

Kassoy, D. R. and Zebib, A. 1975 Variable viscosity effects on the onset of convection in porous media. *Phys. Fluids* **18**, 1649-1651.

Klarsfeld, S. 1970 Champs de température associés aux movements de convection naturelle dans un milieu poreux limité. *Rev. Gén. Thermique* **9**, 1403-1424.

Lapwood, E. R. 1948 Convection of a fluid in a porous medium *Proc. Cambridge Phil. Soc.* **44**, 508-521.

Merkin, J. H. 1980 Mixed convection boundary layer flow on a vertical surface in a saturared porous medium. *J. Engng. Math.* **14**, 301-313.

Mohamed, R. A. 1995 Some problems of flow of viscous fluids in a porous medium. Phd thesis, South Valley University, Qena, Egypt.

Morland, L. W., Zebib, A. and Kassoy, D. R. 1977 Variable property effects on the onset of convection in an elastic porous matrix. *Phys. Fluids* **20**, 1255-1259.

Nield, D.A and Bejan, A. 1999 *Convection in Porous Media.* Second Edition. Springer-Verlag.

Oberbeck, A. 1879 Ueber die Wärmeleitung der Flüssigkeiten bei Berücksichtigung der Strömungen infolge von Temperaturdifferenzen. *Ann. Phys. Chem.* **7**, 271-292.

Palm, E., Weber, J. E. and Kvernvold, O. 1972 On steady convection in a porous medium. *J. Fluid Mech.* **54**, 153-161.

Prasad, V. 1987 Thermal convection in a rectangular cavity filled with a heat-generating, Darcy porous medium. *ASME J. Heat Transfer* **109**, 697-703.

Prasad, V. and Kulacki, F. A. 1984 Convective heat transfer in a rectangular porous cavity-effect of aspect ratio on flow structure and heat transfer. *ASME J. Heat Transfer* **106**, 158-165.

Rees, D. A. S. and Bassom, A. P. 1991 Some exact solutions for free convective flows over heated semi-infinite surfaces in porous media. *Int. J. Heat Mass Transfer* **34**, 1564-1567.

Rees, D. A. S. and Bassom, A. P. 1993 The nonlinear non-parallel wave instability

of boundary-layer flow induced by a horizontal heated surface in porous media. *J. Fluid Mech.* **253**, 267-295.

Rees, D. A. S. and Bassom, A. P. 1994 The linear wave instability of boundary layer flow induced by a horizontal heated surface in porous media. *Int. Comm. Heat Mass Transfer* **21**, 143-150.

Schlichting, H. 1968 Boundary-Layer Theory. Sixth Edition. McGraw-Hill.

Schubert, G. and Strauss, J. M. 1982 Transitions in time-dependent thermal convection in fluid-saturated porous media. *J. Fluid Mech.* **121**, 301-303.

Seki, N., Fukusako, S. and Inaba, H. 1978 Heat transfer in a confined rectangular porous cavity packed with a porous media. *Int. J. Heat Mass Transfer* **21**, 985-989.

Simpkins, P. G. and Blythe, P. A. 1980 Convection in a porous layer. *Int. J. Heat Mass Transfer* **23**, 881-887.

Straus, J. M. 1974 Large amplitude convection in porous media. *J. Fluid Mech.* **64**, 51-63.

Straus, J. M. and Schubert, G. 1979 Three-dimensional convection in a cubic box of fluid-saturated porous material. *J. Fluid Mech.* **91**, 155-165.

Tien, C. L. and Vafai, K. 1990 Convective and radiative heat transfer in porous media. *Adv. Appl. Mech.* **27**, 225-281.

Walker, K. L. and Homsy, G. M. 1978 Convection in a porous cavity. *J. Fluid Mech.* **87**, 449-474.

Weber, J. E. 1975 The boundary-layer regime for convection in a vertical porous layer. *Int. J. Heat Mass Transfer* **18**, 569-573.